



Norwegian University of
Science and Technology

Simulation of the Environmental Impact on Turbine Blade Monitoring Sensors

Robert Marcin Nowak

Master's Thesis

Submission date: June 2016

Supervisor: Reidar Kristoffersen, EPT

Co-supervisor: Krzysztof Tesch, GUoT

Norwegian University of Science and Technology
Department of Energy and Process Engineering

EPT-M-2016-94

MASTER THESIS

for

Student ROBERT MARCIN NOWAK

Spring 2016

Simulation of the Environmental Impact on Turbine Blade Monitoring Sensors

*Simulering av innvirkningen fra omgivelsene på monitoreringssensorer på turbinblad***Background and objective**

Wind turbine blades shall be monitored with several wireless sensors attached at different locations on the surface of the blade. It is not possible to mount these sensors inside the blade material, so a design minimizing the wind forces on the sensors is desired. Maintenance and repairs on sensors mounted on wind turbines is difficult and expensive, especially on offshore turbines, so it is important that the sensors can bear any forces acting on them.

The following tasks are to be considered:

1. CFD simulations of airflow over a sensor mounted on different locations on a turbine blade.
2. CFD simulations of different sensor body designs.
3. Investigation of possible impact on the sensor from air temperature/rain/snow/ice.
4. Investigation of aero-acoustics around the sensor.
5. Conclude with a recommended design for the sensor.

Within 14 days of receiving the written text on the master thesis, the candidate shall submit a research plan for his project to the department.

When the thesis is evaluated, emphasis is put on processing of the results, and that they are presented in tabular and/or graphic form in a clear manner, and that they are analyzed carefully.

The thesis should be formulated as a research report with summary both in English and Norwegian, conclusion, literature references, table of contents etc. During the preparation of the text, the candidate should make an effort to produce a well-structured and easily readable report. In order to ease the evaluation of the thesis, it is important that the cross-references are correct. In the making of the report, strong emphasis should be placed on both a thorough discussion of the results and an orderly presentation.

The candidate is requested to initiate and keep close contact with his/her academic supervisor(s) throughout the working period. The candidate must follow the rules and regulations of NTNU as well as passive directions given by the Department of Energy and Process Engineering.

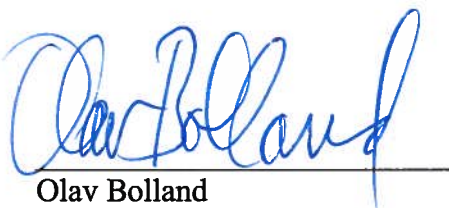
Risk assessment of the candidate's work shall be carried out according to the department's procedures. The risk assessment must be documented and included as part of the final report. Events related to the candidate's work adversely affecting the health, safety or security, must be documented and included as part of the final report. If the documentation on risk assessment represents a large number of pages, the full version is to be submitted electronically to the supervisor and an excerpt is included in the report.

Pursuant to "Regulations concerning the supplementary provisions to the technology study program/Master of Science" at NTNU §20, the Department reserves the permission to utilize all the results and data for teaching and research purposes as well as in future publications.

The final report is to be submitted digitally in DAIM. An executive summary of the thesis including title, student's name, supervisor's name, year, department name, and NTNU's logo and name, shall be submitted to the department as a separate pdf file. Based on an agreement with the supervisor, the final report and other material and documents may be given to the supervisor in digital format.

- Work to be done in lab (Water power lab, Fluids engineering lab, Thermal engineering lab)
 Field work

Department of Energy and Process Engineering, 15. January 2016



Olav Bolland
Department Head



Reidar Kristoffersen
Academic Supervisor

Research Advisor:

Maria Nissrin Foshaug, Kongsberg Maritime AS

Preface

This master thesis was written at the Department of Energy and Process Engineering at the Norwegian University of Science and Technology during the spring of 2016.

I would like to thank my supervisor prof. Reidar Kristoffersen for his support and guidance during this semester. Moreover, I have to thank the company Kongsberg Maritime, especially Maria Nissrin Foshaug and Audun Lønmo Knudsrød for giving me such interesting problem to solve, as well as their support.

It was very challenging and educative work which gave me a great insight into aerodynamics and numerical flow analysis.

Summary

Kongsberg Maritime AS is a company mostly involved in selling automation and equipment to ships and oil rigs. They are considered with wind power as well and started program "WiVind" which main goal is to develop a surface mounted sensor on a wind turbine to help with damage detection. The sensor will be affected by wind which will produce aerodynamic forces and change the flow over a blade of the wind turbine.

The main goal of this master thesis is to investigate the forces acting on the sensor body and check how the flow will be changed by this obstacle. Simulations and calculations will be done by using CFD software COMSOL Multiphysics 5.2.

A literature study was carried out to understand aerodynamics in external flows around blunt bodies and how models should be implemented in CFD software. Initial 2D simulations were performed in order to choose turbulence model and find the most optimal cross-section of the sensor. This study showed that the best sensor had a smooth surface without any sharp edges and the k omega SST turbulence model gave the best results.

Next the 3D simulations of the sensor model mounted on an actual wind turbine blade were carried out. A few approximations were made in order to reduce computational time. With these approximations it was possible to simulate flow only over a part of the wind turbine blade with the sensor mounted on it. Results showed that, for the proposed sensor shapes, force coefficients were very similar which means the total force was only affected by the total area of the sensor, not its shape. The placement of the sensor can affect the flow. Sensor mounted close to the place where the thickness of the blade is highest could drastically influence the flow by creating a large separation area which could reduce the efficiency of the wind turbine.

The NAFNoise noise prediction code, made by NREL institute, was used to predict the Aeroacoustics of the wind turbine blade. This code could only be used for part of the wind turbine but it should not affect the results too much. Calculations were performed for different freestream wind velocities.

Icing problem was checked by using the icing maps made by the Kjeller Vindteknikk company which used WRF model to estimate ice risk in a given area. In the Hundhammerfjellet Wind Farm based on these maps icing problem should occur 200 hours per year.

Sammendrag

Kongsberg Maritime AS er en bedrift fortrinnsvis involvert i salg av automatisering og utstyr for skip og oljeplattformer. De er interessert i vind-energi og startet programmet "WiVind" med hovedmål å utvikle en overflate-montert sensor på vindturbiner til hjelp med skade-deteksjon. Sensoren vill bli påvirket av vind som vil generere aerodynamiske krefter og påvirke strømmingen over vingen til vindturbinen.

Hovedformålet med denne masteroppgaven er å undersøke kreftene på sensoren og se hvordan strømmingen vil bli endret av forhindringen sensoren utgjør. Simuleringer og beregninger vil bli gjort med CFD programvare COMSOL Multiphysics 5.2.

Et litteraturstudie ble gjennomført for å forstå aerodynamikken i eksterne strømminger rundt butte legemer, og hvordan ulike modeller brukes i CFD programvare. Først ble 2D simuleringer gjennomført for å velge turbulensmodell og finne et optimalt tverrsnitt av sensoren. De beste resultatene fra dette studiet var med en sensor med jevn overflate uten skarpe kanter og med k-omega SST turbulens-modell.

Deretter ble 3D simuleringer av sensor-modellen montert på et turbinblad gjennomført. Noen få forenklinger ble gjort for å redusere beregningstiden. Med disse forenklingene var det mulig å simulere strømmingen over kun en del av turbin-bladet med sensoren montert. Resultatene viste at de ulike forslagene for sensor-design ga svært like kraft-koeffisienter, som betyr at kreftene på sensoren er kun avhengig av front-arealet av sensoren, ikke av formen.

Plasseringen av sensoren kan påvirke strømmingen. En sensor montert nær turbinbladets største tykkelse kan påvirke strømmingen med et stort separasjonsområde som igjen kan redusere effektiviteten til vindturbinen.

NAFNoise, et støy-prediksjonsprogram lagd av NREL instituttet, ble brukt for å predikere aero-akustikken fra vind-turbinbladet. Dette programmet kunne bare bli brukt for deler av vindturbinen, men det burde ikke påvirke resultatene for mye. Simuleringer ble utført med forskjellige fristrøms hastigheter.

Problemer med ising ble undersøkt ved hjelp av isings-kart laget av Kjeller Vindteknikk som har brukt WRF modeller for å estimere risikoen for ising i et gitt område. Basert på disse kartene vil ising i området for Hundhammerfjellet vind-farm opptre 200 timer per år.

Contents

Preface	I
Summary	II
Sammendrag	III
List of Figures	VII
List of Tables	XI
Nomenclature	XII
1. Introduction	1
2. Theory	2
2.1. Drag and lift force	2
2.2. Drag and lift coefficients.....	3
2.3. Flow separation and vortex shedding.....	4
2.4. Influence of the parameters of the environmental air to the flow parameters.....	5
2.5. Computational Fluid Dynamics	7
2.5.1. Governing Equations	7
2.5.2. Boundary Conditions	7
2.5.3. Turbulence Modeling.....	8
2.6. Aero-acoustics.....	11
2.6.1. Turbulent Boundary Layer Trailing Edge (TBL-TE)	12
2.6.2. Separated Flow.....	13
2.6.3. Laminar Boundary Layer Vortex Shedding (LBL-VS).....	13
2.6.4. Trailing-Edge Bluntness Vortex Shedding (TEB-VS)	14
2.6.5. Tip Vortex Formation	14
2.6.6. Turbulent Inflow	15
2.7. Occurrence and detection of ice	16
2.7.1. Rime.....	19
2.7.2. Glaze	20

2.7.3.	Wet snow	20
2.7.4.	Hoar frost	21
3.	CFD analysis of the 2D simulations	22
3.1.	Mesh generation	22
3.2.	Flow over a cylinder.....	22
3.2.1.	Geometry of the domain and boundary conditions.....	23
3.2.2.	Verification and validation of the laminar flow.....	23
3.2.3.	Verification and validation of the turbulent flow	27
3.3.	Flow over a cylindrical sensor mounted on flat surface.....	32
3.3.1.	Geometry of the domain and boundary conditions.....	32
3.3.2.	Verification and validation of laminar flow.....	32
3.3.3.	Verification and validation of turbulent flow	34
3.4.	Flow over a cylindrical sensor mounted on a flat surface with elevation.....	37
3.4.1.	Geometry and boundary conditions	37
3.4.2.	Verification and validation of laminar flow.....	37
3.4.3.	Verification and validation of turbulent flow	39
3.5.	Analysis of the designed sensors.....	42
3.6.	Results and discussion.....	44
3.6.1.	Simulation of the flow	44
3.6.2.	Drag and lift coefficients and forces.....	46
4.	Analysis of the 3D CFD simulations	47
4.1.	Wind turbine blade model and sensor locations.....	47
4.2.	Sensors geometry	51
4.3.	Control volume and boundary conditions	52
4.4.	Mesh validation.....	56
4.5.	Results and discussion.....	57
4.5.1.	Aerodynamics	57

4.5.2. Aeroacoustics	66
4.5.3. Icing problem	70
5. Conclusions.....	72
6. Further work.....	74
7. References.....	75
Appendix A	76

List of Figures

Figure 2.1 Forces acting on the airfoil drag (D), lift (L) and angle of attack (α) [2].....	2
Figure 2.2 Real fluid flow about an airfoil. The thickness of the boundary layers and wake are greatly exaggerated. The bottom flow along lower surface is the same as on the upper surface. [13]	5
Figure 2.3 Type of accreted ice as a function of wind speed and air temperature [15].....	19
Figure 3.1 Mesh structure for COMSOL on the upper left for laminar flow, upper right: k epsilon and below k omega SST	22
Figure 3.2 Geometry of the flow around a cylinder and boundary conditions	23
Figure 3.3 Velocity, on the left, and pressure, on the right, field of the laminar flow over a cylinder	24
Figure 3.4 Karman vortex sheet behind the cylinder for $Re=200$. Photograph by Gary Koopman [4].....	24
Figure 3.5 Plot of Strouhal number to the Reynolds number for cylinders with different diameter.....	25
Figure 3.6 Drag and lift coefficients for laminar flow over a cylinder	25
Figure 3.7 Log-log plot of drag coefficient C_d as a function of Reynolds number Re for spheres, transverse cylinders and face-on discs. The broken straight line represents Stoke's law.....	26
Figure 3.8 Oscillations of the drag and lift coefficients for the laminar flow over a cylinder on the left	27
Figure 3.9 Velocity, on the left and pressure, in the right, field of the k epsilon turbulence model of the flow over a cylinder	28
Figure 3.10 Velocity, on the left and pressure, in the right, field of the k omega SST turbulence model of the flow over a cylinder	28
Figure 3.11 Flow past a cylinder for $Re=10000$. Photograph made by Thomas Corke and Hassan Nagib [4].....	28
Figure 3.12 Drag and lift coefficient for turbulent flow over a cylinder using k epsilon turbulence model (on the left) and k omega SST turbulence model (on the right)	29
Figure 3.13 Time history of drag and lift coefficient for the flow past stationary cylinder at $Re = 10000$. Simulation done using DNS [6]	29
Figure 3.14 Oscillations of drag and lift coefficient for turbulent flow over a cylinder using k epsilon turbulence model (on the left) and k omega SST model (on the right).....	30

Figure 3.15 Turbulent k epsilon and k omega SST models for flow over a cylinder – y^+ value.....	30
Figure 3.16 Geometry of the domain and boundary conditions for flow over a cylindrical sensor mounted on flat surface	32
Figure 3.17 Velocity, on the left, and pressure, on the right, field of the laminar flow over a cylindrical sensor mounted on flat surface.....	33
Figure 3.18 Velocity with velocity indicators, on the left, and pressure, on the right, field of the k epsilon turbulent flow over a cylindrical sensor mounted on flat surface	34
Figure 3.19 Velocity with velocity indicators, on the left, and pressure, on the right, field of the k omega SST turbulent flow over a cylindrical sensor mounted on flat surface	34
Figure 3.20 Turbulent k epsilon and k omega SST models for flow over a cylindrical sensor mounted on flat surface – y^+ value	35
Figure 3.21 Geometry of the domain and boundary conditions for flow over a cylindrical sensor mounted on a flat surface with elevation	37
Figure 3.22 Velocity with velocity indicators and pressure field of the laminar flow over a cylindrical sensor mounted on a flat surface with elevation.....	38
Figure 3.23 Velocity with velocity indicators and pressure field of the turbulent k epsilon flow over a cylindrical sensor mounted on a flat surface with elevation.....	39
Figure 3.24 Velocity with velocity indicators and pressure field of the turbulent k omega SST flow over a cylindrical sensor mounted on a flat surface with elevation.....	39
Figure 3.25 Turbulent k epsilon and k omega SST models for flow over a cylindrical sensor mounted on flat surface – y^+ value	40
Figure 3.26 Geometries of designed sensor respectively from up for first model, second and third.....	43
Figure 3.27 Velocity field with velocity indicators for flow over the first model of the sensor	44
Figure 3.28 Velocity field with velocity indicators for flow over the second model of the sensor	44
Figure 3.29 Velocity field with velocity indicators for flow over the third model of the sensor	45
Figure 4.1 Placement of the sensor on the wind turbine blade.	48
Figure 4.2 Blade definition	48
Figure 4.3 Wind turbine blade tip	49
Figure 4.4 Trailing edge before change	50

Figure 4.5 Trailing edge after change	50
Figure 4.6 Ignored cylindrical area near the blade root	50
Figure 4.7 Geometry of the first sensor model	51
Figure 4.8 Geometry of the second sensor model.....	52
Figure 4.9 Flow simulation of flow through a wind turbine.....	53
Figure 4.10 Rectangular domain used for the initial NACA0012 aeroacoustic simulations showing the boundary conditions. The chord length of the airfoil is C and the span is 1/4 S [16].....	54
Figure 4.11 Pressure field and velocity field with velocity vector indicators for sensor mounted 19 m from the blade root. First sensor model on the top and the second below.	58
Figure 4.12 Streamlines for model with 19 meter distance to the blade root. On top is the first sensor model below the second.	59
Figure 4.13 Velocity with velocity vector indicators and pressure field for sensor model places 19 meters from the blade root for both sensor models with first on the top and second below.....	60
Figure 4.14 Velocity and pressure fields alongside the wind turbine blade for the first sensor model located, from the top: 19, 27, 34, 42.8 meters from the blade root.....	61
Figure 4.15 Velocity and pressure fields alongside the wind turbine blade for second sensor model located, 19meters from the blade root.....	62
Figure 4.16 Pressure distribution on the blade surface around the sensors with the 19 meter distance from the blade root.....	62
Figure 4.17 Pressure field and velocity field with velocity vector indicators for sensor mounted 19 meters from the blade root near the critical position. First sensor model on the top and the second below.....	64
Figure 4.18 Pressure distribution on the blade surface around the sensors with the 19 meter distance from the blade root placed near the critical position	65
Figure 4.19 Comparison of the NAFNoise simulation with different span of the blade ...	67
Figure 4.20 Comparison of total sound pressure levels for different freestream velocities for all sensor locations	69
Figure 4.21 Icing map provided by Kjeller Vindteknikk company. Location of the wind turbine farm is marked with red square	71
Figure A.1 Velocity with velocity vector indicators and pressure field for sensor model places 27 meters from the blade root for both sensor models with first on the top and second below.....	76

Figure A.2 Velocity with velocity vector indicators and pressure field for sensor model places 34 meters from the blade root for both sensor models with first on the top and second below.....77

Figure A.3 Velocity with velocity vector indicators and pressure field for sensor model places 42.8 meters from the blade root for both sensor models with first on the top and second below.....77

Figure A.4 Velocity and pressure fields alongside the wind turbine blade for second sensor model located, 27 meters from the blade root.....78

Figure A.5 Velocity and pressure fields alongside the wind turbine blade for second sensor model located, 34 meters from the blade root.....78

Figure A.6 Velocity and pressure fields alongside the wind turbine blade for second sensor model located, 42.8 meters from the blade root.....78

Figure A.7 Pressure distribution on the blade surface around the sensors with the 27 meter distance from the blade root.....79

Figure A.8 Pressure distribution on the blade surface around the sensors with the 34 meter distance from the blade root.....79

Figure A.9 Pressure distribution on the blade surface around the sensors with the 42.8 meter distance from the blade root.....79

List of Tables

Table 2.1 Effect of temperature on properties of air at 1 atm.....	6
Table 2.2 Typical properties of accreted atmospheric ice	18
Table 2.3 Meteorological parameters controlling atmospheric ice accretion	18
Table 3.1 Control volume test for laminar flow over a cylinder test case	27
Table 3.2 Mesh independency test for laminar flow over a cylinder test case	27
Table 3.3 Control volume test for turbulent flow over a cylinder test case.....	31
Table 3.4 Mesh independency test for turbulent flow over a cylinder test case	31
Table 3.5 Control volume test for laminar flow a cylindrical sensor mounted on flat surface.	33
Table 3.6 Mesh independency test for laminar flow over a cylindrical sensor mounted on flat surface.....	34
Table 3.7 Control volume test for turbulent flow over a cylindrical sensor mounted on flat surface	36
Table 3.8 Mesh independency test for turbulent flow over a cylindrical sensor mounted on flat surface.....	36
Table 3.9 Control volume test for laminar flow a cylindrical sensor mounted on flat surface with elevation.....	38
Table 3.10 Mesh independency test for laminar flow over a cylindrical sensor mounted on flat surface with elevation	38
Table 3.11 Control volume test for turbulent flow over a cylindrical sensor mounted on flat surface with elevation	41
Table 3.12 Mesh independency test for turbulent flow over a cylindrical sensor mounted on flat surface with elevation.....	41
Table 3.13 Forces and coefficients of drag and lift for designed sensors.....	46
Table 4.1 Control volume check for first sensors model in all locations on the wind turbine	55
Table 4.2 Mesh independence check for the first sensor model in all locations on the wind turbine blade.....	56
Table 4.3 Aerodynamic forces for both sensors in all locations on the wind turbine blade	63
Table 4.4 Aerodynamic forces for both sensors placed near the critical position with 19 meter distance from the blade root.....	65
Table 4.5 Parameters used in the NAFNoise - noise prediction code for airfoils	66

Nomenclature

F_d	drag force	f_{vs}	frequency of vortex shedding
F_l	lift force	f_{cd}	frequency of drag coefficient oscillations
F_r	radial force	f_{cl}	frequency of lift coefficient oscillations
α	angle of attack	y^+	dimensionless wall distance
A	reference area	l_t	first layer thickness
L	reference length	κ	von Karman constant
C_d	drag coefficient	E	roughness of the wall constant
C_l	lift coefficient	Abbreviations	
C_r	radial force coefficient	CFD	Computational Fluid Dynamics
U	freestream velocity	RANS	Reynolds Averaging Navier-Stokes
ρ	density of the fluid	DNS	Direct Numerical Simulation
$R_{\text{specific air}}$	specific gas constant for dry air	SST	Shear Stress Transport
T	absolute temperature	WRF	Weather Reference Forecast
p	absolute pressure	SPL	Sound Pressure Level
τ_w	shear stress		
μ	dynamic viscosity		
ν	kinematic viscosity		
k	turbulent kinetic energy		
ε	turbulent dissipation rate		
ω	specific dissipation rate		
Re	Reynolds number		
St	Strouhal number		

1. Introduction

Kongsberg Maritime AS (just called “KM” from now) is a Norwegian company owned by the Kongsberg Group, a company which is owned by the Norwegian Government.

KM is mainly involved in selling automation and instrumentation equipment to ships and oil rigs. It also has some interest in wind power. The WiVind project is part of that interest, and aims to develop sensors that can be used to analyze the state/wellbeing of a wind turbine blade and detect damages to the blade.

The WiVind project will develop surface-mounted sensors for wind turbine blades that will transmit wireless data to a host system, which in turn can warn an operator if something is wrong. This will allow the owner of the wind turbines to plan repairs and maintenance in advance, before serious damage has occurred.

In this study the aerodynamics of the sensor will be checked. It is important that the air forces as drag or lift will not be able to blow away the sensor. The main task in this work is to familiarize with the aerodynamics and CFD programs such as COMSOL Multiphysics 5.2. This program should help calculate the forces acting on the sensors and provide better understanding of the flow which can be hard to predict.

Aeroacoustics and icing risk should be checked. Both features can highly affect work of the sensor by changing the results by creating mechanical oscillations in the airflow and physically changing flow by ice loads.

2. Theory

2.1. Drag and lift force

Drag is a force that opposes motion. This force acts on a body in the flow direction. Fluid exerts a pressure force which is normal to the surface of an immersed body. Motion between the body surface and the fluid causes a tangential shear force due to the viscosity (assuming no-slip condition). That means the drag force is combined effect of pressure, P , and shear stress, τ_w , acting in the flow direction (1):

$$dF_D = PdA\cos\theta + \tau_w dA\sin\theta \quad (1)$$

where

dA is a element of surface area

Θ is angle between pressure force and horizontal line

Lift Force is similar to the drag force but it is an effect of pressure and shear stresses acting perpendicularly to the direction of the flow of the fluid, Lift tries to change the direction of motion (2):

$$dF_L = PdA\sin\theta + \tau_w dA\cos\theta \quad (2)$$

Figure 2.1 is an example of pressure fields and shear force acting on an airfoil and forces.

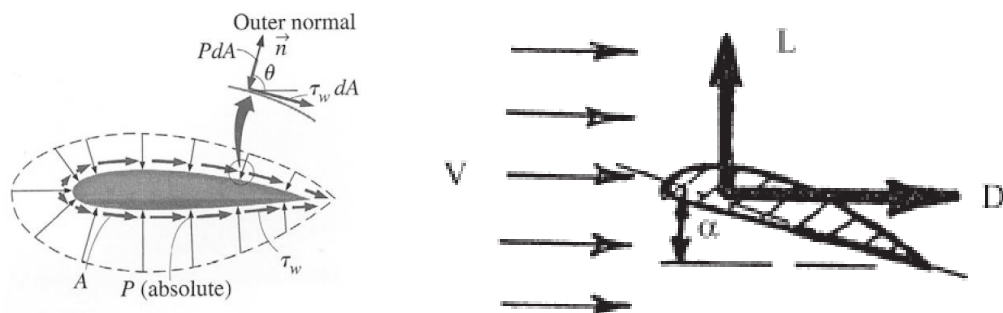


Figure 2.1 Forces acting on the airfoil drag (D), lift (L) and angle of attack (α) [2]

The shape of the body has a significant influence on the relative magnitude of the Drag and Lift components. A thin body (small height to length ratio) will cause less pressure drag, all drag force comes from skin friction (viscous component of drag force). On the other side a thick body (large height to length ratio) where the flow separation most likely will occur, the pressure drag will be dominant.

To avoid separations which decrease pressure drag considerably this body can be streamlined. On the other hand, in case of a flat plate normal to the flow, the pressure drag will dominate over the viscous drag.

For the most blunt bodies, which are not streamlined, drag force is primarily from pressure, due to much higher pressure at the front of the body than on the rear.

In this study, especially with the 3D approach, it is important to remember there could generate additional force acting in the radial direction in the wind turbine, though the blade. This force will be called radial force - F_r .

2.2. Drag and lift coefficients

The drag coefficient, C_d , is a dimensionless number that aerodynamicists use to model all of the complex dependencies of shape, inclination, and flow conditions on the drag force. The drag coefficient C_d is equal to the drag force F_d divided by the dynamic pressure times a reference area A . For 2D case it can be assumed that $A=L$, where L is characteristic length given by the equation (3):

$$C_d = \frac{F_d}{0.5A\rho U^2} \quad (3)$$

where

U is freestream velocity

ρ is density of the fluid

The lift coefficient C_l is calculated in the same way but for lift force F_l in the place of a drag force, (4):

$$C_l = \frac{F_l}{0.5A\rho U^2} \quad (4)$$

The choice of reference area (for example: wing area, frontal area, surface area) or length (for example: diameter of a circular body) is very important and it will affect the actual numerical value of the drag coefficient that is calculated. Therefore, when reporting drag or lift coefficient values, it is important to specify the reference area or length that was used to determine that coefficient.

These coefficients allows to predict the drag or lift force that will be produced under a different set of velocity, density, and area or length conditions for the body with the same

shape using the above equations. Additionally the radial force coefficient has the same approach as the other forces, (5):

$$C_r = \frac{F_r}{0.5A\rho U^2} \quad (5)$$

2.3. Flow separation and vortex shedding

Flows around bluff body are characterized by flow separation which produces a region of disturbed flow behind, i.e. the wake. This disruption is created when fluid curves too much and a region of adverse pressure gradient – pressure increases in the downstream direction. Within the near-wake various forms of flow instabilities, both convective and absolute, may be triggered and amplified. These instabilities are manifested by the generation of two- and three-dimensional unsteady flow structures and eventually turbulence as the Reynolds number is progressively increased. The most well-known instability is that leading to the periodic formation and shedding of spanwise vortices which produces an impressive wake pattern named after von Kármán and Benhard. The frequency of vortex shedding is characterized by the Strouhal number (6):

$$St = \frac{f_{vs} D}{U} \quad (6)$$

where

f_{vs} is frequency of vortex shedding

This number is a function of the Reynolds number, $St(Re)$. Bluff body flows involve the interaction of three shear layers, namely the boundary layer, the separating free shear layers and the wake. The physics of vortex formation and the near-wake flow have been the subject of numerous experimental and numerical studies which have provided a wealth of information. The basic mechanism of vortex formation is essentially two dimensional although there are inherent three-dimensional features for Reynolds numbers above 190. As well as contributing to time-averaged aerodynamic forces, vortex shedding is responsible for the generation of fluctuating forces acting on the body. This has several consequences in practical applications as it may excite flow-induced vibration and acoustic noise.

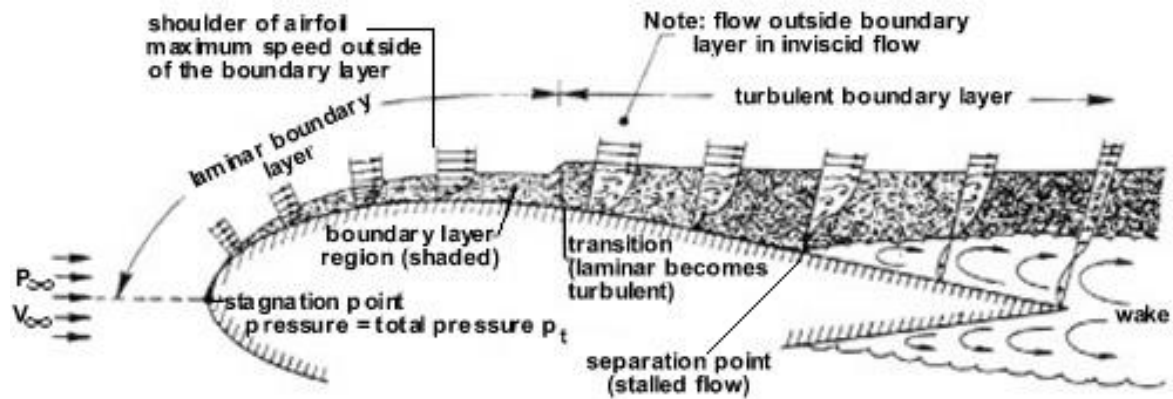


Figure 2.2 Real fluid flow about an airfoil. The thickness of the boundary layers and wake are greatly exaggerated. The bottom flow along lower surface is the same as on the upper surface [13]

The boundary layer leaves the surface approximately in tangential direction, resulting in a wedge shaped separation area. The separated, but still laminar flow is highly sensitive to disturbances, which finally cause it to transition to the turbulent state. The transition region is located away from the airfoil at the outer boundary of the separated flow area. The thickness of the now turbulent boundary layer grows rapidly, forming a turbulent wedge, which may reach the airfoil surface again. The region where the turbulent flow touches the surface again is called reattachment point. The volume enclosed by the regions of separated laminar flow and turbulent flow is called a laminar separation bubble. Inside the bubble the flow may be circulating, the direction near the airfoil surface may even be the opposite of the direction of the outer flow. There is almost no energy exchange with the outer flow, which makes the laminar separation bubble quite stable. Separation bubbles might appear at low Reynolds numbers [14].

2.4. Influence of the parameters of the environmental air to the flow parameters

Temperature

The density of dry air can be calculated using the ideal gas law, expressed as a function of temperature and pressure (7):

$$\rho = \frac{p}{R_{specific} T} \quad (7)$$

where:

ρ - air density [kg/m³]

p - absolute pressure [Pa]

T - absolute temperature [K]

R_{specific} - specific gas constant for dry air [J/(kg*K)]

The specific gas constant for dry air is 287.058 J/(kg·K) in SI units. This quantity may vary slightly depending on the molecular composition of air at a particular location.

At 20°C and 101.325 kPa, dry air has a density of 1.2041 [kg/m³].

As goes for viscosity widely used Sutherland Equation is given by (8):

$$\mu = \frac{bT^{\frac{3}{2}}}{T + S} \quad (8)$$

where

b and S are coefficients and constants, for air:

$b=1.458 \cdot 10^{-6}$ [kg/(m*s*K^{1/2})]

$S=110.4$ [K]

Table 2.1 Effect of temperature on properties of air at 1 atm

Temperature T [°C]	Density of air ρ [kg/m ³]	Absolute (dynamic) viscosity μ [Pa·s] *10 ⁻⁵
35	1.1455	1.88431
30	1.1644	1.86087
25	1.1839	1.83723
20	1.2041	1.81341
15	1.225	1.78938
10	1.2466	1.76515
5	1.269	1.74072
0	1.2922	1.71608
-5	1.3163	1.69122
-10	1.3413	1.66615
-15	1.3673	1.64085
-20	1.3943	1.61533
-25	1.4224	1.58957

2.5. Computational Fluid Dynamics

Computational fluid dynamics is a branch of fluid mechanics that uses numerical analysis and algorithms to solve and analyze problems that involve fluid flows. Computers are used to perform the calculations required to simulate the interaction of liquids and gases with surfaces defined by boundary conditions. With high-speed supercomputers, better solutions can be achieved. Ongoing research yields software that improves the accuracy and speed of complex simulation scenarios such as transonic or turbulent flows. Initial experimental validation of such software is performed using a wind tunnel with the final validation coming in full-scale testing, e.g. flight tests.

The fundamental basis of almost all CFD problems are the Navier–Stokes equations, which define any single-phase (gas or liquid, but not both) fluid flow.

2.5.1. Governing Equations

The governing equations of fluid flow are:

- Conservation of Mass
- Conservation of Momentum
- Conservation of Energy

In the process for the numerical approach solution, fluids are considered as a continuum, the substance which fills the given space it occupies. The computational domain is divided into a certain number of small elements, where the elements are large enough, compared with the sizes of the molecules, to treat the fluid as a continuum. These elements are called fluid elements [11]. All of the governing equations must be satisfied for fluid in any position or motion through time.

2.5.2. Boundary Conditions

All CFD problems are defined in terms of initial and boundary conditions. It is very important to specify these correctly to save some computational time and to reach convergence.

Inlet boundary condition – at this boundary condition all distribution of all flow variables needs to be specified. In our cases for laminar flow it can be assumed that

$u = [u_0 \ 0 \ 0]$ and $\frac{\partial p}{\partial n} = 0$ as goes for turbulence it is needed to add values for variables of transport equations, for k-epsilon turbulence model: k and epsilon and for k omega SST model: k and omega.

Outlet boundary condition – here it can be assumed that all the gradients of all variables are equal zero (for example $\frac{\partial u}{\partial n} = 0$) except pressure.

Wall boundary condition – for most cases there is used no slip condition, that means on the wall $u = v = 0$. Some turbulence models are using the wall functions instead. Wall functions are used in the turbulence modeling to save a lot of computing time and they allow using coarser mesh near walls. Extremely close to the wall there is very thin viscous sub-layer followed by buffer layer and the turbulent core. To implement these functions viscous distance from the wall y^+ needs to be evaluated where y^+ is given by (9):

$$y^+ = \frac{\Delta y_p}{\nu} \sqrt{\frac{\tau_w}{\rho}} \quad (9)$$

where

Δy_p is the distance of the near wall node to the solid surface.

Symmetry boundary condition – conditions for this boundary are:

- no flow across the boundary
- no scalar flux across the boundary

In this case to fulfill these conditions it is assumed that on the symmetry boundary gradients

for pressure $\frac{\partial p}{\partial n} = 0$ and velocity $\frac{\partial u}{\partial n} = 0$.

2.5.3. Turbulence Modeling

It is assumed that the flow is turbulent if the Reynolds number is higher than 2300 where this number is given by equation (10):

$$Re = \frac{\rho UL}{\mu} \quad (10)$$

where

ρ is density of the air

U is freestream velocity of the air

L is characteristic length of the model

μ is dynamic viscosity of the air

From a variety of existing turbulence models k epsilon RANS model was chosen. The k epsilon turbulence model focuses on the mechanism that affect the turbulent kinetic energy. This is a two equation model which means that it needs two additional transport equation models to be solved, the turbulent kinetic energy k and turbulent dissipation rate ϵ .

The k epsilon model is the most widely used and validated turbulence model. It has achieved notable success in calculating a wide variety of thin shear layer and reticulating flows without the need for case-by case adjustment of the model constants. The model performs particularly well in confined flows where the Reynolds shear stresses are most important. This includes a wide range of flows with industrial engineering applications, which explains its popularity.

For the COMSOL it is taken that a near wall flow is laminar is $y^+ \leq 11.06$. The wall shear stress is assumed to be entirely viscous in origin. And for $y^+ > 11.06$ the flow is turbulent and the wall function approach is used. The criterion places the changeover from laminar to turbulent near wall flow in the buffer layer between the linear and log-law regions of a turbulent wall layer. It is assumed that $y^+ = 11.06$ is the intersection of the linear profile and the log-law. This value was obtained from (11):

$$y^+ = \frac{1}{\kappa} \ln(Ey^+) \quad (11)$$

where κ is von Karman constant equal 0.4187 and E is an integration constant that depends on the roughness of the wall, for smooth walls with constant shear stress E has value of 9.793.

Initial values for k and ϵ which are a part of transport equations are computed by segregated solver. The nonlinear system that the Navier-Stokes (RANS) and turbulence transport equations constitute can become ill-conditioned if solved using a fully coupled

solver. Turbulent flows are therefore solved using a segregated approach: Navier-Stokes in one group and the turbulence transport equations in another. For each iteration in the Navier-Stokes group, two or three iterations are performed for the turbulence transport equations. This is necessary to make sure that the very nonlinear source terms in the turbulence transport equations are in balance before performing another iteration for the Navier-Stokes group. The default iterative solver for the turbulence transport equations is GMRES accelerated by Geometric Multigrid. The default smoother is SOR Line [7].

Advantages:

- This is one of the simplest turbulence models for which only initial and boundary conditions need to be supplied.
- Excellent performance for many industrially relevant flows
- Well established

Disadvantages:

- Poor performance in a variety of important cases such as: some unconfined flows, flows with large extra strains, rotating flows, fully developed flows in non-circular ducts.

To check the validity of used k epsilon model a more advanced model will be used as well – k omega SST, where SST stands for Shear Stress Transport. This is a two equation model as well which combines the two turbulence models k omega in the inner parts of the boundary layer (it makes model usable all the way down to the viscous sublayer) and k epsilon in the free stream area. The SST k- ω model does produce a bit too large turbulence levels in regions with large normal strain, like stagnation regions and regions with strong acceleration. This tendency is much less pronounced than with a normal k - ϵ model though. This model uses wall functions as well but is more accurate with $y^+ \leq 2$. Initial values of k and omega are computed by segregated solver as for the k epsilon model for COMSOL.

2.6. Aero-acoustics

Due to the nonlinearity of the governing equations it is very difficult to predict the sound production of fluid flows. This sound production occurs typically at high speed flows, for which nonlinear inertial terms in the equation of motion are much larger than the viscous terms (high Reynolds numbers). As sound production represents only a very minute fraction of the energy in the flow the direct prediction of sound generation is very difficult. The fact that the sound field is in some sense a small perturbation of the flow can however be used to obtain approximate solutions.

To predict aeroacoustics NAFNoise code by Pat Moriarty will be used. From User Guide for this code [8]: "NAFNoise, which stands for NREL AirFoil Noise, is a program that predicts the noise of any airfoil shape for five different types of noise sources: turbulent boundary layer trailing-edge noise, separated flow noise, laminar boundary layer vortex-shedding noise, trailing-edge bluntness noise, and turbulent inflow noise. The models in the program are based on the work of others and recently performed research at NREL. Empirical models for the first four noise sources (everything except turbulent inflow noise) were originally developed by Brooks, Pope and Marcolini, based on their detailed measurements of noise from NACA 0012 airfoils. An empirical model for the turbulent inflow noise is based on the work of Amiet. Recent improvement of these models, has included the modeling of any airfoil shape by using the boundary layer calculations of Xfoil, developed by Drela. These boundary layer predictions can be used as inputs into the models of Brooks, Pope, and Marcolini or into a newly developed model for trailing edge noise by researchers at TNO. Two final modifications to the empirical models are the introduction of a turbulent inflow noise correction developed by Guidati and a simplified version of the same Guidati method that is less computationally intensive. The Guidati method corrects the Amiet method for turbulent inflow noise to account for airfoil shape.(...)"

Each semi-empirical model relates the properties of the flow field and turbine geometry to a resulting sound pressure level (SPL). The SPL, given in units of dB, is proportional to the logarithm of the ratio of sound intensity (or mean square pressure) to a reference value (12):

$$SPL = 10 \log\left(\frac{I}{I_{ref}}\right) = 20 \log\left(\frac{p}{p_{ref}}\right) \quad (12)$$

where I is the sound intensity, and p is the root mean square sound pressure. The reference root mean square pressure is $20 \mu\text{Pa}$.

Each of the semi-empirical models was developed for a single two-dimensional airfoil. In order to calculate the aerodynamic noise radiating from a wind turbine rotor, the rotor blades are first discretized into many individual segments. Using local flow velocities and angles of attack, the sound pressure level for each segment and noise source is then calculated relative to an observer position. Finally, the sound pressure level from each of the individual sources is summed across the blade to calculate the total noise signature of the rotor. For the semi-empirical models to be applicable, the segments are assumed to operate in predominantly two-dimensional flow. This is largely true for outboard blade sections, which tend to dominate the noise production. The flow over the segments is also assumed to be quasi-steady, such that the mechanisms that produce noise are stationary at each time step in the simulation.

2.6.1. Turbulent Boundary Layer Trailing Edge (TBL-TE)

The first, and perhaps most common, source of noise from an airfoil, results from the interaction between the turbulent boundary layer and the trailing edge of the airfoil, especially at higher Reynolds numbers. Based on their measurements, Brooks, Pope, and Marcolini formulated empirical relations to predict these noise sources based on the edge-scatter formulation of Ffowcs-Williams and Hall [5]. These relations account for the noise intensity being directly proportional to the turbulent boundary layer displacement thickness, δ^* , and the fifth power of the mean velocity or Mach number, M^5 , and inversely proportional to the square of the distance between the observer and the airfoil trailing edge. There are also corrections for angle of attack and Reynolds number, as well as tripped and untripped boundary layers. Turbulent boundary layer noise can originate on both the suction and pressure side of the airfoil. For the pressure side of the airfoil, the sound pressure level is given as follows (13):

$$SPL_p = 10 \log \left(\frac{\delta_p^* M^5 L \overline{D_n}}{r_e^2} \right) + A \left(\frac{St_p}{St_1} \right) + (K_1 - 3) + \Delta K_1 \quad (13)$$

where $\delta^* = \delta^*(\alpha, Re_c)$ is the boundary layer displacement thickness, in meters [m], based on α , the angle of attack [deg.], and Re_c , the Reynolds number based on chord. The subscript p refers to the pressure side of the airfoil. Other parameters in Equation 2 are L ,

the span of the airfoil section [m]; D_h , the directivity function, r_e , the effective observer distance [m]; and A , an empirical spectral shape based on the Strouhal number $St = (f\delta^*/U)$, where f is the frequency in hertz [Hz], and U is the local mean velocity [m/s]. Three other empirical relations are also used, $St_1 = 0.02M^{0.6}$, $K_1 = K_1(Re_c)$, and $\Delta K_1 = \Delta K_1(\alpha, Re_{\delta^*})$.

A nearly identical formulation is used to calculate the sound pressure level radiating from the suction side of the airfoil.

2.6.2. Separated Flow

As the angle of attack increases from moderate to high, the size of the turbulent boundary layer on the suction side of the airfoil increases dramatically, and large-scale unsteady structures form. These structures can dominate noise production from the trailing edge. When the airfoil is fully separated or stalled, noise radiates from the unsteady flow over the entire chord of the airfoil. This is an important noise source for wind turbines because the blades operate at high angles of attack for significant portions of time. The empirical relation for separated flow noise, denoted SPL_α , is very similar to Equation 2 with different scaling functions for the angle of attack dependence.

The total sound pressure level from the interaction of the turbulent boundary layer with the trailing edge can be determined through simple summation of the three different components: pressure side, suction side, and separated flow (14):

$$SPL_{TBL-TE} = 10 \log \left(10^{\frac{SPL_p}{10}} + 10^{\frac{SPL_S}{10}} + 10^{\frac{SPL_\alpha}{10}} \right) \quad (14)$$

2.6.3. Laminar Boundary Layer Vortex Shedding (LBL-VS)

Another source of airfoil self noise is that of laminar boundary layer vortex shedding. The noise from this source is created by a feedback loop between vortices being shed at the trailing edge and instability waves in the laminar boundary layer upstream of the trailing edge. As a laminar vortex leaves the trailing edge, its pressure waves propagate upstream and amplify instabilities in the boundary layer. When these instabilities reach the trailing edge, vortices with similar frequency content are created, forming a feedback loop. This source of noise is most likely to occur on the pressure side of the airfoil and is somewhat tonal in nature because of feedback amplification. This noise source is probably

not significant for current utility-sized turbines because their blade airfoil sections, particularly near the tips, operate at fairly large Reynolds number (>1 million), but may be important for smaller sized turbines (i.e. <500 kW). The empirical relation for sound pressure level is as follows (15):

$$SPL_{LBL-VS} = 10 \log \left(\frac{\delta_p M^5 L \overline{D_h}}{r_e^2} \right) + G_1 \left(\frac{St'}{St'_{peak}} \right) + G_2 \left(\frac{Re_c}{(Re_c)_o} \right) + G_3(\alpha) \quad (15)$$

where most of the variables are identical to those in Equation 2: δ_p is the boundary layer thickness [m] on the pressure side of the airfoil; G_1 , G_2 , and G_3 are empirical functions; St' is the Strouhal number based on δ_p , $St'_{peak}=St'_{peak}(Re_c)$ and is the peak Strouhal number; and $(Re_c)_o=(Re_c)_o(\alpha)$ is a reference Reynolds number.

2.6.4. Trailing-Edge Bluntness Vortex Shedding (TEB-VS)

Another source of airfoil self noise is vortex shedding from a blunt trailing edge. The frequency and amplitude of this noise source are largely determined by the geometry of the trailing edge. The vortices shed are typically coherent in nature and can produce discrete tones similar to a Von Karman vortex street downstream of cylindrical objects. This noise source will dominate the total radiated noise if the thickness of the trailing edge is significantly larger than the thickness of the boundary layer at the trailing edge. Therefore, in addition to Mach number and boundary layer thickness scaling, the empirical relation to predict sound pressure level also contains functions dependent on the trailing edge thickness, as follows (16):

$$SPL_{TEB-VS} = 10 \log \left(\frac{\delta_p^* M^5 L \overline{D_h}}{r_e^2} \right) + G_4 \left(\frac{h}{\delta_{avg}^*}, \Psi \right) + G_5 \left(\frac{h}{\delta_{avg}^*}, \Psi, \frac{St''}{St''_{peak}} \right) \quad (16)$$

where h is the trailing edge thickness [m]; δ_{avg}^* is the average displacement thickness for both sides of the airfoil [m]; Ψ is the solid angle between both airfoil surfaces just upstream of the trailing edge [deg.]; St'' is the Strouhal number based on h ; $St''_{peak}=St''_{peak}(h/\delta_{avg}^*)$ is the peak Strouhal number; and G_4 and G_5 are empirical functions of these parameters.

2.6.5. Tip Vortex Formation

The interaction of the tip vortex with the blade tip and trailing edge near the tip is also a source of aerodynamic noise. This noise source is different from the previous four sources in that it is three-dimensional in nature. The sound pressure level is a function of

the vortex strength, which is dependent on the spanwise loading on the turbine blade. Typically, the sound pressure levels from tip noise are less than those of trailing edge noise, but tip noise can add significant amounts of noise at higher frequencies. Brooks, Pope, and Marcolini formulated the following relation for an untwisted, constant chord blade (17):

$$SPL_{Tip} = 10 \log \left(\frac{M^2 M_{max}^5 l^2 \overline{D_h}}{r_e^2} \right) - 30.5 (\log St''' + 0.3)^2 + 126 \quad (17)$$

where $M_{max} = M_{max}(\alpha_{tip})$ is the maximum Mach number within the separated flow region near the tip, α_{tip} is the equivalent angle of attack at the tip [deg.], and $l = l(\alpha_{tip})$ is the spanwise extent of the separation zone [m], which is dependent on the spanwise lift distribution and the geometric shape of the tip (rounded or square). St''' is the Strouhal number based on l . Because this relation was formulated for an untwisted, constant chord blade, an equivalent α_{tip} for twisted and tapered blades should be used to produce reliable results. A crude estimate for this parameter can be made by multiplying the geometric α_{tip} by the ratio of the slopes of the spanwise lift distribution for the complex blade shape to that of Brooks, Pope, and Marcolini. If accurate estimates of absolute tip noise were necessary, the user would be required to tune this variable to match measured data, which are not easily obtained.

2.6.6. Turbulent Inflow

For wind-turbine applications, the interaction of the turbulent inflow (produced by the atmospheric boundary layer) with the leading edge of the turbine blades is a significant source of noise, particularly at low frequencies. This noise source becomes important when the length scale of the turbulent eddies is large in comparison to the leading edge radius of an airfoil. In the atmospheric boundary layer, the scales of turbulence vary by several orders of magnitude from approximately 1 mm to larger scales on the order of 100 m, where most of the energy resides.

Depending on the size of the length scale relative to the leading edge radius of the airfoil, turbulent inflow can create either a dipole noise source (low-frequency) with M^6 dependence or a scattered quadruple noise source (high frequency) with M^5 dependence. Lowson formulated an empirical relation for inflow turbulence noise that modeled both the low and high frequency behavior and is based on Amiet's work on experimental airfoil measurements, as follows (18-21):

$$SPL_{Inflow} = SPL_{Inflow}^H + 10 \log\left(\frac{LFC}{1 + LFC}\right) \quad (18)$$

$$SPL_{Inflow}^H = 10 \log\left(\frac{\rho_o^2 c_o^2 l L}{2r_e^2} M^3 u^2 I^2 \frac{K^3}{(1 + K^2)^{\frac{7}{3}}} \overline{D_L}\right) + 58.4 \quad (19)$$

$$LFC = 10S^2 MK^2 \beta^{-2} \quad (20)$$

$$S^2 = \left(\frac{2\pi K}{\beta^2} + \left(1 + 2.4 \frac{K}{\beta^2}\right)^{-1}\right)^{-1} \quad (21)$$

where ρ_o is the air density [kg/m^3]; c_o is the speed of sound [m/s]; l is a turbulence length scale (described in the next paragraph) [m]; u is the mean wind speed [m/s]; I is the turbulence intensity [%]; $K = \pi fc/U$ is the local wave number, where f is the frequency of interest [Hz], c is the local airfoil chord length [m], and U is the local velocity over the airfoil section [m/s]; D_L is a low-frequency directivity function; LFC is a low-frequency correction factor; S is the compressible Sears function; and $\beta^2 = 1 - M^2$.

2.7. Occurrence and detection of ice

Main goal of this section is to describe the different processes and needed conditions that lead to ice accretion on structures in this case wind turbines.

Atmospheric icing is the physical process where drifting or falling water droplets, rain or wet snow freezes upon a surface exposed to the atmosphere, as defined by The International organization for Standardization. The process of atmospheric icing is quite difficult to define, but the widely accepted present definition includes the air temperature, wind speed, liquid water content (LWC) and median volume diameter (MVD) of the water droplets. However, ice accretion is not only a function of meteorological parameters, but also a function of the properties of the actual object exposed to icing, such as size, shape, orientation relative to mean wind direction and flexibility.

Icing most often occurs on objects exposed to the wind at times with freezing temperatures and significant LWC. However, low temperatures alone do not automatically imply ice accretion, water vapor or some form of condensate has to be present in the atmosphere.

When icing conditions are fulfilled, all parts of a wind turbine are exposed to ice accretion. The moving rotor is likely to accrete much larger amounts of ice than the stationary parts. This happens because the rate of ice accretion is dependent on the relative velocity of the super-cooled water droplets and the highest velocities occur at the tip of the rotating blades. The ends of the blades also cover a larger area than the inner parts of the wind turbine resulting in accumulation of the water from a larger volume.

The risk of icing at a specific location can be difficult to predict because regional and local topography highly influence the icing conditions through the vertical motion of air masses. This leads to changes in cloud base height, LWC and hence precipitation. The most severe icing events typically occur at high altitudes relative to the surroundings, where a combination of in-cloud icing and precipitation icing enhances the ice accretion.

Classification and characteristics of ice

Atmospheric icing problem, according to meteorological conditions and air particle properties, is formed by two processes:

- Precipitation icing
- In-cloud icing

Precipitation icing is the freezing of rain or snow upon contact with a surface while in-cloud icing results from the deposition of cloud droplets and water vapor onto a surface. In-cloud icing occurs if the height of the cloud base is less than the elevation of the site and the temperature is below 0°C. Precipitation icing can cause much higher ice accumulation rates than in-cloud icing and though possibly result in a greater damage.

ISO has classified four different types of ice resulting from either of the above processes:

- Glaze
- Rime (hard/soft)
- Wet snow
- Hoar frost

The first three can result in a significant ice accretion on surfaces while hoar frost is generally considered not to, due to created ice low density. The properties of accreted ice can change greatly by influence of meteorological conditions throughout the build-up

period. Different types of ice can form on a structure because of these conditions. Table 2.2 presents typical properties of different types of ice. The maximum ice load accreted during an icing event depends on several factors, the most important are humidity, temperature and duration of the event.

Table 2.2 Typical properties of accreted atmospheric ice

Type of ice	Density [kg/m ³]	Adhesion and Cohesion	General appearance	
			Color	Shape
Glaze	900	Strong	Transparent	Evenly distributed / icicles
Wet snow	300 to 600	Weak (forming) Strong (frozen)	White	Evenly distributed / eccentric
Hard rime	600 to 900	Strong	Opaque	Eccentric, pointing windward
Soft rime	200 to 900	Low to medium	White	Eccentric, pointing windward

Ice types can be further classified using different meteorological parameters, as can be seen in Table 2.3. Here the ice types have been divided into precipitation icing and in-cloud icing as well as by wind speed and ambient temperature.

Table 2.3 Meteorological parameters controlling atmospheric ice accretion

Type of ice	Air temperature [°C]	Wind speed [m/s]	Droplet size	Water content in air	Typical storm duration
Precipitation ice					
Glaze (freezing rain or drizzle)	-10 < Ta < 0	Any	Large	Medium	Hours
Wet Snow	0 < Ta < +3	Any	Flakes	Very high	Hours

Type of ice	Air temperature [°C]	Wind speed [m/s]	Droplet size	Water content in air	Typical storm duration
In-cloud icing					
Glaze	See Figure 2.3	See Figure 2.3	Medium	High	Hours
Hard rime	See Figure 2.3	See Figure 2.3	Medium	Medium	Days
Soft rime	See Figure 2.3	See Figure 2.3	Small	Low	days

Precipitation icing is quite clearly defined, in-cloud icing is more dependent on wind speed as can be seen in Figure 2.3. Depending on temperature and wind speed: glaze, hard and soft rime can form. It should be noted that the curves shift further to the left with increasing LWC and decreasing object size. It should also be noted that icing types on wind turbine blades depend on the velocity, i.e. the radial position on the blade. That means different types of ice can be formed on the blade depending on distance from root.

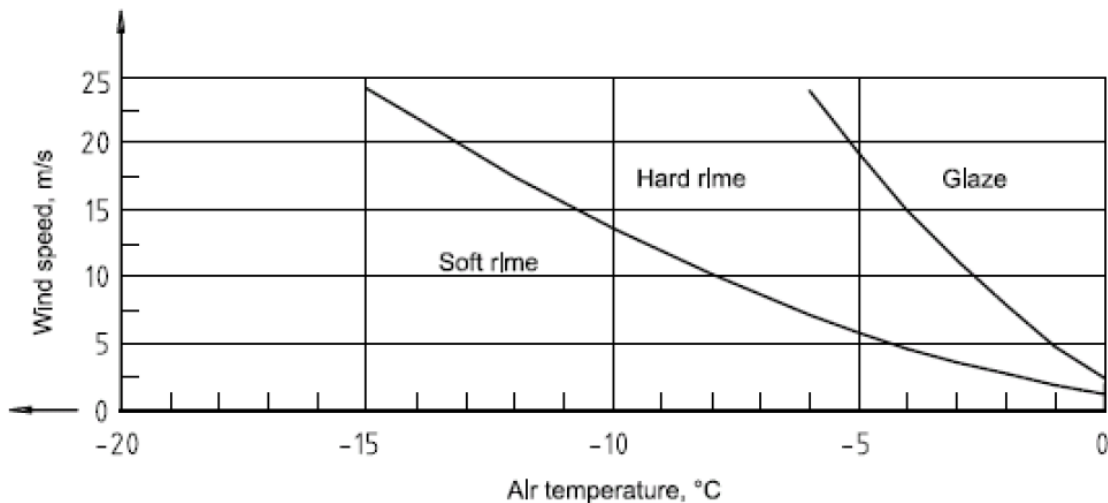


Figure 2.3 Type of accreted ice as a function of wind speed and air temperature [15]

2.7.1. Rime

Rime forms through deposition of super-cooled fog or cloud droplets and is the most common form of in-cloud icing. Depending on droplet size and air temperature during the icing event, rime can form structures of different density and strength, which leads to a division into two sub types of rime – hard and soft (see Table 2.2). Low temperatures and small droplet size typically lead to an ice accretion of low density and low strength.

Soft rime is a white ice deposition that forms when the water droplets in light freezing fog or mist freeze to the outer surfaces of objects, with calm or light wind. The fog freezes usually to the windward side of tree branches, wires, or any other solid objects.

Hard rime is a white ice that forms when the water droplets in fog freeze to the outer surfaces of objects. It is often seen on trees atop mountains and ridges in winter, when low-hanging clouds cause freezing fog. This fog freezes to the windward (wind-facing) side of tree branches, buildings, or any other solid objects, usually with high wind velocities and air temperatures.

Rime icing is common at high altitudes and at low temperatures. The most severe rime icing events occur on freely exposed mountains or hilltops where moist air is forced upwards and consequently cooled or where mountain valleys force moist air through passes which also increases the wind speed.

The rate of accretion mainly depends on wind speed, LWC, droplet size distribution and air temperature. Rime tends to form vanes on the windward side of a static object, which implies that the dimensions of the object affect the total ice load. However, when rime forms on turbine blades it shows remarkable symmetry with no imbalance as a result.

2.7.2. Glaze

Glaze can be formed by either freezing precipitation or in-cloud icing and normally forms smooth, opaque depositions, fairly evenly distributed over the object. It is typically formed as a wet growth process, which means that there is insufficient time for latent heat released by the phase transition to transfer from the surface to the air, and that a liquid coating therefore is formed on the surface. This wet growth leads to a high density, typically in the magnitude of 900kg/m³.

The accretion rate varies with wind speed, air temperature and rate of precipitation and is most often formed at temperatures between 0°C and -10°C.

2.7.3. Wet snow

Wet snow is the accretion process where snowflakes partly contain liquid water and therefore are able to adhere to a surface. This implies that wet snow accretion occurs at temperatures just above freezing point. If a temperature decrease follows the wet snow

accretion process, the snow will freeze, causing a change in density and adhesive strength. Other factors that influence these parameters are wind speed and fraction of liquid water in the snow.

2.7.4. Hoar frost

Hoar frost is formed by sublimation of water vapor and is common at lower temperatures. Frost is the coating or deposit of ice that may form in humid air in cold conditions, usually overnight. In temperate climates it most commonly appears as fragile white crystals or frozen dew drops near the ground, but in cold climates it occurs in a greater variety of forms. Frost is composed of delicate branched patterns of ice crystals formed as the result of fractal process development. However, hoar frost is of low density and strength and does therefore not result in significant ice loads on structures.

3. CFD analysis of the 2D simulations

Models of the sensor cover are designed to have at least 0.12 x 0.05 x 0.02 m free space in them to fit the sensor module. In this chapter only 2D calculations will be considered so only 2 dimensions of the sensor module are needed: 0.12 m as length and 0.02 as height.

All of the airflows will be computed for air temperature equal 20⁰C. That means the density of the air is equal 1.2044 kg/m³ and dynamic viscosity is equal 1.81*10⁻⁵ Pa*s.

3.1. Mesh generation

COMSOL is using unstructured meshes. Examples how they are for calculations is given in the figures below where bottom edge is wall which requires different meshes for different flow models. Laminar flow does not need fine mesh while k epsilon and k omega SST need mesh which satisfy the wall function conditions for y⁺. Figure 3.1 shows examples of used meshes.

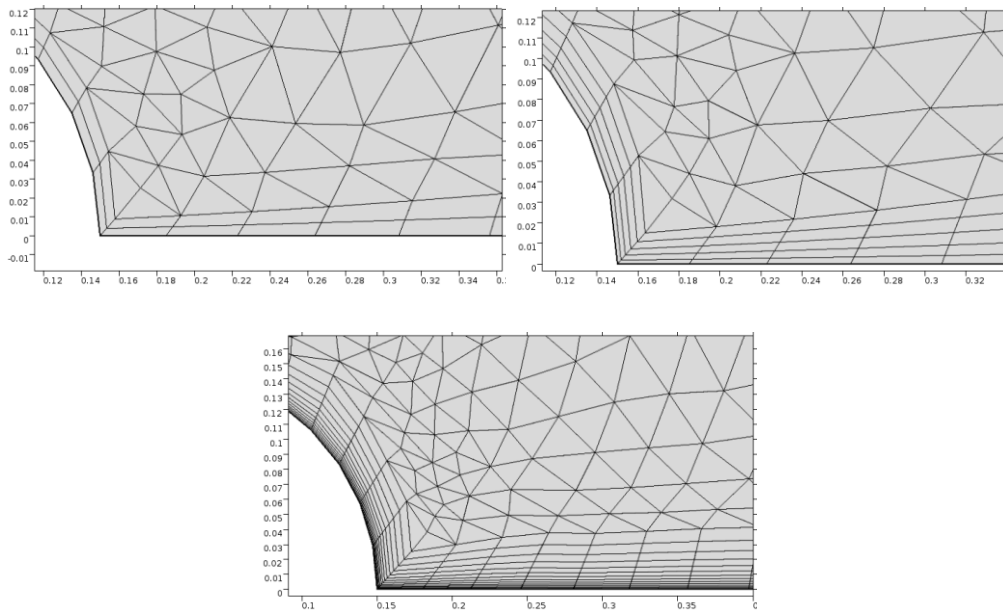


Figure 3.1 Mesh structure for COMSOL on the upper left for laminar flow, upper right: k epsilon and below k omega SST

3.2. Flow over a cylinder

In COMSOL a test case was prepared and executed – flow around a cylinder. It was done to check if both programs are able to give similar results and adequate setting was used. There is for this case experimental data as well to validate this results.

This model was chosen mostly because it has a very simple geometry and is commonly used to help students understand fluid dynamics.

3.2.1. Geometry of the domain and boundary conditions

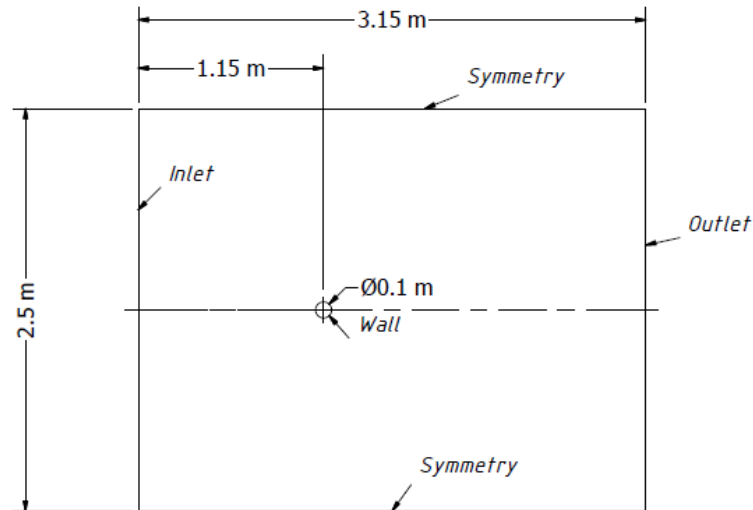


Figure 3.2 Geometry of the flow around a cylinder and boundary conditions

Figure 3.2 shows geometry of the model used in turbulent flow. In the laminar flow case whole model was rescaled with ratio 5:1. Cylinder has a diameter equal 0.02 m, the domain has 0.5 m height and 0.63 m length. The cylinder distance to the inlet boundary condition is 0.23 m instead.

3.2.2. Verification and validation of the laminar flow

It was computed for small Reynolds number ($Re=200$) thus small velocity of the air ($u=0.15$ [m/s]).

Laminar flow is not reliable for computing open flows because it needs very small velocity of the fluid but still there is a chance it may occur. This flow has a lot differences with turbulent flow for example layers cannot mix, is stationary etc. This flow is very easy to compute and does not require a very fine mesh. Thanks to this feature we can easily initially analyze size of the control volume and influence of the mesh structure and size because computing time is very short.

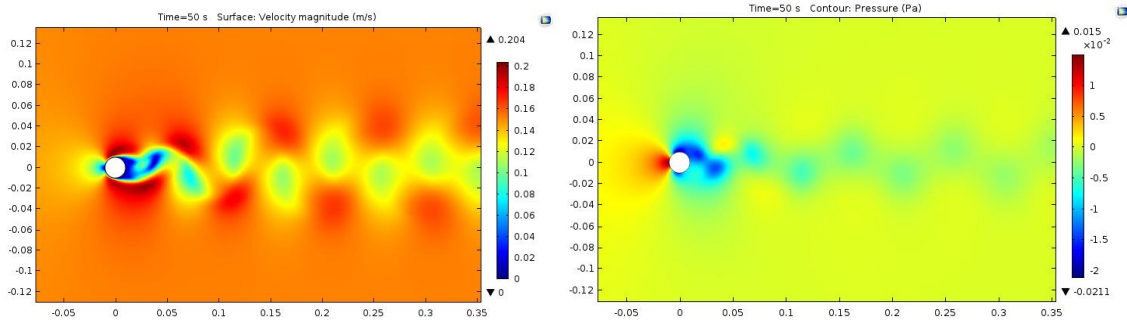


Figure 3.3 Velocity, on the left, and pressure, on the right, field of the laminar flow over a cylinder



Figure 3.4 Karman vortex sheet behind the cylinder for $Re=200$. Photograph by Gary Koopman [4]

On the pressure and velocity fields, presented on the Figure 3.3, there is a visible vorticity even though it is for a very small Reynolds number and diameter of cylinder. There is large vortex sheet behind the cylinder. The flow looks very similar to the photograph, Figure 3.4 – the vortices are created approximately in the same places which can be easily observed on the velocity graphs, vortices are in the area of low velocity.

Graphs for drag or lift coefficients are needed because these coefficients are changing through time due to vortex shedding. Strouhal number St is equal 0.19 for $Re = 200$ from Figure 3.5 from that frequency of vortex shedding $f_{vs} = 1.425$ Hz which means the new vortices will be created in the 0.702 second period after the flow develops.

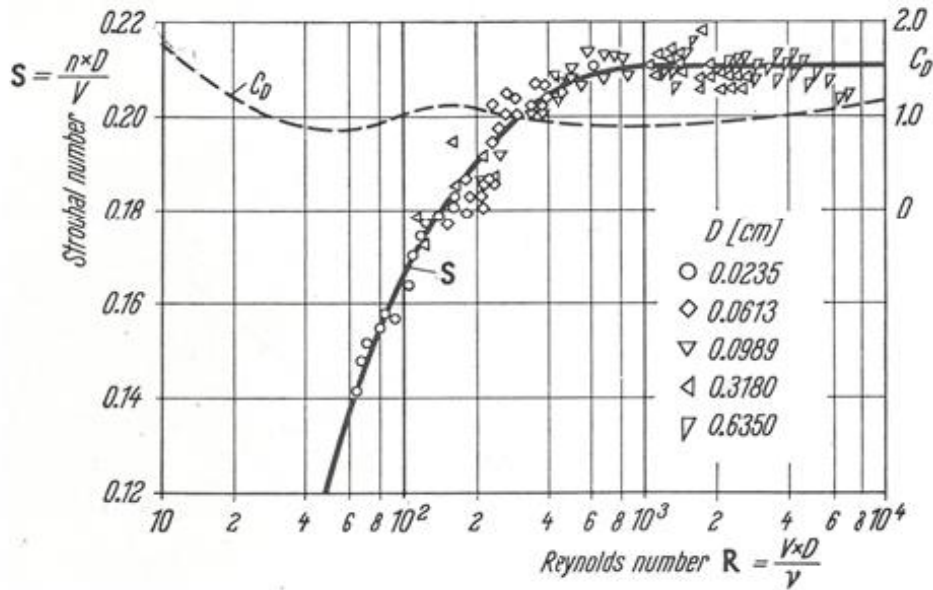


Figure 3.5 Plot of Strouhal number to the Reynolds number for cylinders with different diameter

Both coefficients were calculated for reference length equal diameter of the cylinder $L = 0.02$ m. Number of degrees of freedom 23754. Figure 3.6 shows lift and drag coefficient changing though time.

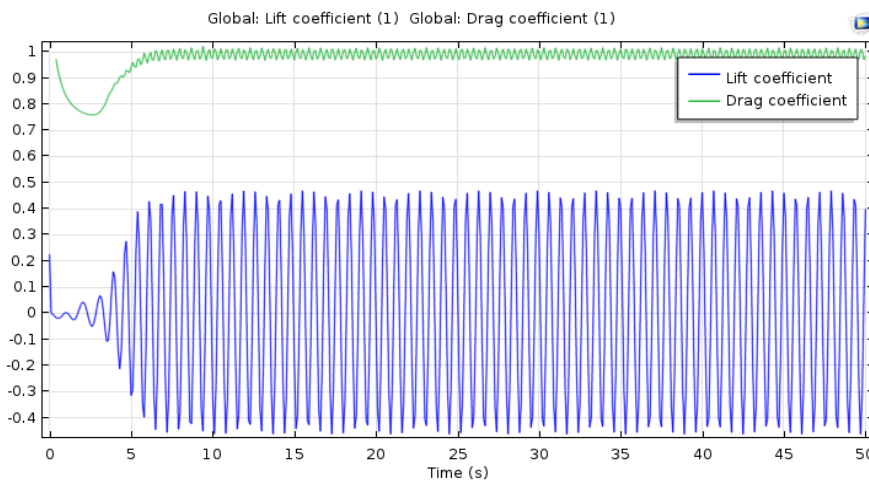


Figure 3.6 Drag and lift coefficients for laminar flow over a cylinder

$$\begin{array}{lll} \text{mean } C_d = 0.9925 & B_{cd} = 0.0225 & f_{cd} = 2.8 \text{ Hz} \\ \text{mean } C_l = 0 & B_{cl} = 0.4666 & f_{cl} = 1.4 \text{ Hz} \end{array}$$

where

B_{cd} , B_{cl} is amplitude of the oscillations of the drag and lift coefficient
 f_{cd} , f_{cl} is frequency of the oscillations of the drag and lift coefficient

Lift coefficient should be more symmetrical for this flow. This error is due to too high tolerance (10^{-5}) for the dependent variables such as pressure and velocity of the fluid.

To save computational time this case will not be recomputed because after comparing results with the experiment data, they are quite reasonable.

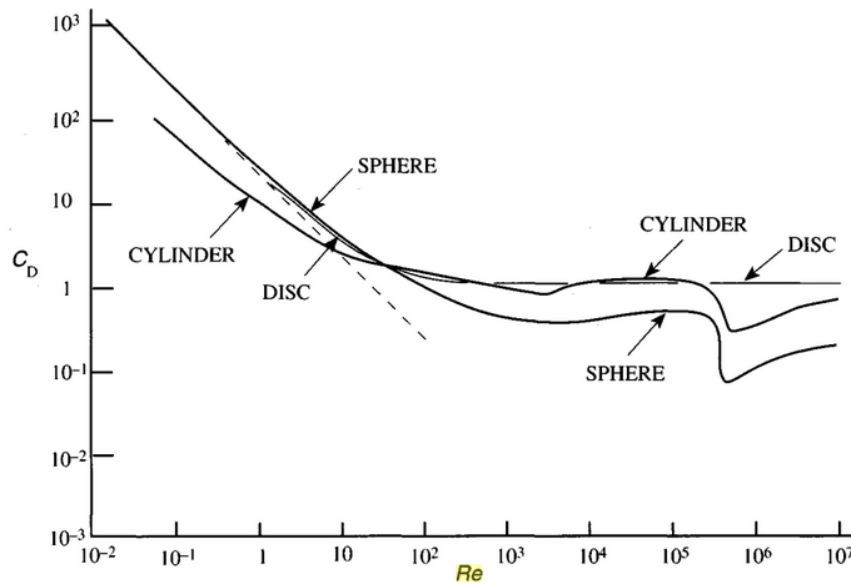


Figure 3.7 Log-log plot of drag coefficient C_D as a function of Reynolds number Re for spheres, transverse cylinders and face-on discs. The broken straight line represents Stoke's law

From figure 3.7 drag coefficient for this flow should be 1.01. Errors in our calculations are for COMSOL $(1.05-0.9925)/1.05*100\% = 5.47\%$.

Frequency of the oscillations of the drag coefficient is two times bigger than for the lift coefficient. This is happening due to the vorticity of the fluid this feature can be seen on the figure 3.8 below. For drag coefficient it does not matter on which side of the cylinder the vortices are developing, they both affect this coefficient in the same way by creating horizontal force acting in the opposite direction to the flow. Where the vortexes develop is important for lift coefficient because of the vertical force these vortexes are creating which has normal direction to the surface of the cylinder. The frequency of the oscillations for the lift coefficient should be the same as the frequency of the origin of the vortexes calculated using Strouhal number $f_{cl}/f_{vs} = 0.98$. The difference is very small approximately 2%.

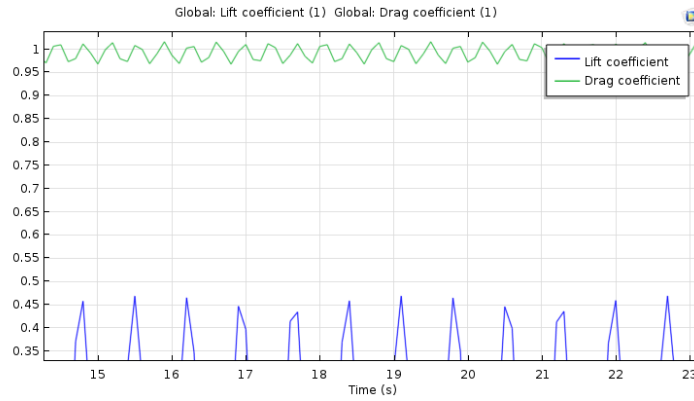


Figure 3.8 Oscillations of the drag and lift coefficients for the laminar flow over a cylinder on the left

To verify the size of control volume its parameters were changed to see if they are able to affect the results. Changes in the values of coefficients are small, around 1%. The mesh independency test was performed as well. Results from both tests are given in Tables 3.1-3.2.

Table 3.1 Control volume test for laminar flow over a cylinder test case

	mean C_d	max C_l
reducing the distance from inlet to cylinder for 0.1 m	1.056	0.4783
reducing the distance from outlet to cylinder for 0.1 m	1.074	0.4821
reducing the distance from both symmetry planes to cylinder for 0.1 m	0.9821	0.4538

Table 3.2 Mesh independency test for laminar flow over a cylinder test case

Number of degrees of freedom	mean C_d	max C_l
9734	1.2432	0.7422
15383	0.1033	0.4731
23754	0.9925	0.4666
30742	0.9866	0.4532

3.2.3. Verification and validation of the turbulent flow

Turbulent flow is commonly used for computation airflows. It is very rare to see different models of the open airflows. Turbulence is very intensive flow where layers can mix. It was computed for high Reynolds number ($Re=10000$) and velocity of the air equals $u=1.5$ m/s.

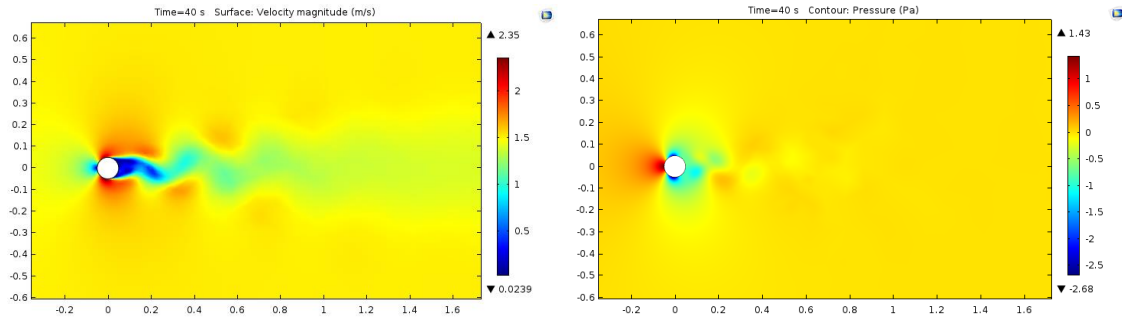


Figure 3.9 Velocity, on the left and pressure, in the right, field of the k epsilon turbulence model of the flow over a cylinder

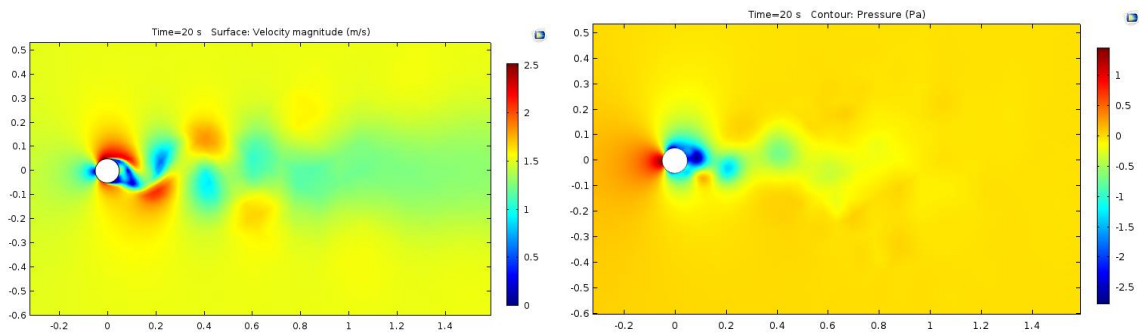


Figure 3.10 Velocity, on the left and pressure, in the right, field of the k omega SST turbulence model of the flow over a cylinder

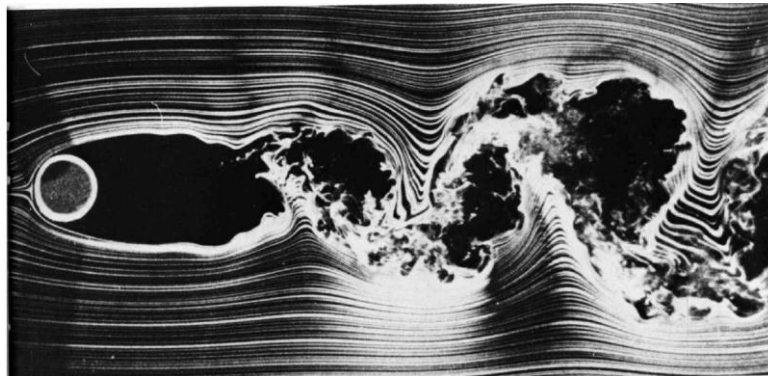


Figure 3.11 Flow past a cylinder for $Re=10000$. Photograph made by Thomas Corke and Hassan Nagib [4]

Comparing velocity and pressure fields from Figures 3.9-3.10 computed using both turbulence models to the photograph, Figure 3.11, it is clear that k omega SST is more accurate and simulates wake area better than k epsilon. Vortexes are almost not visible on the velocity graph for k epsilon.

Both coefficients were calculated for reference length equal diameter of the cylinder $L=0.1$ m. As the vorticity highly affect the coefficients, creating oscillations through time they will be plotted.

COMSOL solves 18410 number of degrees of freedom while using k epsilon model and 23788 while using k omega SST model. Figure 3.12 shows coefficients for both turbulence models.

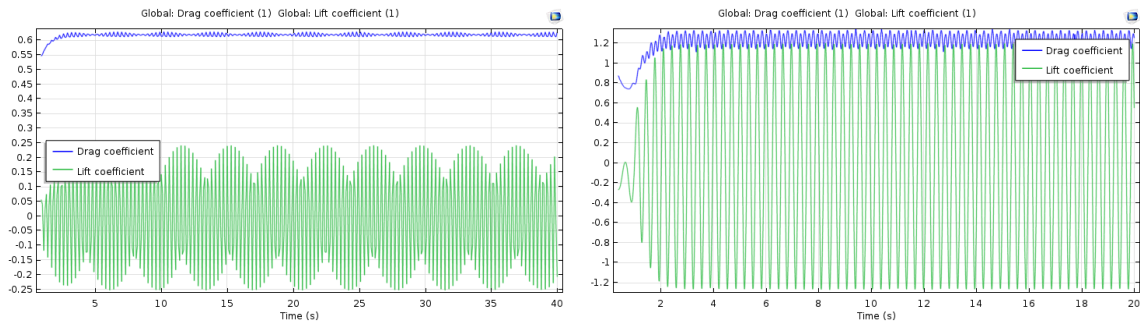


Figure 3.12 Drag and lift coefficient for turbulent flow over a cylinder using k epsilon turbulence model (on the left) and k omega SST turbulence model (on the right)

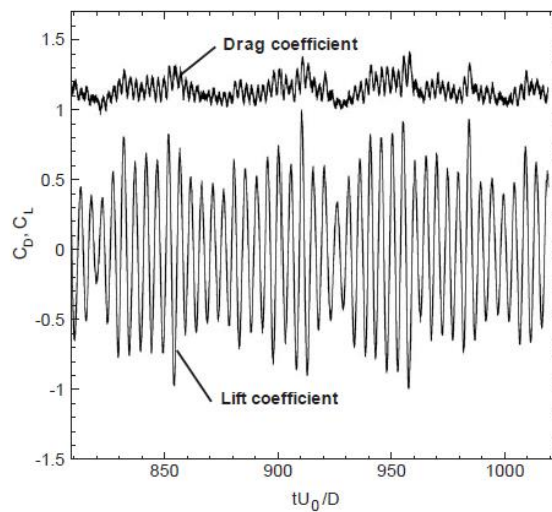


Figure 3.13 Time history of drag and lift coefficient for the flow past stationary cylinder at $Re = 10000$. Simulation done using DNS [6]

Coefficient for k epsilon model

$$\text{mean } C_d = 0.621 \quad B_{cd} = 0.008 \quad f_{cd} = 4.5 \text{ Hz}$$

$$\text{mean } C_l = 0 \quad B_{cl} = 0.24 \quad f_{cl} = 4\text{Hz}$$

Coefficients for k omega SST model

$$\text{mean } C_d = 1.24 \quad *B_{cd} = 0.08 \quad f_{cd} = 1.53 \text{ Hz}$$

$$\text{mean } C_l = 0 \quad B_{cl} = 1.19 \quad f_{cl} = 3.08 \text{ Hz}$$

Strouhal number is equal $St = 0.2$ (form [6]) that means frequency of vortex sheet should be equal $f_{vs} = 3$ Hz so is the frequency of oscillations of the lift coefficient. The frequency of oscillations for k epsilon model is clearly wrong. Figure 3.14 shows more clearly this oscillations.

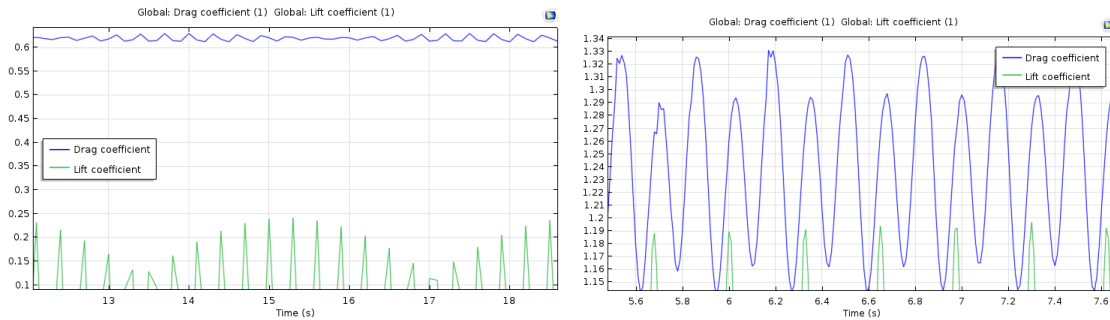


Figure 3.14 Oscillations of drag and lift coefficient for turbulent flow over a cylinder using k epsilon turbulence model (on the left) and k omega SST model (on the right)

On the Figure 3.12 drag and lift coefficient have wrong values. Drag coefficient from experiment is $C_d = 1.15$ by data provided by [6] and presented on the Figure 3.13. The error in calculating drag for k epsilon model is very high $(1.15-0.621)/1.15*100\% = 46\%$ while the same error is much smaller for k omega SST $(1.15 - 1.24)/1.15*100\% = -7.8\%$ where sign minus means only that the value is too high instead of small. Oscillations of the drag and lift coefficient are not logical for k epsilon. It should be that drag have frequency two times lower than the lift which is fulfilled for k omega SST turbulence model. Coefficient graph generated from k omega SST is much more similar than one from k epsilon to DNS calculations which is simulating turbulent flow for almost all turbulence spectrum all way to the wall and is known as the most accurate CFD tool.

In turbulent flows y^+ value is very important for the walls. From COMSOL in this case y^+ is equal approximately 11.1 for all walls which is very close to the 11.63 value that means this condition as fulfilled for k epsilon and for k omega SST maximum y^+ is equal 1.6 which is below 2. Figure 3.15 shows y^+ values for both turbulence models.

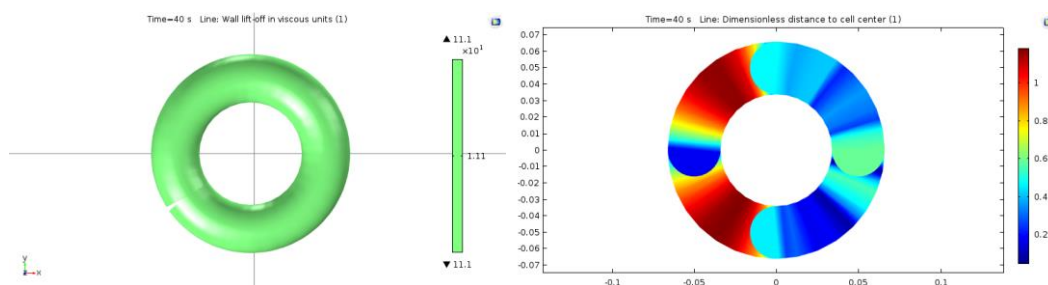


Figure 3.15 Turbulent k epsilon and k omega SST models for flow over a cylinder – y^+ value

To verify the size of control volume its parameters will be changed to see if these changes were able to affect the results and conditions for using turbulence models. The mesh independency test will be done as well by changing meshes. Each of these test was done for turbulence models and additionally the y^+ value was checked with constant first layer thickness l_t . Change in coefficients are very small, around 1% near the used control volume and mesh. Results are given in Tables 3.3-3.4.

Table 3.3 Control volume test for turbulent flow over a cylinder test case

	mean Cd [1]	max Cl [1]	l_t [mm]	max y^+ [1]
k epsilon				
reducing the distance from inlet to cylinder for 0.1 m	0.6176	0.2354	0.0024	11.126
reducing the distance from outlet to cylinder for 0.1 m	0.6358	0.2586	0.0024	11.145
reducing the distance from both symmetry planes to cylinder for 0.1 m	0.6278	0.2438	0.0024	11.121
k omega SST				
reducing the distance from inlet to cylinder for 0.1 m	1.2475	1.1846	0.0001	1.58
reducing the distance from outlet to cylinder for 0.1 m	1.2385	1.1937	0.0001	1.62
reducing the distance from both symmetry planes to cylinder for 0.1 m	1.2558	1.169	0.0001	1.61

Table 3.4 Mesh independency test for turbulent flow over a cylinder test case

Number of degrees of freedom	mean Cd [1]	max Cl [1]	l_t [mm]	max y^+ [1]
k epsilon				
9543	0.843	0.486	0.0024	12.484
15324	0.643	0.255	0.0024	11.156
18410	0.621	0.24	0.0024	11.1
26832	0.614	0.235	0.0024	11.05
k omega SST				
13954	1.493	1.39	0.0001	1.89
18394	1.252	1.23	0.0001	1.72
23788	1.24	1.19	0.0001	1.6
35382	1.232	1.184	0.0001	1.58

3.3. Flow over a cylindrical sensor mounted on flat surface

This is a test case for sensor mounted on a flat surface. Cylindrical shape was chosen because of simple shape and for typical cubic shape drag and lift forces will be high with large wake behind the body which is undesirable.

3.3.1. Geometry of the domain and boundary conditions

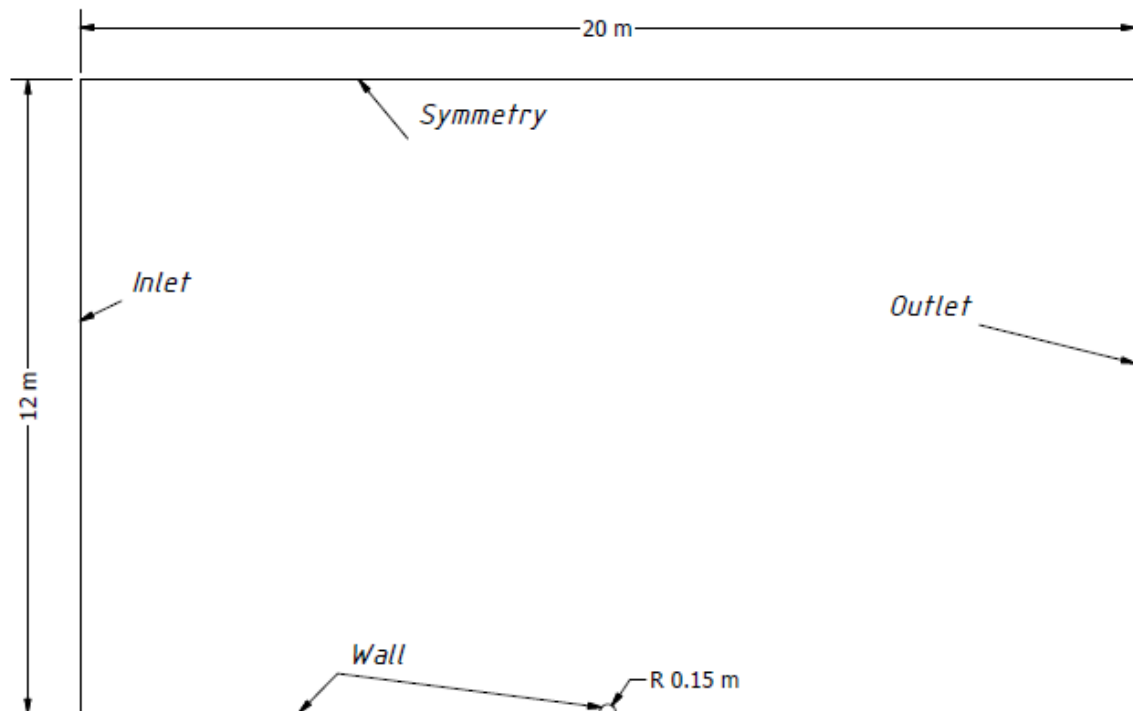


Figure 3.16 Geometry of the domain and boundary conditions for flow over a cylindrical sensor mounted on flat surface

The domain have a shape of a rectangular with height 12 m and width 20 m. A sensor with a half cylinder shape with diameter 0.3 m is placed in the middle of the down edge. For the boundary conditions: on the right edge there is inlet, left is outlet, top is symmetry and the bottom with sensor is wall. Figure 3.16 shows this geometry.

3.3.2. Verification and validation of laminar flow

Laminar flow will be computed for fluid with density 1 kg/m^3 and dynamic viscosity $0.01 \text{ Pa}\cdot\text{s}$. Reason for this assumption is that for air which has very small dynamic viscosity $1.81 \cdot 10^{-5} \text{ Pa}\cdot\text{s}$ to have small Re around 500 the velocity of the fluid would be equal $3.76 \cdot 10^{-4} \text{ m/s}$ with characteristic length 20 m in horizontal direction. This small velocity would force programs to compute for very long time and the forces would be very small

which may cause problems with accuracy of this calculations. New fluid has $Re = 500$ with $L = 20$ m with velocity of the fluid equal $u = 0.25$ m/s which is much higher than for air.

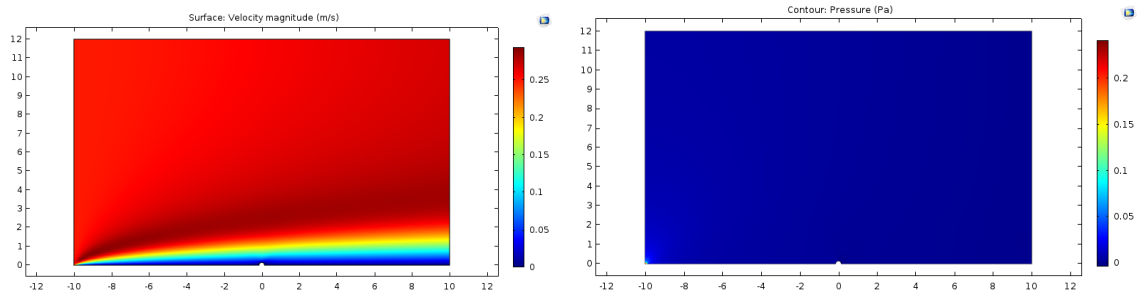


Figure 3.17 Velocity, on the left, and pressure, on the right, field of the laminar flow over a cylindrical sensor mounted on flat surface

On the Figure 3.17 pressure and velocity fields are shown. This flow is interrupted by the wall very close to inlet. There is a large wake generated by the wall not the sensor. Here there are not any vortexes in this flow. Pressure field is almost constant in whole domain. Only difference is on short part of the wall near inlet where maximum pressure is.

Both coefficients were calculated for reference length equal external perimeter of the sensors cover $L = 0.471$ m.

- Number of degrees of freedom 10827.
- $C_d = 0.075375$
- $C_l = -0.010494$

To verify the size of the control volume and mesh independency similar as before tests were performed. Results obtained from these test are sufficient, error is equal approximately 1% of the coefficients value for used setup. Tables 3.5-3.6 present the results.

Table 3.5 Control volume test for laminar flow a cylindrical sensor mounted on flat surface.

	C_d [1]	C_l [1]
reducing the distance from inlet to sensor for 0.1 m	0.08372	-0.01538
reducing the distance from outlet to sensor for 0.1 m	0.8462	-0.01824
reducing the distance from upper wall to the sensor for 0.1 m	0.0812	-0.01327

Table 3.6 Mesh independency test for laminar flow over a cylindrical sensor mounted on flat surface

Number of degrees of freedom	C_d [1]	C_l [1]
5823	0.23843	-0.2245
8392	0.09437	-0.01832
10827	0.075375	-0.010494
15832	0.06937	-0.009837

3.3.3. Verification and validation of turbulent flow

Turbulence needs as high Re as possible so air can be used as the fluid in the domain. Velocity of the airflow is assumed to be $u = 1$ m/s. For this case $Re = 1333333$ for length of the bottom wall $L = 20$ m and $Re = 10000$ for highest vertical length $L = 0.15$ m. Computation of turbulence will be done with k epsilon and k omega SST turbulence models.

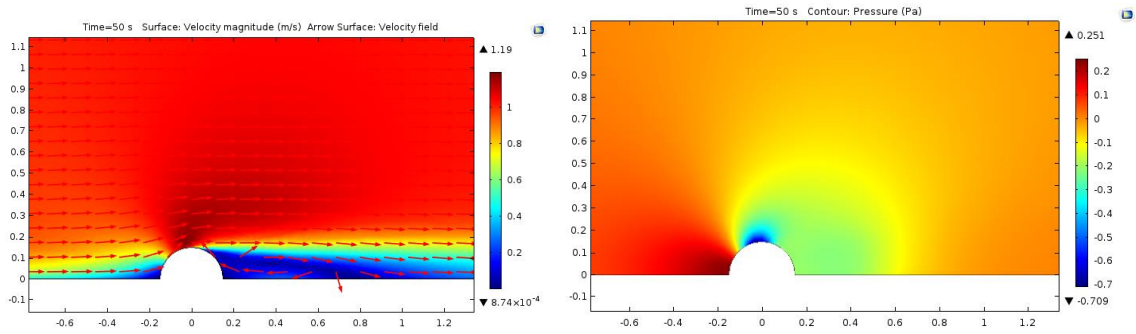


Figure 3.18 Velocity with velocity indicators, on the left, and pressure, on the right, field of the k epsilon turbulent flow over a cylindrical sensor mounted on flat surface

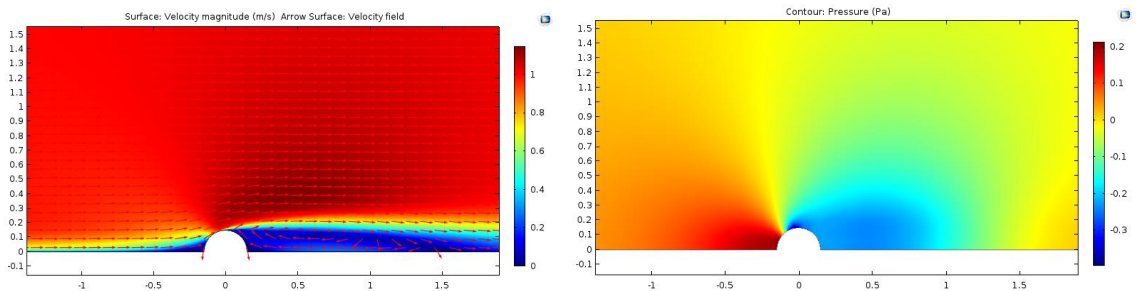


Figure 3.19 Velocity with velocity indicators, on the left, and pressure, on the right, field of the k omega SST turbulent flow over a cylindrical sensor mounted on flat surface

Comparing both methods, presented on Figures 3.18-3.19, there are some differences. Most of them are in the wake where for k omega SST model vortex behind the sensor is larger (almost two times) and pressure is lower in the wake area than for k epsilon.

Both force coefficients were calculated for reference length equal external perimeter of the sensor, $L = 0.471$ m.

Results for the coefficients given by using k epsilon turbulence model:

- number of degrees of freedom is 54095

$$C_d = 0.11867$$

$$C_l = 0.36001$$

Results for the coefficients given by using k omega SST turbulence model:

- number of degrees of freedom is 64095

$$C_d = 0.16466$$

$$C_l = 0.21291$$

Conditions for y^+ for both turbulence models were fulfilled. In COMSOL k epsilon has y^+ equal 11.1 which is close to 11.06 and for k omega SST maximum $y^+ = 2.1$ and is close enough for this condition, area with higher than 2 y^+ value is near inlet and it should affect the results. Figure 3.20 shows y^+ values for both coefficients.

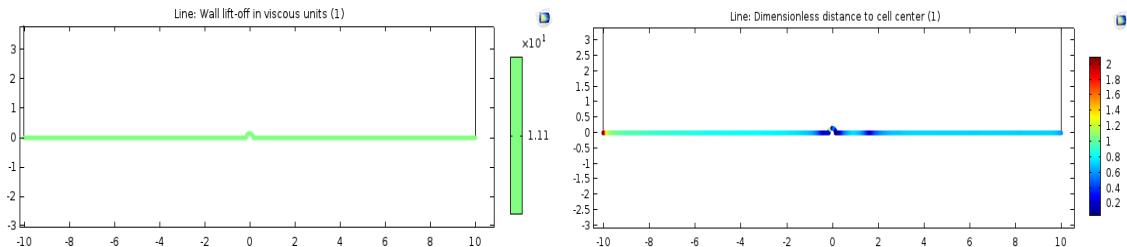


Figure 3.20 Turbulent k epsilon and k omega SST models for flow over a cylindrical sensor mounted on flat surface – y^+ value

To verify the size of the control volume and the mesh independency just as before tests were executed for turbulence. Change in coefficients are very small, around 1% near the used control volume and mesh. Results are given in the Tables 3.7-3.8.

Table 3.7 Control volume test for turbulent flow over a cylindrical sensor mounted on flat surface

	Cd [1]	Cl [1]	l _t [mm]	max y ⁺ [1]
k epsilon				
reducing the distance from inlet to sensor for 0.1 m	0.12234	0.37392	0.0024	11.33
reducing the distance from outlet to sensor for 0.1 m	0.10283	0.35859	0.0024	11.93
reducing the distance from upper wall to the sensor for 0.1 m	0.11729	0.36142	0.0024	11.36
k omega SST				
reducing the distance from inlet to sensor for 0.1 m	0.17034	0.22943	0.0001	2.249
reducing the distance from outlet to sensor for 0.1 m	0.17048	0.22401	0.0001	2.139
reducing the distance from upper wall to the sensor for 0.1 m	0.16932	0.21949	0.0001	2.012

Table 3.8 Mesh independency test for turbulent flow over a cylindrical sensor mounted on flat surface

Number of degrees of freedom	Cd [1]	Cl [1]	l _t [mm]	max y ⁺ [1]
k epsilon				
29058	0.28534	0.53848	0.0024	12.932
45392	0.12948	0.38472	0.0024	11.494
54095	0.11867	0.36001	0.0024	11.102
73948	0.11574	0.35947	0.0024	11.08
k omega SST				
30748	0.28477	0.29474	0.0001	2.194
45084	0.17944	0.22849	0.0001	2.149
64095	0.16466	0.21291	0.0001	2.103
83945	0.15947	0.20947	0.0001	2.08

3.4. Flow over a cylindrical sensor mounted on a flat surface with elevation

Flow over a sensor mounted on a blade of wind turbine will be affected by geometry of the front part of the blade. This test case is a sensor mounted on elevated surface with round front which can imitate blade in the neutral position.

3.4.1. Geometry and boundary conditions

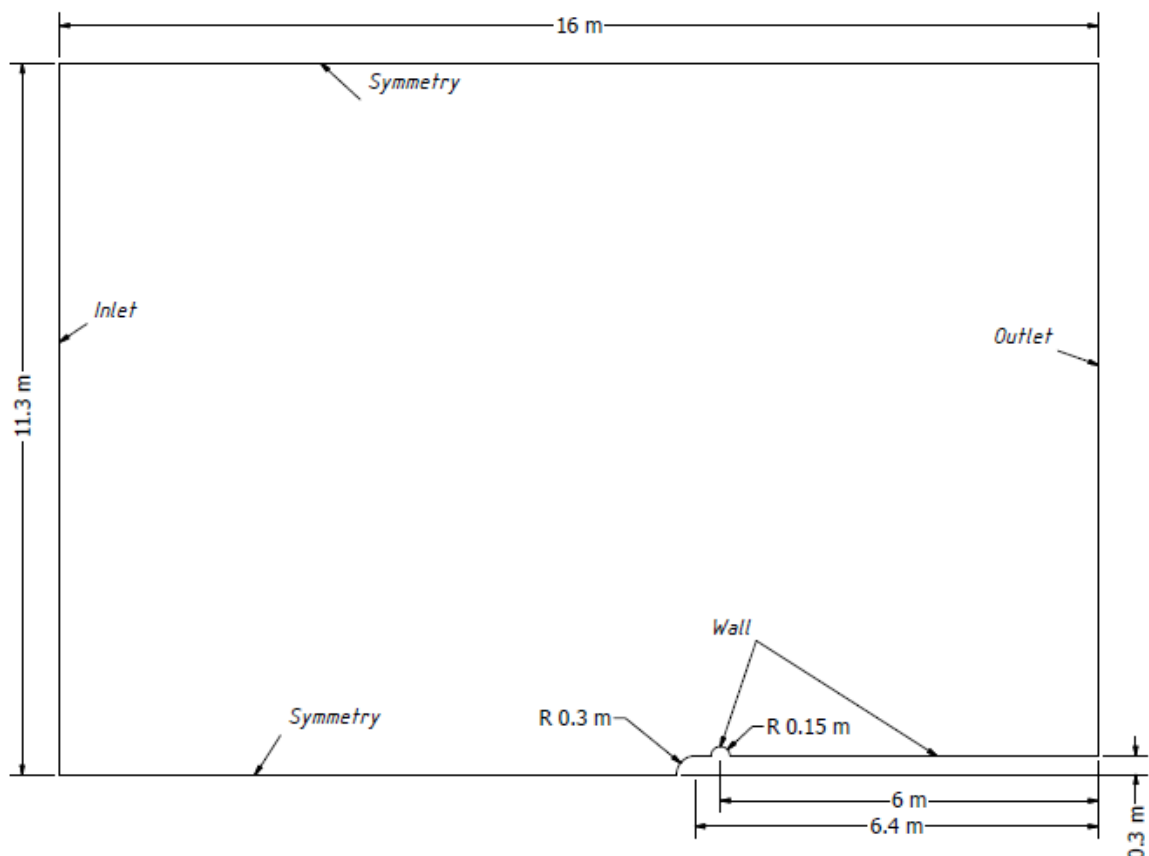


Figure 3.21 Geometry of the domain and boundary conditions for flow over a cylindrical sensor mounted on a flat surface with elevation

Sensor has the same geometry as previous model – half of cylinder in this case mounted on a flat surface with elevation. Figure 3.21 shows geometry of this model.

3.4.2. Verification and validation of laminar flow

Laminar flow will be computed for fluid with density 1 kg/m^3 and dynamic viscosity $0.01 \text{ Pa}\cdot\text{s}$ for the same reasons as in the previous model. To have $Re = 500$ with $L = 6.7 \text{ m}$ new fluid needs $u = 0.75 \text{ m/s}$.

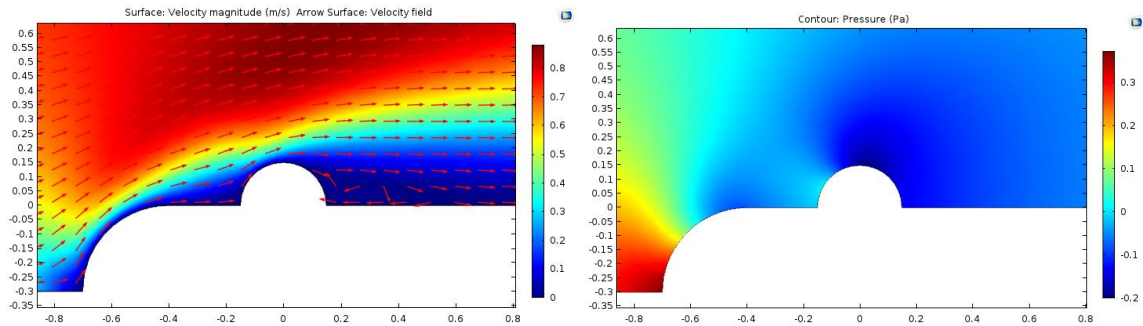


Figure 3.22 Velocity with velocity indicators and pressure field of the laminar flow over a cylindrical sensor mounted on a flat surface with elevation

A large wake is generated by surface of the elevation and the sensor. There is a small vortex behind the sensor but none before. Pressure after the flow encountered the sensor is very small and even on the sensor there is underpressure area. This is presented on the Figure 3.22.

Both coefficients were calculated for reference length equal external perimeter of the sensors cover $L = 0.471$ m.

- Number of degrees of freedom 8325.

$$C_d = 0.13818$$

$$C_l = 0.2963$$

To verify the size of the control volume and mesh independency similar as before tests were performed. Results obtained from these test are sufficient, error is equal approximately 1% of the coefficients value for used setup. Results are given in the Tables 3.9-3.10.

Table 3.9 Control volume test for laminar flow a cylindrical sensor mounted on flat surface with elevation

	C_d [1]	C_l [1]
reducing the distance from inlet to sensor for 0.1 m	0.14203	0.3019
reducing the distance from outlet to sensor for 0.1 m	0.14	0.302
reducing the distance from upper wall to the sensor for 0.1 m	0.14102	0.3069

Table 3.10 Mesh independency test for laminar flow over a cylindrical sensor mounted on flat surface with elevation

Number of degrees of freedom	C_d [1]	C_l [1]
5943	0.22489	0.4847
6593	0.14877	0.3048
8325	0.13818	0.2963
11948	0.13047	0.2896

3.4.3. Verification and validation of turbulent flow

In this case air can be the fluid in the domain. It can be assumed that velocity of the airflow $u = 1 \text{ m/s}$ which give us $Re = 446667$ for the highest dimension in the horizontal direction $L = 6.7 \text{ m}$ and $Re = 30000$ for the highest dimension in the vertical direction $L = 0.45 \text{ m}$.

Both Reynolds number are much higher than critical Reynolds number, $Re=2300$, which means flow should be turbulent. Computation of turbulence will be done with k epsilon and k omega SST turbulence models.

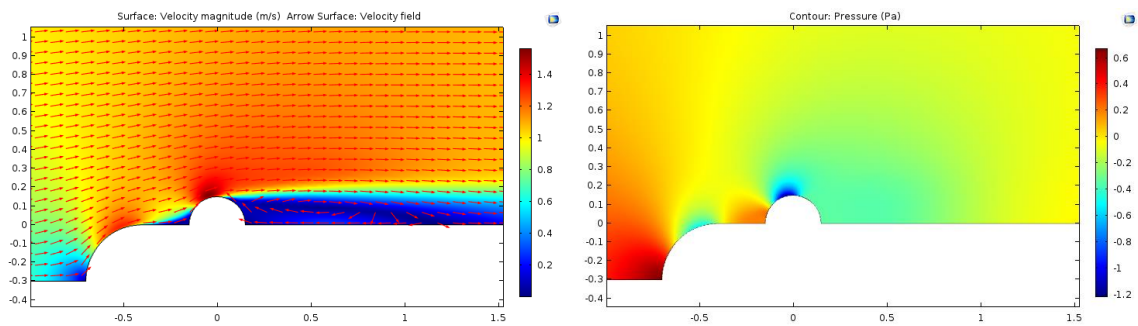


Figure 3.23 Velocity with velocity indicators and pressure field of the turbulent k epsilon flow over a cylindrical sensor mounted on a flat surface with elevation

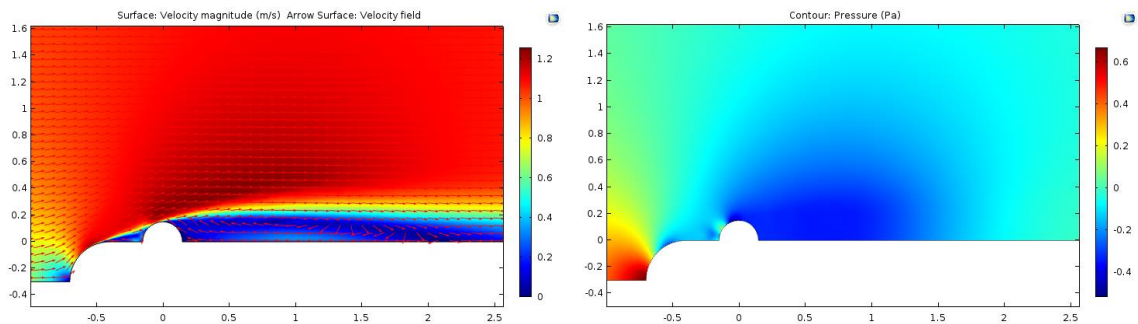


Figure 3.24 Velocity with velocity indicators and pressure field of the turbulent k omega SST flow over a cylindrical sensor mounted on a flat surface with elevation

The same problem occurred as in the test case without elevation while comparing pressure and velocity graphs for both methods of solving turbulence. Model k omega SST has a larger wake and a vortex behind the sensor and in addition pressure is lower in the wake area than for the k epsilon. Before the sensor there is a small vortex of equal size in both turbulence models. This is presented on the Figures 3.23-3.24.

Both force coefficients were calculated for reference length equal external perimeter of the sensor, $L = 0.471 \text{ m}$.

Results for the coefficients given by using k epsilon turbulence model:

- number of degrees of freedom is 50980
- $C_d = 0.093445$
 $C_l = 0.63305$

Results for the coefficients given by using k omega SST turbulence model:

- number of degrees of freedom is 59300
- $C_d = 0.11903$
 $C_l = 0.31813$

The lift coefficient calculated when using k epsilon is two times bigger than the lift coefficient from k omega SST. Reason for this is in the simulation of the wake area where there are vortexes influencing the coefficients.

Conditions for y^+ for both turbulence models were fulfilled. In COMSOL k epsilon has y^+ equal 11.1 which is close to 11.06 and for k omega SST maximum $y^+ = 1.42$. In OpenFOAM k epsilon has minimum $y^+ = 44.8091$ and maximum $y^+ = 164.443$ while for k omega SST maximum $y^+ = 1.92772$. Figure 3.25 shows y^+ values.

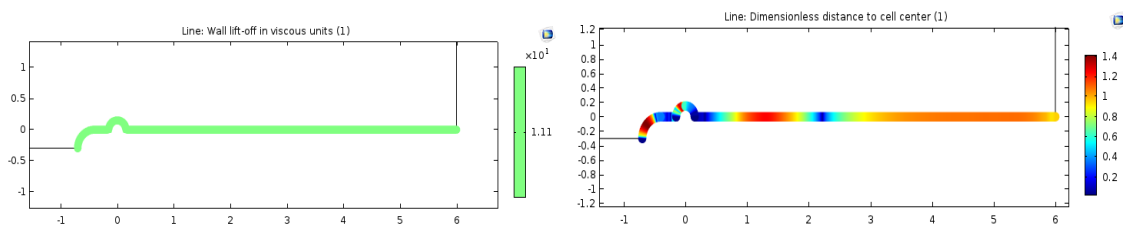


Figure 3.25 Turbulent k epsilon and k omega SST models for flow over a cylindrical sensor mounted on flat surface – y^+ value

To verify the size of the control volume and the mesh independency just as before tests were executed for turbulence. Change in coefficients are very small, around 1% near the used control volume and mesh. Results are given in the Tables 3.11-3.12.

Table 3.11 Control volume test for turbulent flow over a cylindrical sensor mounted on flat surface with elevation

	Cd [1]	Cl [1]	lt [mm]	max y ⁺ [1]
k epsilon				
reducing the distance from inlet to sensor for 0.1 m	0.10973	0.64947	0.0024	11.927
reducing the distance from outlet to sensor for 0.1 m	0.11937	0.63938	0.0024	11.582
reducing the distance from upper wall to the sensor for 0.1 m	0.99337	0.64247	0.0024	11.399
k omega SST				
reducing the distance from inlet to sensor for 0.1 m	0.12289	0.32947	0.0001	1.54
reducing the distance from outlet to sensor for 0.1 m	0.12394	0.31937	0.0001	1.49
reducing the distance from upper wall to the sensor for 0.1 m	0.11941	0.31738	0.0001	1.51

Table 3.12 Mesh independency test for turbulent flow over a cylindrical sensor mounted on flat surface with elevation

Number of degrees of freedom	Cd [1]	Cl [1]	lt [mm]	max y ⁺ [1]
k epsilon				
30837	0.13584	0.76342	0.0024	12.004
41848	0.10474	0.65847	0.0024	11.248
50980	0.09345	0.63305	0.0024	11.101
63038	0.08936	0.62936	0.0024	11.03
k omega SST				
39472	0.13948	0.38382	0.0001	1.69
49747	0.12483	0.32474	0.0001	1.5
59300	0.11903	0.31813	0.0001	1.42
73884	0.11683	0.31284	0.0001	1.4

3.5. Analysis of the designed sensors

From analysis performed before, the best way to simulate the turbulent flow is by using the k omega SST turbulence model which is more accurate and creates better simulations of the flow especially the wake area than k epsilon turbulence model, so calculations will be done only by using k omega SST turbulence model. The geometry of the domain was chosen as for the sensor mounted on the elevated surface where lift coefficient is changed due to the elevation like in the real case of flow over a blade of a wind turbine in the neutral horizontal position. From this it can be assumed that this case was actually stationary – it was not dependent on time because in the flow there were not any time depending variables, for example inlet velocity is changing through time or some time dependent dynamic in the model such as von Karman vortex sheet. Validation and verification for researched shapes of the sensor will not be described for this part because it is the same as for the tests described in analysis chapter. Only mesh will be adjusted to satisfy $y^+ \leq 2$ condition.

Laminar flow will not be computed for upcoming models because it is not reliable for this project due to very small requirement of the air velocity which should not occur in real life.

Simulations were done for 1 m/s air velocity and for 20⁰C air temperature. This flow is turbulent as the Reynolds number is equal $Re = 446667$ for characteristic length in horizontal direction $L = 6.7$ m . In vertical direction $Re = 23333$ for $L = 0.35$ m for first sensor,

$Re = 22667$ for $L = 0.34$ m for second sensor and $Re = 23533$ for $L=0.353$ for third.

Geometry of the domain is the same as for the flow over a cylindrical sensor mounted on a flat surface with elevation in the analysis chapter. Boundary conditions are the same as well.

First sensor has a very simple geometry. Main reason for designing this shape was to build a slope into the direction of the flow to reduce the influence of the drag force and a slope behind the sensor to prevent developing of the vortices by simply reducing their area of their action. Second model has smooth edges. Main goal was to reduce drag and lift even more by giving this cover more aerodynamical shape. Third model is a variation to check if bigger slope with much lower angle of inclination in the front will be able to

reduce drag coefficient. It has smooth edges as the second sensor. All proposed geometries of the sensor are presented on the Figure 3.26.

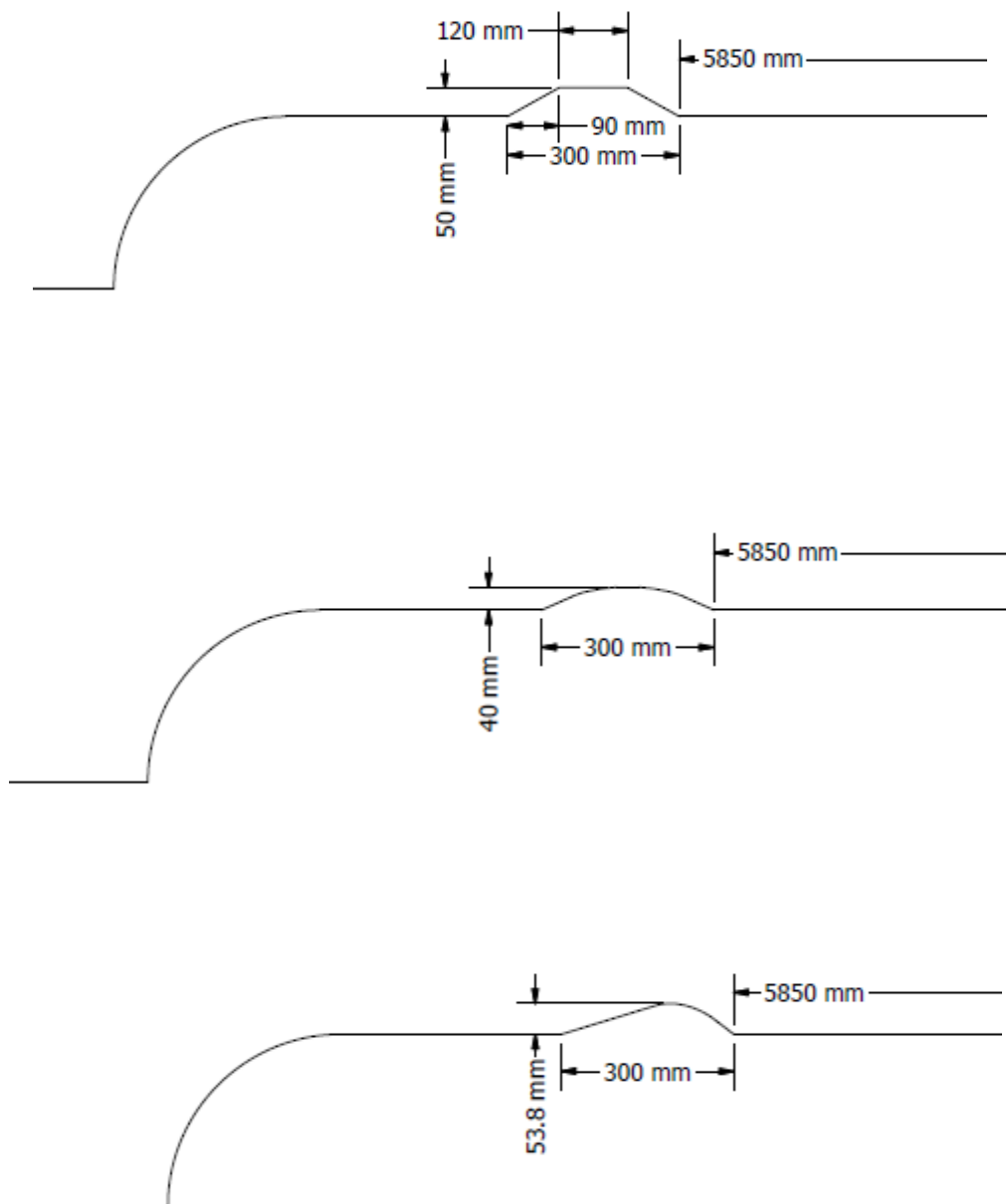


Figure 3.26 Geometries of designed sensor respectively from up for fist model, second and third

3.6. Results and discussion

In this chapter the researched sensors will be analysed for the most reliable case when they are mounted on a surface with elevation. Main goal of the research is to find the most optimal example of the sensors cover in regard of the aerodynamics.

3.6.1. Simulation of the flow

Simulation of the airflow over researched body is very important due to high risk of accumulating ice on the surface. In every simulation there are vortexes, one before and one after the sensors cover. Figures 3.27-3.29 shows velocity fields for all proposed sensor models.

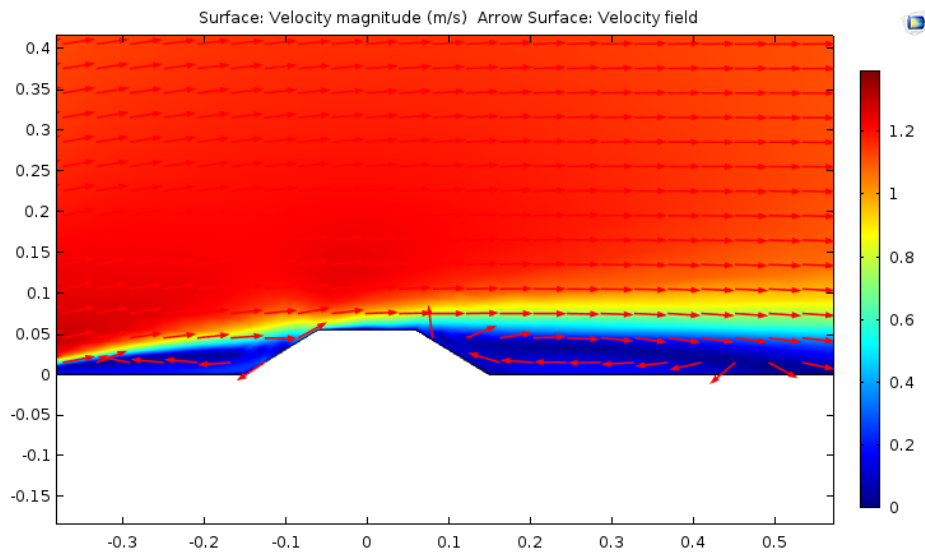


Figure 3.27 Velocity field with velocity indicators for flow over the first model of the sensor

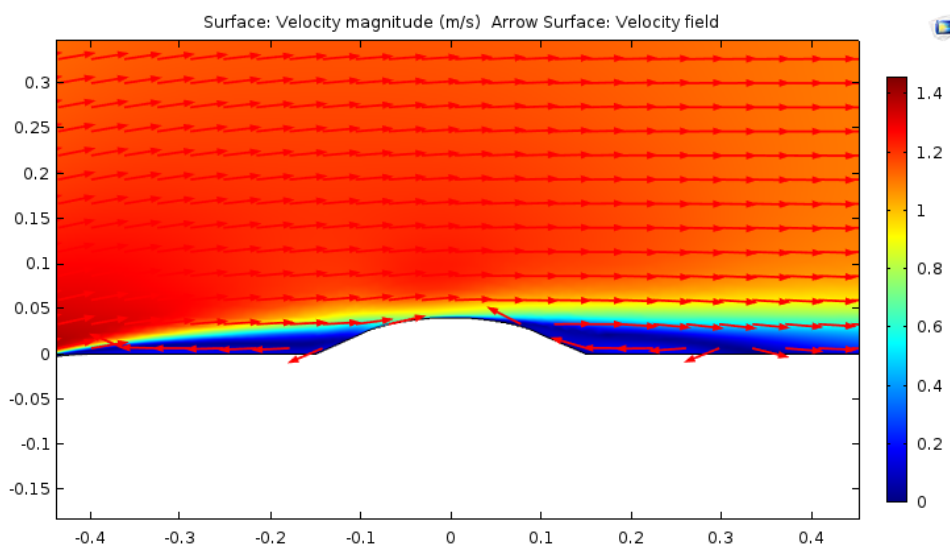


Figure 3.28 Velocity field with velocity indicators for flow over the second model of the sensor

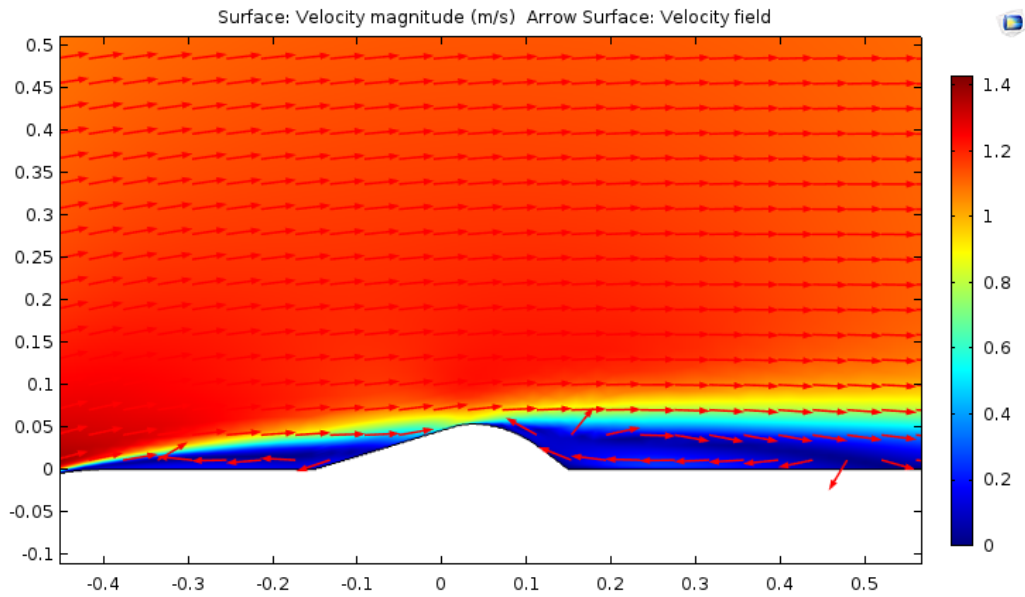


Figure 3.29 Velocity field with velocity indicators for flow over the third model of the sensor

The length of the vortex placed before the sensor changes only when there is free space to do so as seen in the velocity graph for the third example of the sensor where due to small angle of inclination of the sensors front edge of this vortex is longer than for the other models of the sensor. Height of this vortex, on the other hand, is not affected by the sensors because the flow is only modelled by the encountered obstacles and in this case the flow before the sensor is only influenced by the elevation of the sensors surface. The vortex located after the researched body is highly affected by the sensors geometry. Its length and height appears to change mostly with the height of the sensor. The vortex located behind the sensor is the smallest for the second model of the sensor where the vortexes length is equal approximately 0.25 m from origin point. For the two remaining models of the sensor the length of the vortex behind the sensor is very similar in both cases and is equal approximately 0.45 m from origin point. The cause of this phenomena is the difference in height of the second and the remaining sensors which is equal to 0.01 m. Origin point for this case is on the upper edge of the sensor where the flow separates.

The most desired are the smallest vortexes possible because they are created in small pressure fields and the velocity of the airflow is very small in the area. Icing problem will mostly occur in these areas where water and snow will accumulate.

3.6.2. Drag and lift coefficients and forces

Wind is generating aerodynamical forces that will act on the surface of the sensor. It is hard to predict the power and the behaviour of these forces. Results for forces were given in the Table 3.13.

Both programs directly computed forces and the coefficients were calculated afterwards. The smallest total force is for third sensor but that does not mean this solution is the best. The flow creates vortexes before and after the sensor which are affecting the coefficients and are undesirable. Very similar problem occurs in one of the tests of the analysis chapter: sensor mounted on elevated surface. The lift coefficient calculated as $C_l = 0.318$ which is smaller than for the researched sensors but the vortex behind the sensor is even larger its length is equal approximately 2 m from origin point.

Table 3.13 Forces and coefficients of drag and lift for designed sensors

	C_d [1]	C_l [1]	Characteristic length l [m]	Drag force F_d [N]	Lift force F_l [N]	Total force F [N]
First sensor	0.0277	0.48	0.317	0.00529	0.09163	0.09178
Second sensor	0.008	0.455	0.3143	0.00151	0.08612	0.08613
Third sensor	0.0292	0.394	0.323	0.00568	0.07664	0.07685

Regarding all of the sensor important features the best option is the second model of the sensor which has smaller coefficients than the first sensor because of smooth edges and smaller vortex behind the sensor of all proposed solutions thanks to smaller height of the sensor.

4. Analysis of the 3D CFD simulations

4.1. Wind turbine blade model and sensor locations

Within the framework of the “WiVind” project the research was carried regarding the wind turbine blade oscillations. Main goal of this research was to find the best sensor positions on the blade. Based on the performed simulations and frequency analyses, the following locations of the blade (given in distance to blade root) are most relevant for edge- and flapwise deflections and acceleration measurements:

- 43.8m, blade tip (covering 1st mode)
- 26-29m (2nd mode)
- 18-20m and 32-35m (3rd mode)

However, there are most likely practical issues which will prevent from putting a sensor on desired place. Blade shape is one of the problems (profile and chord length). It is impossible to mount a sensor on the blade tip. Fortunately there are not any hard restrictions regarding these sensor locations. They can be placed in other places near the ones that are desired and still work properly. The simulation results showed that the blade tip location is very relevant for sensor measurements, however, this fact is still valid for a location 0.5-1.0 m from the tip towards the hub. So there is no substantial problem in moving the sensor slightly towards the center of the rotor.

Following locations were chosen (given in distance to blade root):

- first sensor: 42.8 m
- second sensor: 34 m
- third sensor: 27 m
- fourth sensor: 19 m

Mentioned simulations do not include direct placement of the sensor (placement on the blade profile and even side of the blade). These analyses were based on the response data at the blade pitch axis, i.e., in the center of the blade profile. Figure 4.1 shows chosen side of the blade and l_s is distance between sensor and trailing edge.



Figure 4.1 Placement of the sensor on the wind turbine blade.

The pressure side was not chosen because there is high possibility the sensors would be damaged by objects in the flow and particles in the flow might produce noise when they hit the sensor. The front of the blade on the suction side was not considered simply because shape of the blade in that area.

For each sensor l_s is:

- first sensor: 0.08 m
- second sensor: 0.62 m
- third sensor: 0.7 m
- fourth sensor: 0.95 m

These simulations were made for a reference blade airfoil NREL 5MW. Figure 4.2 is showing the relative placement of each blade element to the pitch axis.

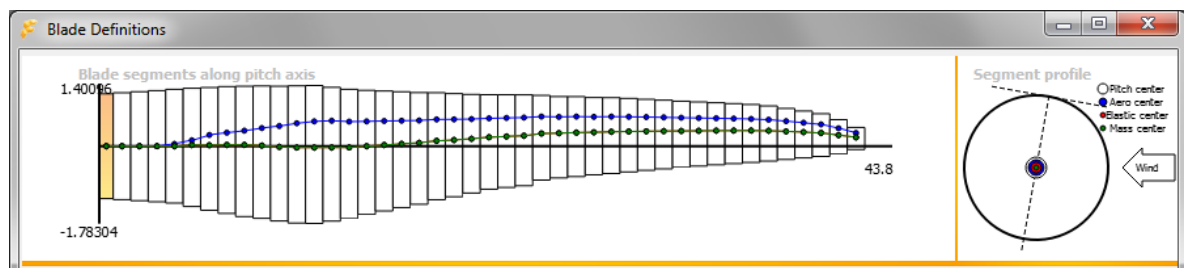


Figure 4.2 Blade definition

Later data containing properties of this reference wind turbine blade was used as an input file in the wind turbine simulation tool Ashes 2.3.0. Ashes is a software that performs integrated analyses of onshore and offshore wind turbines. This program created points for each profile of the airfoil and positioned them in space. Coordinates of each point was saved into STEP file.

Further work to create 3D model of the wind turbine blade was performed in Autodesk Inventor Professional 2014 on the STEP file from Ashes. The imported points were connected with control vertex splines creating each blade profile in a blade section. Control vertex was used because it formed smoother blade surface than interpolation spline. Now with loft tool each profile of the blade was connected and formed whole wind turbine blade.

Regarding the nature of the problem few approximations where made:

- The mentioned research at “WiVind” project did not need to model tip of the blade therefore tip in this model was approximately formed to fit this wind turbine blade shape. It is shown on the Figure 4.3.

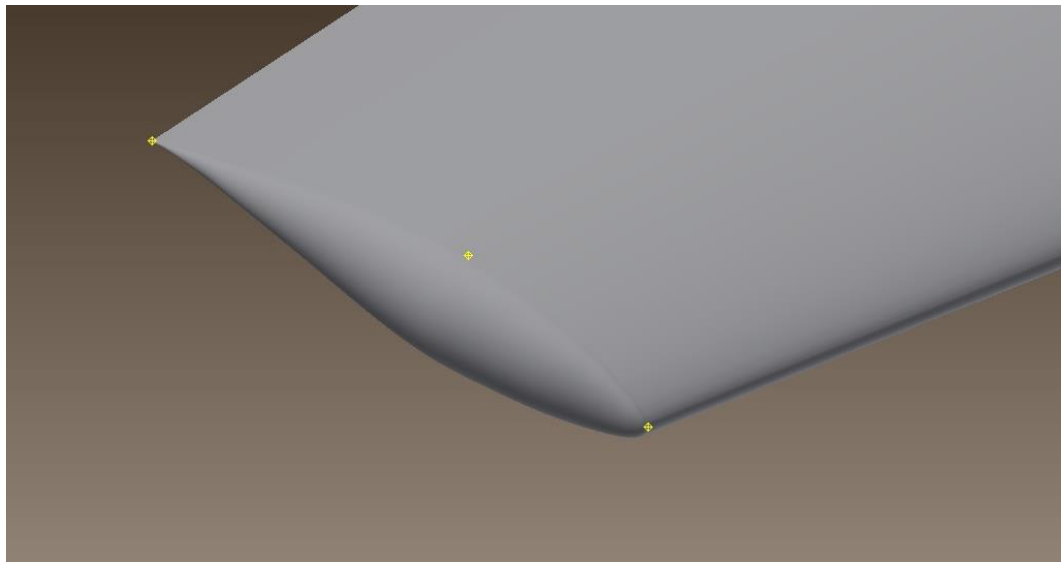


Figure 4.3 Wind turbine blade tip

- Near the trailing edge is a small curved area. That area needs very fine mesh and might produce convergence problems. In order to prevent that it was filled. That change does affect the flow around the wind turbine blade but not the flow around monitored sensor. That feature was repaired by creating additional loft which filled that area. This change is presented on Figures 4.4-4.5.

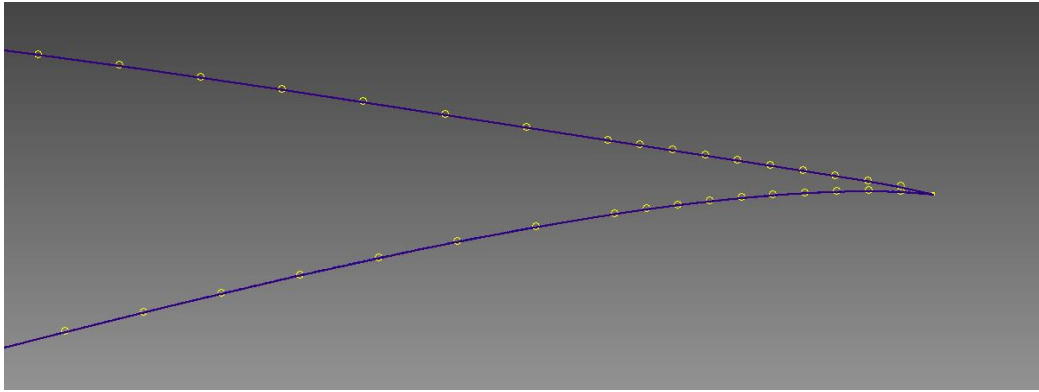


Figure 4.4 Trailing edge before change

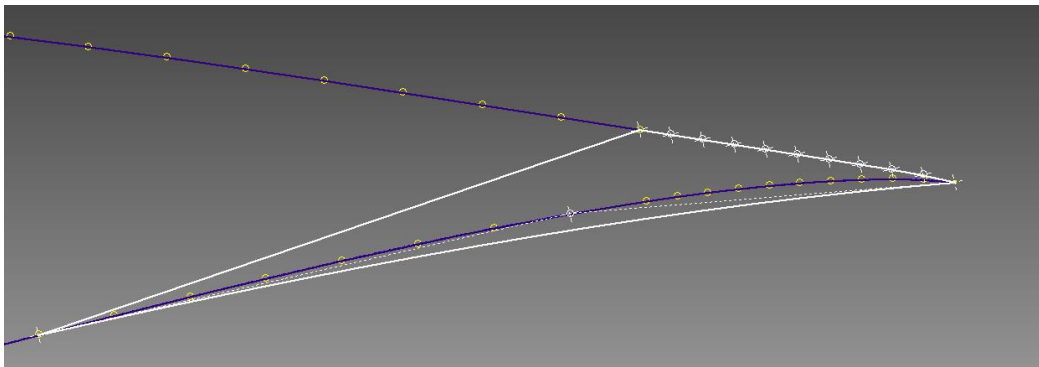


Figure 4.5 Trailing edge after change

- Closest sensor to the blade root is at distance of 19 meters, because of that the cylindrical profiles near the blade root where ignored. See Figure 4.6.

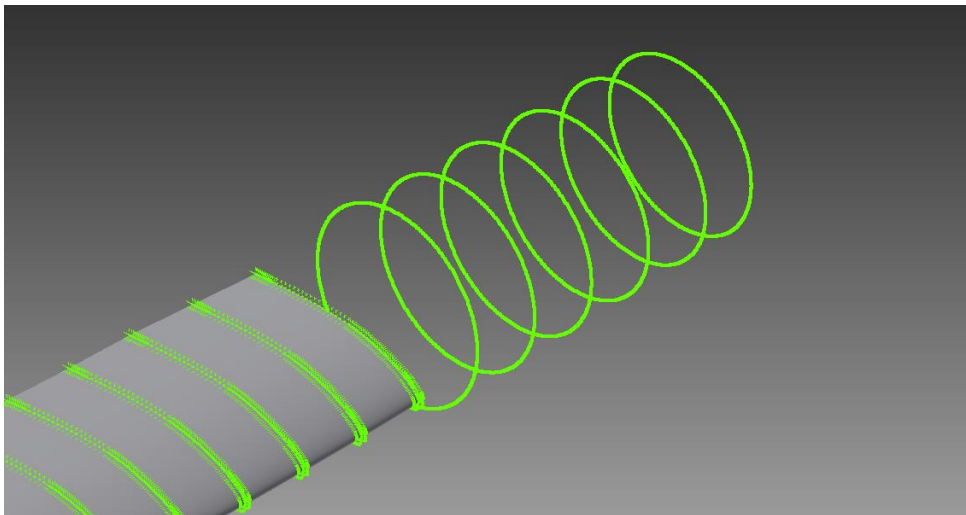


Figure 4.6 Ignored cylindrical area near the blade root

4.2. Sensors geometry

In project “WiVind” 2D flow simulations were performed around different models of a sensor mounted on a flat plate. Results from that project showed that the best aerodynamics (smallest drag and lift force) were for model with the smallest height and without sharp edges.

In this Master Thesis the 3D flow was analyzed and with the memory of mentioned properties of the sensor the following models were proposed:

- First model of a sensor has a shape similar to half of a sphere. This model is easy to produce and does not cover a lot of surface of the wind turbine blade. This design is streamlined for all directions which is his another advantage.

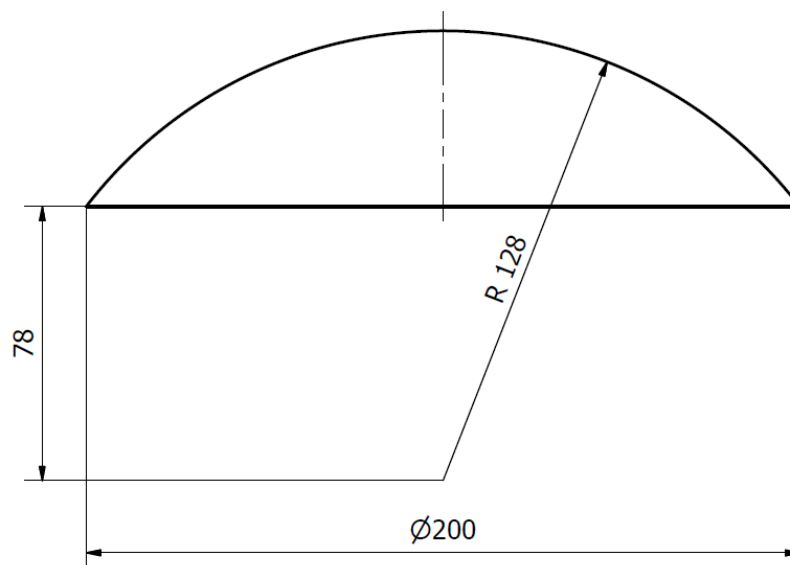


Figure 4.7 Geometry of the first sensor model

- Second model was inspired by arrowhead which should give this sensor more aerodynamical shape. Con of this model is that it might not work properly for flow incoming from other directions than the blade leading edge which because of high relative speed should not happen.

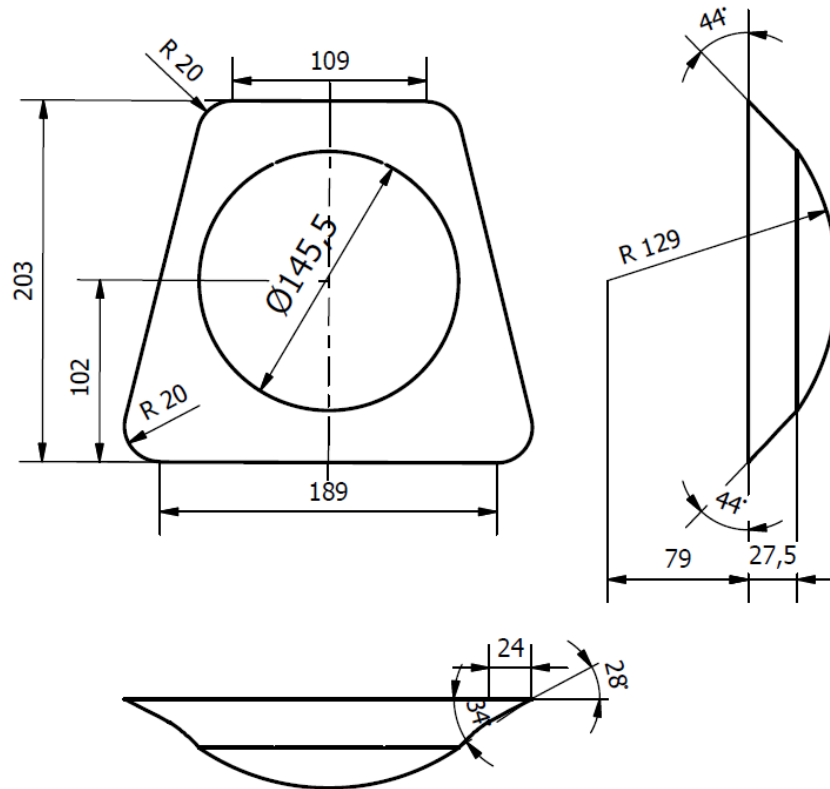


Figure 4.8 Geometry of the second sensor model

4.3. Control volume and boundary conditions

One of the solutions is to simulate whole wind turbine. That would allow to present flow with very high precision both in long and short distance from the wind turbine. These simulations would be more realistic. Unfortunately this solution requires very fine mesh with large number of cells and part of this mesh around wind turbine rotor would have to be able to rotate. Therefore this model would require high computing power and such complicated mesh would probably have convergence problems as well not to mention very long computing time. Work with that model would be very hard and uncomfortable. Each change could be applied after long computation time. This model validation would need even finer mesh and more simulation to check influence of the boundary conditions. Figure 4.9 shows example of a flow through wind turbine made by TotalSim company.

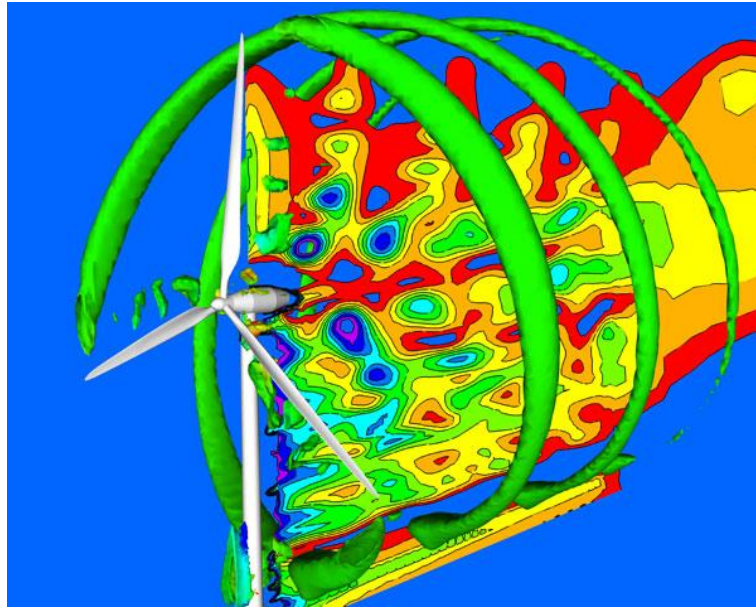


Figure 4.9 Flow simulation of flow through a wind turbine

Another solution is to simulate part of the wind turbine blade with mounted sensor. Mesh for this solution needs much less cells but will not be able to predict flow at long distance from the wind turbine. Figure 4.10 shows control volume and boundary conditions for this method. Separate model was created for each sensor mounted on the wind turbine blade. Idea for this solution was taken from the [16] where main goal was to simulate aeroacoustics of wind turbine blade. The correctness of this method was proven by comparing results with experimental data. In present work this method is not used directly because it involves very costly LES simulations. Instead SST simulations are performed. Therefore only control volume with the same boundary conditions but with different size is used. The difference in size results from the nature of analyzed problem. In present work most important matter is to properly simulate flow as well as the aerodynamic forces acting on the sensor.

Regarding boundary conditions few assumptions were made. Since this project has the most interest in flow specifically around sensor mounted on the blade there is no purpose to simulate flow far from the wind turbine. For the inlets:

- Relative velocity component of the wind parallel to the blade, in the horizontal direction, will be ignored, it is only meaningful far from the blade. For cells closer to the blade this component reduces significantly since it is the result of the rotation.

- Change in the relative velocity component of the wind in vertical direction though width of the control volume is very small. For width equal 1,4 m and rotational speed 1,76 rad/s, change for this velocity component is equal 2.46 m/s. For comparison the average relative wind velocity at inlet for the model closest to the blade root is equal approximately 44 m/s (with previous approximation applied).

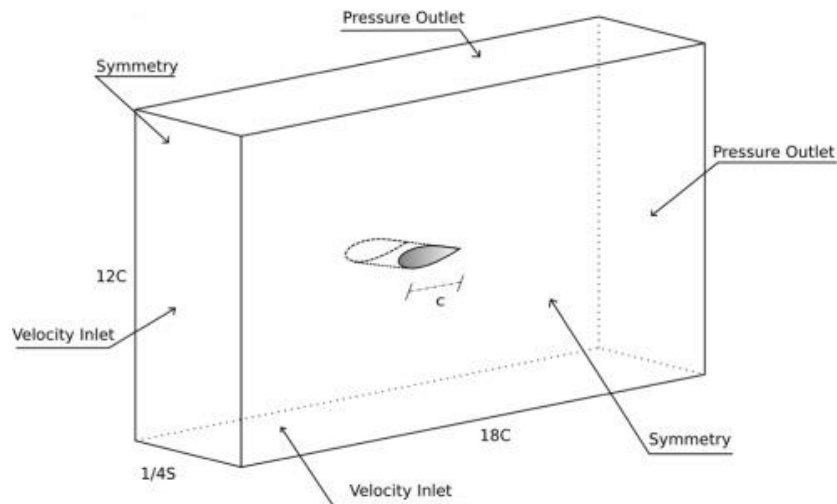


Figure 4.10 Rectangular domain used for the initial NACA0012 aeroacoustic simulations showing the boundary conditions. The chord length of the airfoil is C and the span is $1/4 S$ [16].

Application of the above assumptions removed any dynamic effects from models. The velocity on the inlet is constant and occurrence of the dynamic effects such as von Karman vortex sheet is impossible. All of these approximations changed these simulations from time depending to stationary which made these simulation much less computationally heavy.

Influence of used boundary conditions was checked by changing the distance of these boundaries from the analyzed sensor. This defined the final control volume size. This was performed only for the first sensor model for different locations on the wind turbine blade because second sensor model has similar size. The flow as well as the aerodynamic forces acting on the sensor were compared. The y^+ value was monitored to be smaller than 2 in order to fulfill the conditions of using SST turbulence model. Results are given in the Table 4.1. Values for all coefficients are similar.

Table 4.1 Control volume check for first sensors model in all locations on the wind turbine

	C_d [1]	C_l [1]	C_r [1]	l_t [mm]	$\max y^+$ [1]
The first model in the distance to the blade root 42.8 m					
without changes	0.068	0.511	- 0.01	$8 \cdot 10^{-6}$	1.8
increasing the distance from inlets to the sensor for 0.1 m	0.072	0.523	- 0.03	$8 \cdot 10^{-6}$	1.82
increasing the distance from symmetry walls to the sensor for 0.1 m	0.073	0.525	- 0.035	$8 \cdot 10^{-6}$	1.84
increasing the distance from outlets to the sensor for 0.1 m	0.067	0.509	- 0.02	$8 \cdot 10^{-6}$	1.81
The second model in the distance to the blade root 34 m					
without changes	0.111	1.076	0.044	$8 \cdot 10^{-6}$	1.45
increasing the distance from inlets to the sensor for 0.1 m	0.11	1.077	0.04	$8 \cdot 10^{-6}$	1.46
increasing the distance from symmetry walls to the sensor for 0.1 m	0.115	1.07	0.037	$8 \cdot 10^{-6}$	1.44
increasing the distance from outlets to the sensor for 0.1 m	0.112	1.08	0.039	$8 \cdot 10^{-6}$	1.47
The third model in the distance to the blade root 27 m					
without changes	0.151	1.112	- 0.021	$8 \cdot 10^{-6}$	1.41
increasing the distance from inlets to the sensor for 0.1 m	0.149	1.11	- 0.025	$8 \cdot 10^{-6}$	1.41
increasing the distance from symmetry walls to the sensor for 0.1 m	0.148	1.111	- 0.023	$8 \cdot 10^{-6}$	1.4
increasing the distance from outlets to the sensor for 0.1 m	0.153	1.114	- 0.026	$8 \cdot 10^{-6}$	1.43
The fourth model in the distance to the blade root 19 m					
without changes	0.195	1.241	0.062	$8 \cdot 10^{-6}$	1.4
increasing the distance from inlets to the sensor for 0.1 m	0.189	1.239	0.07	$8 \cdot 10^{-6}$	1.42
increasing the distance from symmetry walls to the sensor for 0.1 m	0.192	1.243	0.065	$8 \cdot 10^{-6}$	1.46
increasing the distance from outlets to the sensor for 0.1 m	0.194	1.245	0.063	$8 \cdot 10^{-6}$	1.43

4.4. Mesh validation

Mesh for the models is focused on the area around the sensor. In the far field this mesh is coarser because that area is not influencing the flow around the sensor. The hybrid mesh was chosen for this model with unstructured mesh around sensor and wind turbine blade and structure mesh further from the blade. Near wall boundary conditions additionally structured boundary layers were applied because in that area influence of the viscosity is much higher and structure mesh better presents these kind of areas.

Mesh influence on the flow was checked by changing its density for sensors in all locations. Results from this investigation are given in the Table 4.2. Coefficients for all sensors are not changing significantly.

Table 4.2 Mesh independence check for the first sensor model in all locations on the wind turbine blade

Chosen results as base	Number of degrees of freedom	C_d [1]	C_l [1]	C_r [1]	l_t [mm]	$\max y^+$ [1]
The first model in the distance to the blade root 42.8 m						
	956192	0.071	0.509	0.03	$8 \cdot 10^{-6}$	1.8
Base	1250366	0.068	0.511	0.01	$8 \cdot 10^{-6}$	1.8
	1684522	0.065	0.51	0.02	$8 \cdot 10^{-6}$	1.9
	2060060	0.066	0.508	0.03	$8 \cdot 10^{-6}$	1.94
The second model in the distance to the blade root 34 m						
	1150825	0.113	1.05	0.04	$8 \cdot 10^{-6}$	1.5
Base	2048391	0.111	1.076	0.044	$8 \cdot 10^{-6}$	1.45
	2452852	0.109	1.09	0.05	$8 \cdot 10^{-6}$	1.41
The third model in the distance to the blade root 27 m						
	1343323	0.153	1.11	-0.025	$8 \cdot 10^{-6}$	1.45
Base	2216498	0.151	1.112	-0.021	$8 \cdot 10^{-6}$	1.41
	2643243	0.152	1.114	-0.023	$8 \cdot 10^{-6}$	1.4
The fourth model in the distance to the blade root 19 m						
	1639583	0.189	1.236	0.071	$8 \cdot 10^{-6}$	1.45
Base	2343994	0.195	1.241	0.062	$8 \cdot 10^{-6}$	1.4
	2847722	0.197	1.243	0.065	$8 \cdot 10^{-6}$	1.42

4.5. Results and discussion

4.5.1. Aerodynamics

Reynolds number for each sensor in all locations on the wind turbine should be checked to prove that simulated flow is turbulent. For characteristic length equal chord length, Reynolds number equals from equation (10):

- for model in the 42.8 m from the blade root: $Re = 2789011.158$
- for model in the 34 m from the blade root: $Re = 6644694.349$
- for model in the 27 m from the blade root: $Re = 6881534.081$
- for model in the 19 m from the blade root: $Re = 7164465.888$

For characteristic length based on blade thickness, Reynolds number equals:

- for model in the 42.8 m from the blade root: $Re = 488066.0034$
- for model in the 34 m from the blade root: $Re = 1162785.607$
- for model in the 27 m from the blade root: $Re = 1445117.685$
- for model in the 19 m from the blade root: $Re = 1791101.974$

where:

- dynamic viscosity of the air $\mu = 1,81341 \cdot 10^{-5}$ Pa·s and density of the air $\rho = 1,2041$ kg/m³;
- for model in the 42.8 m from the blade root: $U = 82.45$ m/s , chord length = 0.50944 m, blade thickness = 0.08915 m;
- for model in the 34 m from the blade root: $U = 67.59$ m/s, chord length = 1.48056 m, blade thickness = 0.25909 m;
- for model in the 27 m from the blade root: $U = 56.12$ m/s, chord length = 1.84672 m, blade thickness = 0.38781 m;
- for model in the 19 m from the blade root: $U = 43.67$ m/s, chord length = 2.47078 m, blade thickness = 0.61769 m;

Reynolds number calculated in each way is much higher than 2300. This flow cannot be laminar either transitioning from laminar to turbulent. Normally, calculations of this dimensionless characteristic number are made for the chord length but locally blade thickness could be more important.

Analysis of the flow

This analysis is performed to justify the simulations of the flow and to check influence of the sensor on the flow. Wind turbines can work when the lift force acting on the blades is high enough. Direction and value of this lift force is influenced by the pressure on each side of the blade. Side with lower pressure and fast moving flow is called suction side and the other one with higher pressure and slow moving flow is called pressure side. Lift force is acting from the pressure side to the suction side causing the blades to move. Figure 4.11 is showing pressure and velocity fields on the slice perpendicular to the blade surface.

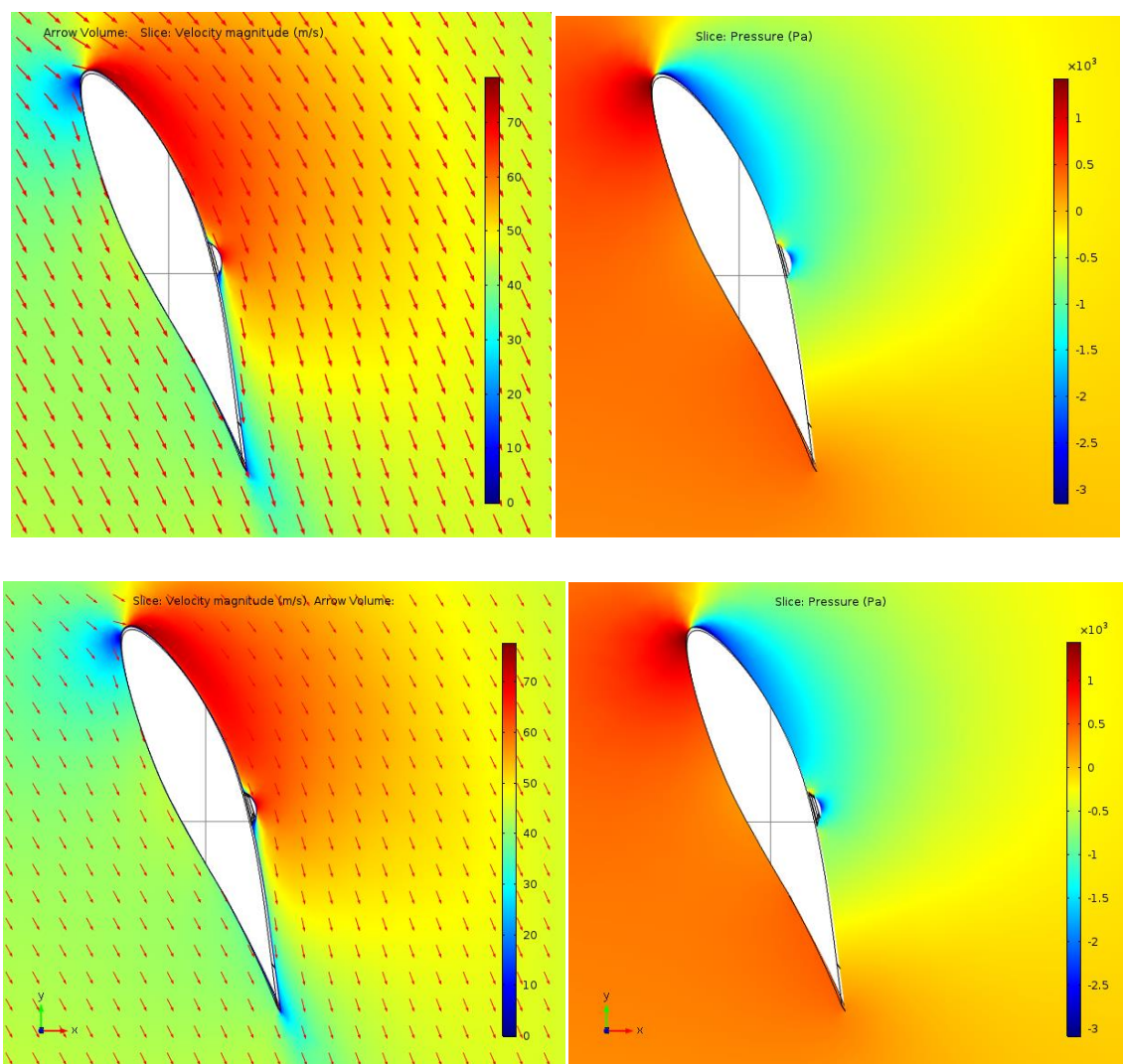


Figure 4.11 Pressure field and velocity field with velocity vector indicators for sensor mounted 19 m from the blade root. First sensor model on the top and the second below.

Blade movement was assumed to be from down to up. That means the lower side of the blade is supposed to be pressure side and upper is supposed to be suction side. Figure

4.11 is compatible with assumptions, on the lower side there is high pressure with slow moving flow and on the other side is low pressure with fast moving flow. This resembles pressure and suction sides. Pressure is not evenly distributed along the surface of the blade because force should be directed (in this case) vertically not perpendicular to the blade surface. Velocity vector indicators only show direction of the flow not its magnitude.

Figure 4.12 is showing streamline along the blade profile. On this graph the stagnation point is visible where the flow divides. These lines do not curve too much which means the flow does not separate and goes smoothly near the surface of the wind turbine blade.

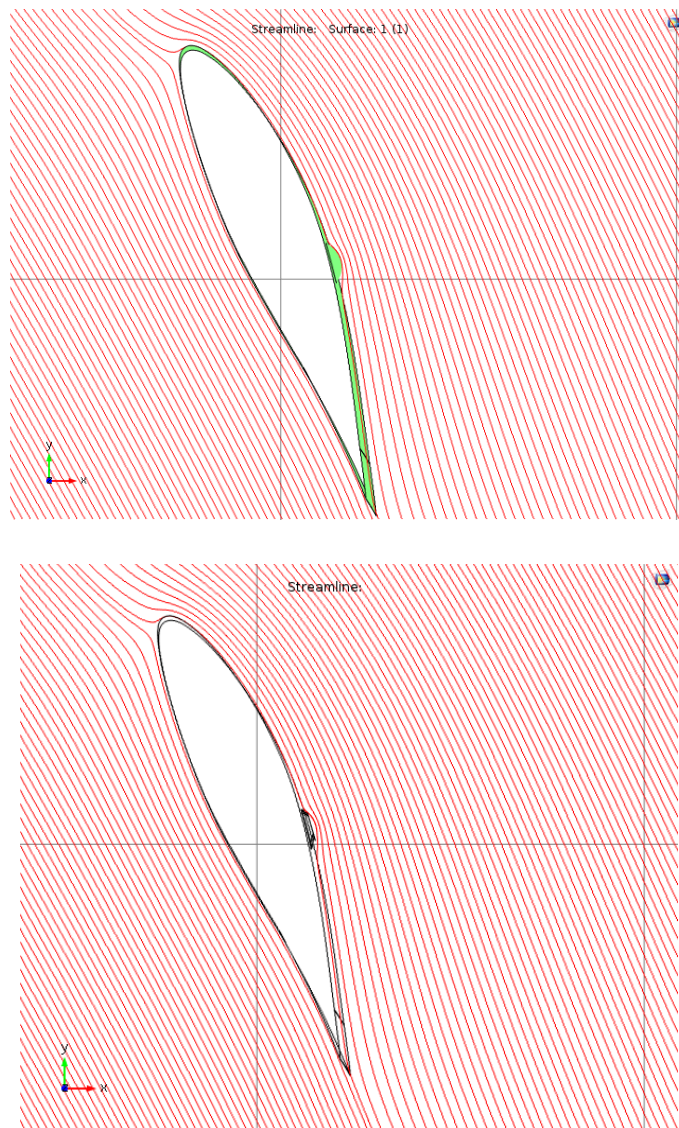


Figure 4.12 Streamlines for model with 19 meter distance to the blade root. On top is the first sensor model below the second.

Flow around each sensor model with 19 meter distance from the blade root is shown on the Figures 4.13 below. Disruptions of the flow made by sensor are not influencing the general flow around wind turbine blade. Separation area is very small, much smaller than the sensor itself. This means near the researched object did not develop any kind of vortexes. Vortexes in the separation area as well as this area could produce aeroacoustic noise and ice could accrete much easily. In Appendix A velocity and pressure fields are shown for the other locations.

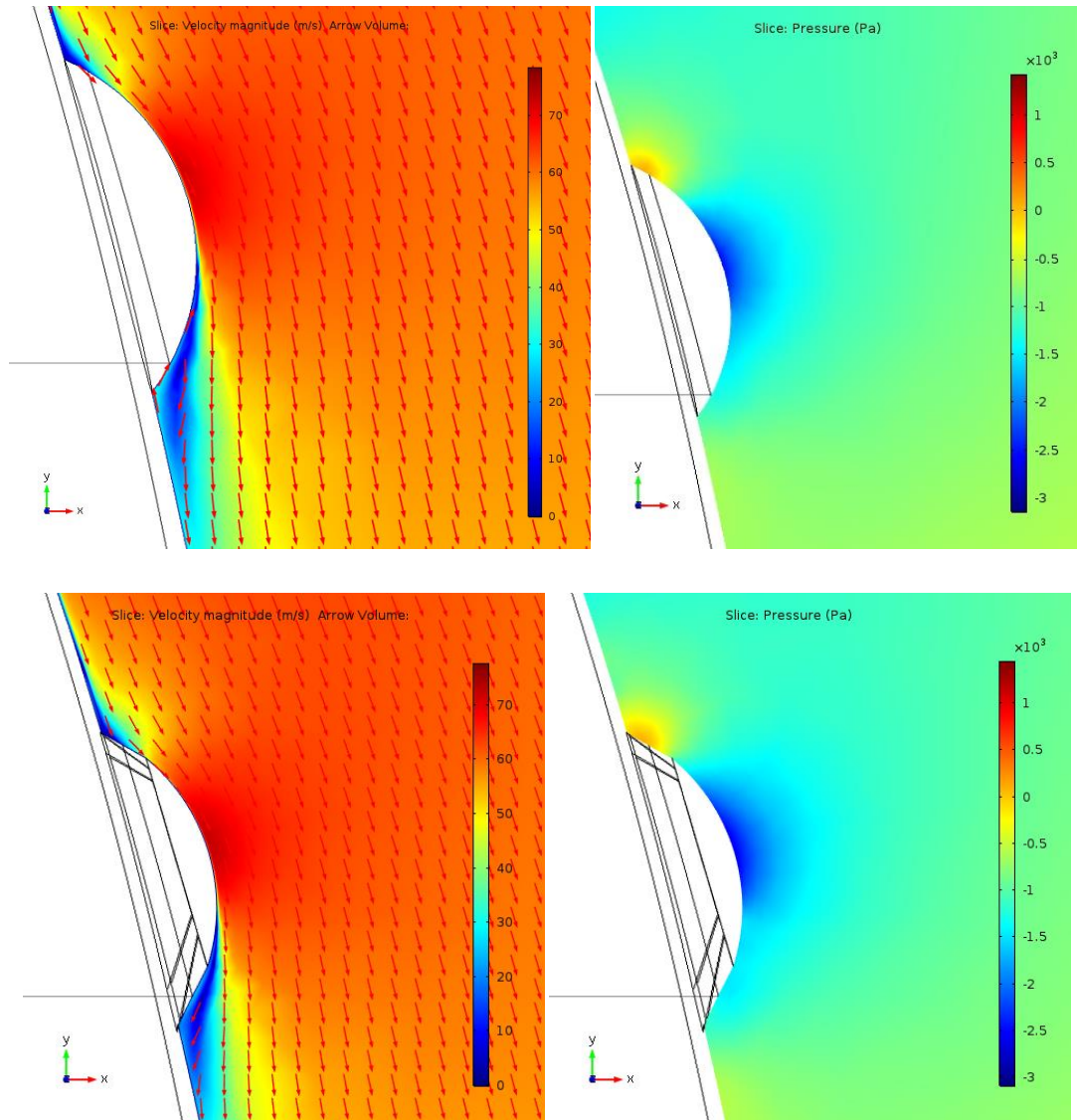


Figure 4.13 Velocity with velocity vector indicators and pressure field for sensor model places 19 meters from the blade root for both sensor models with first on the top and second below

Figure 4.14 presents flow alongside wind turbine blade for first sensor model in all locations. This graphs shows that there should be small force acting in this direction. For each sensor location it seems that this radial force is in different direction. For 19 and 34

meter from the blade root this force is from blade root to the blade tip and for the others is in the opposite direction. This strange behavior may be caused by the received data about wind turbine from the "WeVind" project. In that project oscillations of the wind turbine blade were checked on the flexible blade and that is responsible for different angle of attack for each sections of the blade. In the next subchapter, where the forces are described, value of this force is not immense in comparison to the total force so this feature will be ignored.

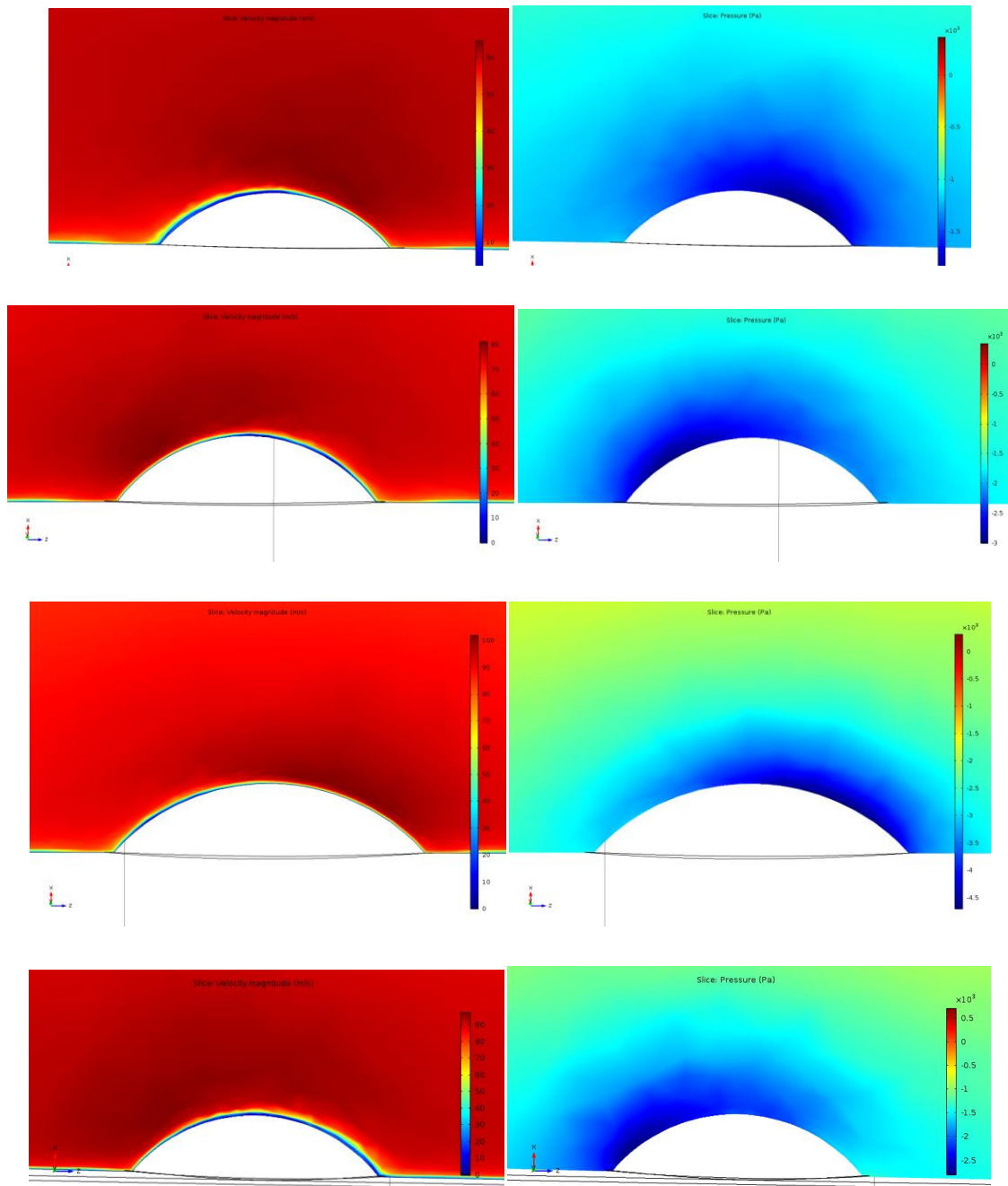


Figure 4.14 Velocity and pressure fields alongside the wind turbine blade for the first sensor model located, from the top: 19, 27, 34, 42.8 meters from the blade root.

This phenomenon does not occur for the second model. All velocity fields look very similar, with the same pattern. Higher pressure is on the right side causing radial force to act from blade tip to the root. Figure 4.15 show example of this fields for the sensor with 19 meter distance from the blade root. In Appendix A are graphs for the other locations.

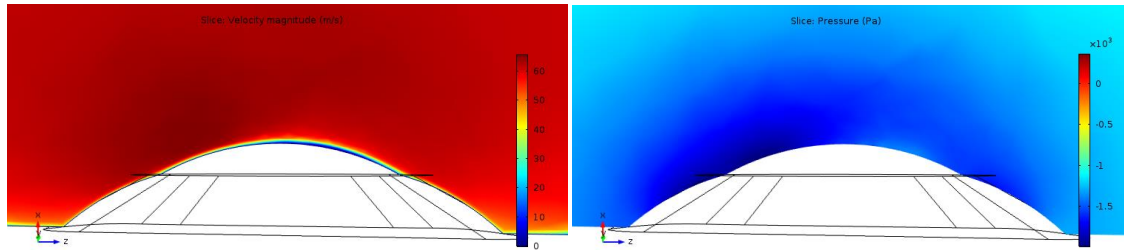


Figure 4.15 Velocity and pressure fields alongside the wind turbine blade for second sensor model located, 19meters from the blade root.

On the figure 4.16 pressure distribution on the blade surface around the sensor is shown. This distributions presents where and which forces are acting on the sensor. In the front of this sensor is a small area with high pressure creating mostly drag force, on the top and the sides is low negative pressure area which is causing mostly lift force and on the back there is low pressure area but very close to zero helping drag force . In Appendix A are graphs for the other locations.

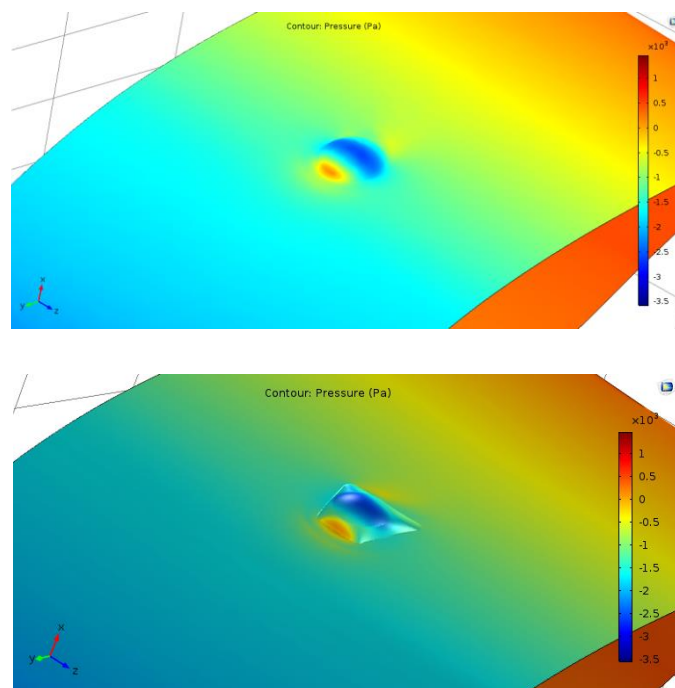


Figure 4.16 Pressure distribution on the blade surface around the sensors with the 19 meter distance from the blade root

Aerodynamic forces were calculated based on performed simulations for each proposed sensor model in all locations on the wind turbine blade. Both force sources: pressure as well as the shear stress were included. Results from this analysis are given in the Table 4.3.

Table 4.3 Aerodynamic forces for both sensors in all locations on the wind turbine blade

	U [m/s]	A [m ²]	C _d [1]	C _l [1]	C _r [1]	F _d [N]	F _l [N]	F _r [N]	F [N]
Distance from the sensor model to the blade root 42.8 m									
1 sensor	82.45	0.038	0.068	0.511	0.01	10.53	79.45	-1.59	80.16
2 sensor	82.45	0.042	0.051	0.449	0.03	8.8	77.18	5.12	77.85
Distance from the sensor model to the blade root 34 m									
1 sensor	67.59	0.038	0.111	1.076	0.044	11.64	112.4	4.65	113.1
2 sensor	67.59	0.042	0.093	1.054	0.023	10.7	121.7	2.71	122.2
Distance from the sensor model to the blade root 27 m									
1 sensor	56.12	0.038	0.151	1.112	0.021	10.86	80.1	-1.54	80.85
2 sensor	56.12	0.042	0.132	1.083	0.022	10.48	86.26	1.73	86.91
Distance from the sensor model to the blade root 19 m									
1 sensor	43.67	0.038	0.195	1.241	0.062	8.49	54.16	2.7	54.89
2 sensor	43.67	0.042	0.185	1.291	0.002	8.94	62.26	0.11	62.9

Negative value for radial force, F_r , means this force is directed from the blade tip to the blade root. From all forces, lift force is almost ten times bigger than the others. It happens because on the suction side there is a negative pressure area causing blade to move upwards. Change in the sign of the F_r proves shows problem explained given before. Even though total forces are higher for the second sensor model than for the first the coefficients are very similar. These coefficients were calculated based on the total area of the sensor which means the shape of the sensor did not affect the aerodynamical forces acting on it. Total area was the most important factor. Smaller forces are exerting on the sensor mounted near the blade tip than for the next one. That happens because blade drastically changes shape near the tip.

Critical position of the sensor on the blade profile

When sensor is mounted close to the place where the thickness of the blade profile is highest, flow will be highly disrupted. Behind the sensor flow will separate creating huge vortex and high pressure area. This happens for the both analyzed sensor models. Figure 4.17 presents velocity and pressure fields for the both sensor models in this location with 19 meter distance to the blade root.

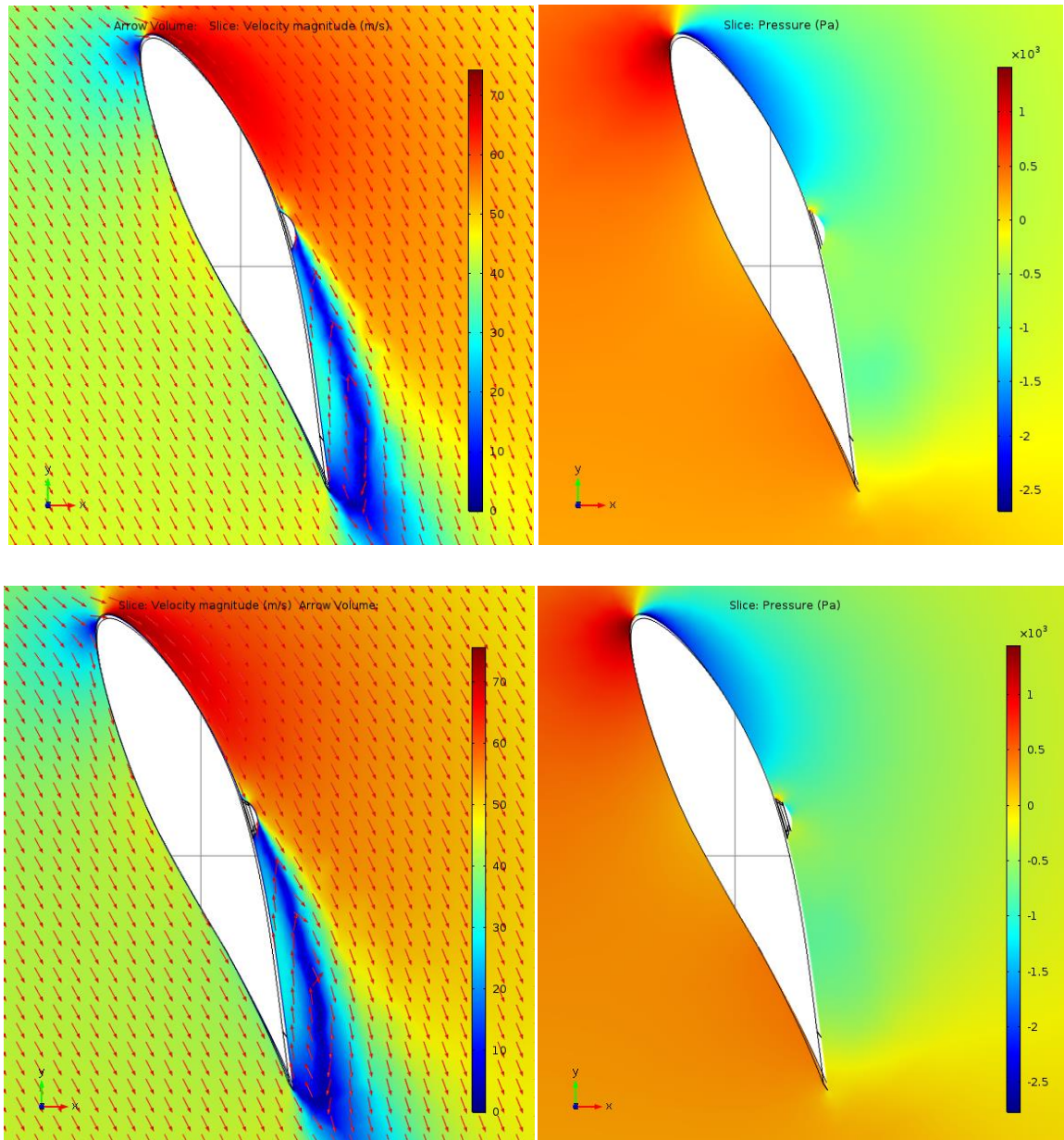


Figure 4.17 Pressure field and velocity field with velocity vector indicators for sensor mounted 19 meters from the blade root near the critical position. First sensor model on the top and the second below.

Based on the results from Table 4.4 total force acting on the sensor is much smaller for this location than the previous one. Flow is very slow behind the sensor which will create high pressure area reducing drag and lift force. This is explained on the figure 4.18 where pressure is high on the back side of the sensor.

Table 4.4 Aerodynamic forces for both sensors placed near the critical position with 19 meter distance from the blade root

	U [m/s]	A [m ²]	C _d [1]	C _l [1]	C _r [1]	F _d [N]	F _l [N]	F _r [N]	F [N]
1 sensor	43.67	0.038	0.195	1.241	0.062	0.63	22.65	0.5	22.66
2 sensor	43.67	0.042	0.019	0.471	0.015	0.92	22.7	0.72	22.73

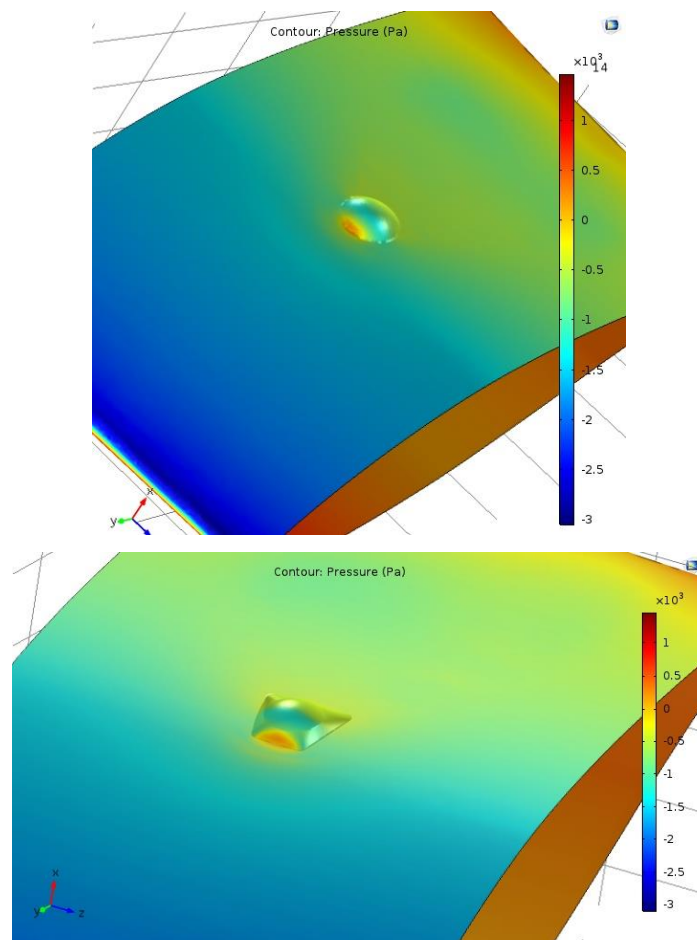


Figure 4.18 Pressure distribution on the blade surface around the sensors with the 19 meter distance from the blade root placed near the critical position

Even though forces are much smaller, this location is mostly disadvantageous. This flow will raise icing risk and create more noise from the separated flow. It can even affect

the efficiency of the wind turbine by reducing lift and drag force locally and creating unexpected disruption in the flow.

4.5.2. Aeroacoustics

NAFNoise program was used to predict aeroacoustical noise generated locally, only for the part of the wind turbine blade with a sensor mounted on it. Simulations were generated for the blade span equal 1.4 m. These simulations were not performed for whole wind turbine because NAFNoise does not include changes in the shape of blade such as different twist angle for each blade section. All the parameters used in this program are given in the Table 4.5.

Table 4.5 Parameters used in the NAFNoise - noise prediction code for airfoils

Distance from sensor model to the blade root [m]	Chord length [m]	Wind turbine rotation speed [rad/s]	Relative freestream wind velocity [m/s]	Pitch angle [deg]	Twist angle [deg]	β [deg]	Angle of attack [deg]
Wind velocity 24 m/s							
42.8	0.50944	1.78	82.45	16	0	16.23	0.23
34	1.48056	1.78	67.59	16	1.6665	19.55	1.8835
27	1.84672	1.78	56.12	16	3.3835	23.15	3.7665
19	2.47078	1.78	43.67	16	5.8075	28.79	6.9825
Wind velocity 18 m/s							
42.8	0.50944	1.65	75.28	13	0	13.45	0.45
34	1.48056	1.65	61.28	13	1.6665	16.37	1.7035
27	1.84672	1.65	50.35	13	3.3835	19.67	3.2865
19	2.47078	1.65	38.32	13	5.8075	25.16	6.3525
Wind velocity 12 m/s							
42.8	0.50944	1.54	69.27	7	0	9.83	2.83
34	1.48056	1.54	55.97	7	1.6665	12.1	3.4335
27	1.84672	1.54	45.5	7	3.3835	14.77	4.3865
19	2.47078	1.54	33.77	7	5.8075	19.56	6.7525
Wind velocity 6 m/s							
42.8	0.50944	1.43	63.63	3	0	5.39	2.39
34	1.48056	1.43	51.12	3	1.6665	6.69	2.0235
27	1.84672	1.43	41.19	3	3.3835	8.29	1.9065
19	2.47078	1.43	29.92	3	5.8075	11.34	2.5325

where β is vertical angle of inclination of the reference wind velocity

One additional simulation was carried out for sensor location 42.8 meter from blade root with freestream velocity equal 24 m/s but with blade span two times bigger - 2.8 m. Figure 4.19 shows sound pressure levels in function of sound frequency. Both cases seem to be identical even with different blade span. Actual difference is very small 2 dB for each frequency.

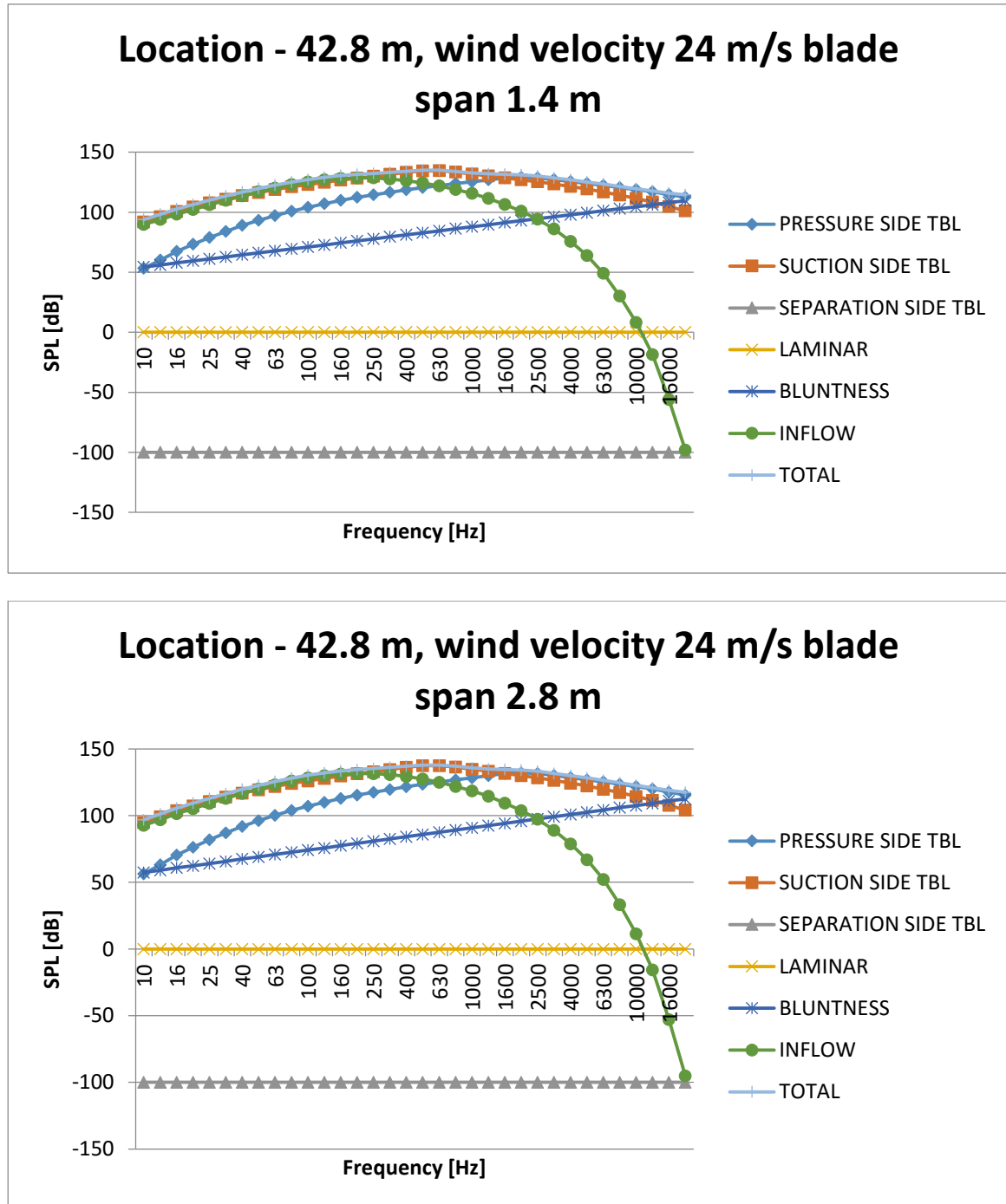
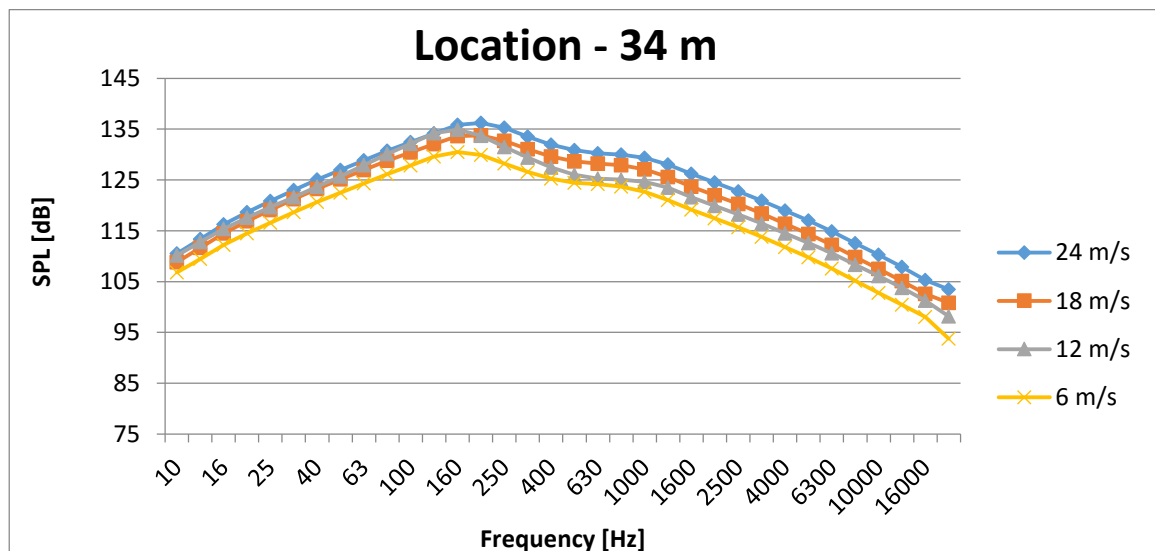
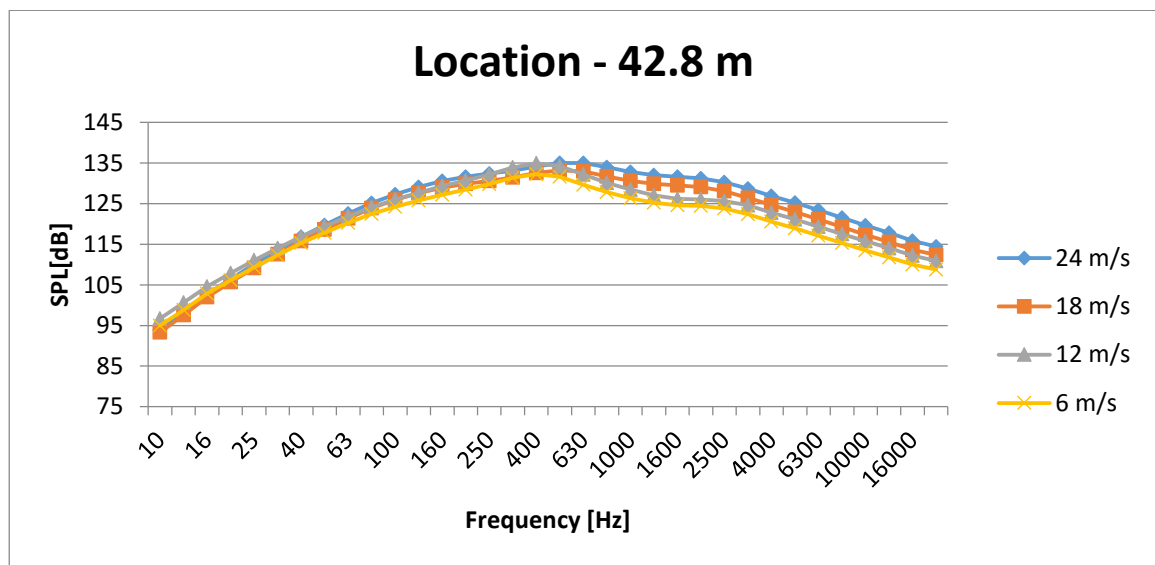


Figure 4.19 Comparison of the NAFNoise simulation with different span of the blade

On these graphs only noise generated by separation is different, not negative. It is important to remember sound pressure level is a logarithm of the acoustic pressure divided by reference pressure. Negative values of the SPL only mean the acoustic pressure is smaller than the reference one

Total SPL for each sensor location and all analyzed wind velocities are shown on the Figure 4.20. As expected smaller wind velocity is producing less noise but the difference is not that high, around 10 dB. It could be influenced by the changes in the angle of attack for each wind velocity.



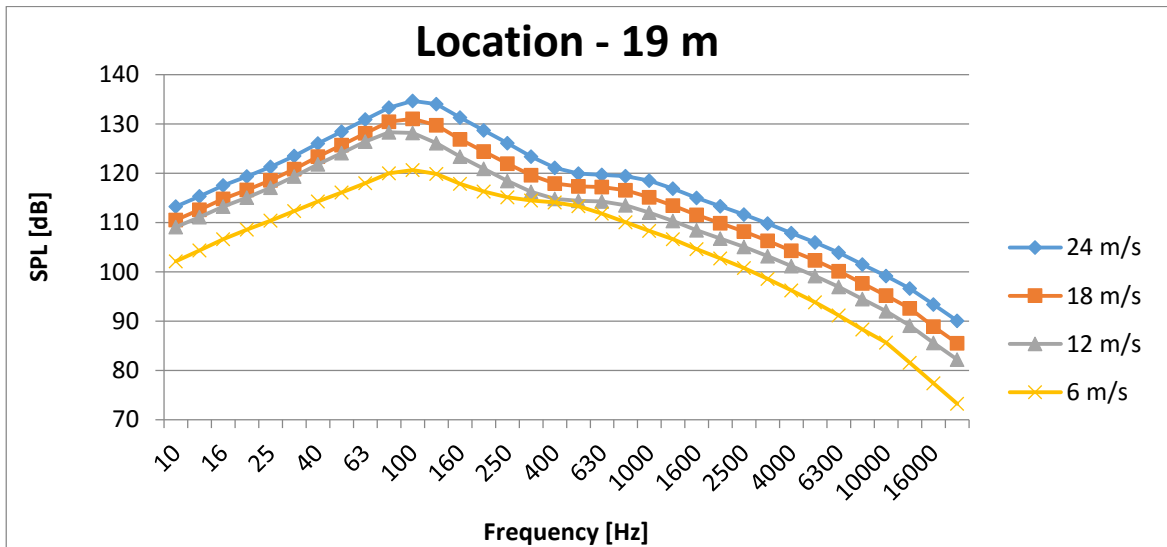
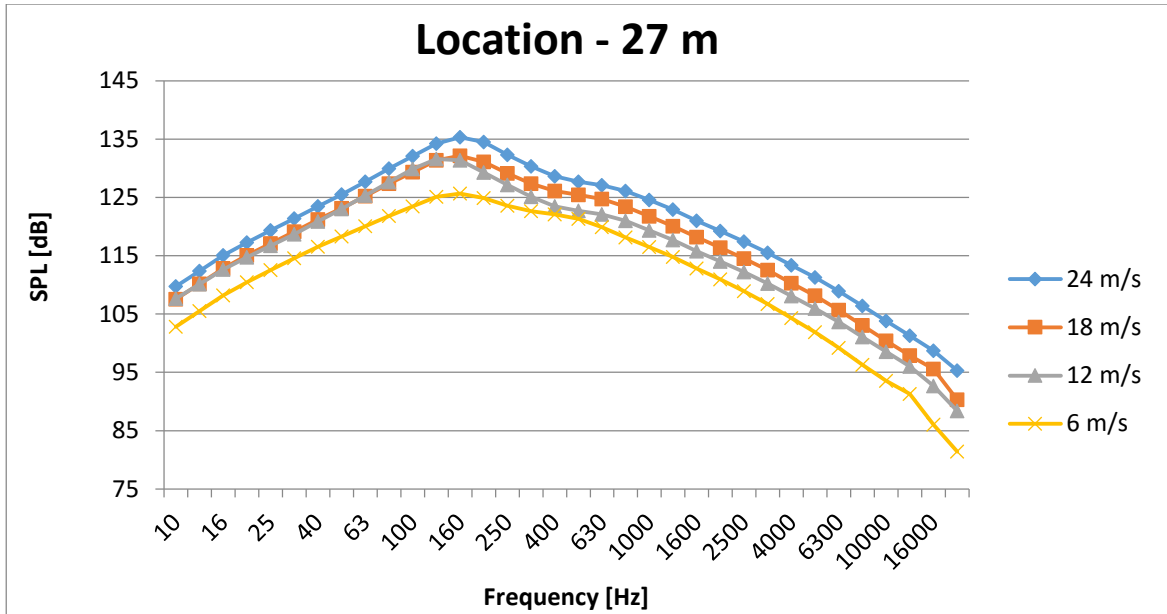


Figure 4.20 Comparison of total sound pressure levels for different freestream velocities for all sensor locations

4.5.3. Icing problem

Icing on the rotating wind turbine blade is very hard to simulate because of the conditions that are required to ice accumulation. Even trying to predict flow over an iced wind turbine blade is difficult because through this blade different ice types may appear. It happens because one of the many factors influencing the ice accretion is the reference wind speed. Through the blade, from the root, relative wind speed, as well as velocity of the super-cooled water droplets, is increasing resulting in accumulation of the ice with higher density.

Kjeller Vindteknikk has produced icing maps covering the Finnish, Swedish and the Norwegian territories that are publicly available. The icing maps have 50 m horizontal resolution and show the number of hours with active icing conditions during a normal year, giving a good indication of which areas are most exposed to icing.

The icing maps are generated based on temperature and humidity parameters from WRF simulations with 1 km horizontal resolution. These data, together with terrain data with 50 m resolution are used as input variables to a local icing model, which is solved with a 50 m resolution for the whole Finland, Sweden and Norway. The local icing model, which is developed by Kjeller Vindteknikk, is based on the ISO-standard “Atmospheric Icing of Structures” (ISO12494). Comparisons with measurements of icing in Sweden and Norway show that the model well describes the periods of icing.

The Weather Research and Forecasting (WRF) model is a numerical weather prediction (NWP) system designed to serve both atmospheric research and operational forecasting needs. NWP refers to the simulation and prediction of the atmosphere with a computer model, and WRF is a set of software for this. WRF generate simulations based on real data.

Based on the provided icing maps by Kjeller Vindteknikk icing in the Hundhammerfjellet Wind Farm area should occur maximum 200 hours per year. Fragment of this map with signed wind farm area is in the Figure 4.21. This means it ice will accrete on the wind turbines only for approximately eight and a half days. When this event occurs most of the HAWT wind turbines will be turn off by positioning blades in the neutral position, parallel to the flow direction. It happens to prevent ice from falling off with high

velocity which can damage nearby wind turbines and other objects as well as the bypassing people.

Sensor might give wrong results because accumulated ice will change the flow and aerodynamic forces acting on the wind turbine causing blade to oscillate which could mean it is damaged while it is not.

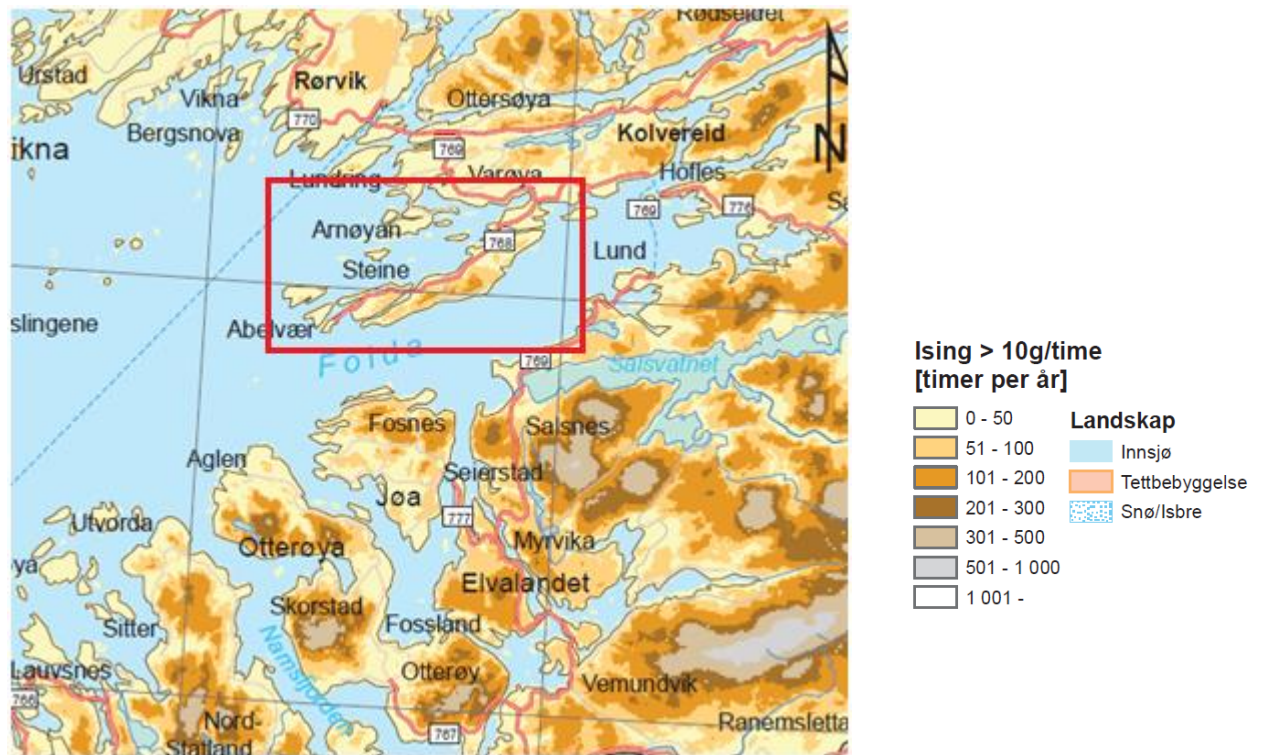


Figure 4.21 Icing map provided by Kjeller Vindteknikk company. Location of the wind turbine farm is marked with red square

5. Conclusions

In this master thesis analysis of the airflow, drag and lift forces as well as the coefficients were calculated for different shapes of the sensors. Simulations of the flow and the calculations of forces were done in the COMSOL Multiphysics 5.2. For each simulation mesh independency tests and control volume checks were done.

Initially, 2D computations were done for laminar flow to check mesh and control volume size. Turbulent flow simulations were done to test k epsilon and k omega SST turbulence models. In the analysis chapter the accuracy of the program was checked by simulating the test case of flow over a cylinder for which experimental data was used to compare the results. COMSOL was accurate for both laminar and turbulent flow. Turbulence k epsilon model was less accurate than the k omega SST.

The analysis of two test cases was performed for sensor mounted on a flat surface and for sensor mounted on a flat surface with elevation where in both cases the sensor had a shape of a half cylinder. From these simulations results for k epsilon model were different but for k omega SST they were compatible. That implied in that the next turbulence calculations were done only with the k omega SST model. Based upon results from performed analysis researched sensors will be mounted on a flat surface with elevation which is more reliable than without elevation because it is closer to reality where the sensor is placed on a wind turbine blade in neutral position.

Three shapes of the sensors were designed and rated based on the aerodynamical forces and wake size. Both features should be as small as possible. The most optimal sensor was the one with the smallest height and smooth edges. Thanks to the small height the vortex area behind the sensor was small and the smooth edges helped with reducing the drag force.

The 3D computation were performed on reference wind turbine blade NREL 5MW with the highest possible wind velocity of 24m/s. In order to reduce the number of cells in the computational domain these simulations were performed only for sections of the blade with mounted sensors. Based on the previous analysis, only two models of the sensor were proposed. Sensors were mounted on the suction side of the blade behind the area where the thickness of the blade is highest. The pressure side was not chosen because there is a high possibility that the sensors would be damaged by objects in the flow and particles in the

flow might produce noise when they hit the sensor. The front of the blade on the suction side was not considered simply because the shape of the blade in this area is strongly curved.

Flow for proposed sensors and their placement does not separate too much which means that this flow should not affect the wind turbine. For both sensors the force coefficients were very similar. Shape of the sensors did not influence the flow and the higher total force for the second sensor was simply because it had a bigger reference area.

Additional models were created with sensor mounted very close to the place where the thickness of the blade is large. The flow changed drastically behind the sensor, a huge separation area developed. Even though the total aerodynamical force was halved this flow could produce noise and raise the risk of icing, not to mention it could even reduce the efficiency of the wind turbine by reducing lift force acting on the blade.

Aeroacoustics were checked by using the 2D noise prediction code NAFNoise developed by the NREL institute. This code tries to predict sound pressure level for different frequencies of the noise based on different velocities of the freestream wind. SPL for each wind velocity was quite similar, approximately 10 dB difference for each frequency.

Icing was checked by using the icing maps based on the WRF model produced by Kjeller Vindteknikk company. On the map the area of the analyzed Hundhammerfjellet Wind Farm was found. Based on the map, the ice problem could occur maximum 200 hours per year which is around eight and a half days. Ice can change the flow around wind turbine causing the blade to oscillate more which could deceive the sensor.

6. Further work

Experimental data was provided only for the test case of flow over a cylinder which is actually not enough to conclude that the other calculation were accurate. Final results should be compared to experimental data as due to numerical errors and how they will behave for different flows.

Simulations were done for 2D cases without any time depending dynamics, but in 3D the flow may be transient. Simulations for the sensors in all other possible locations such as pressure side of the blade should be performed even though sensor might be damaged in this area could be still beneficial.

Large Eddy Simulations should be carried out in order to predict aeroacoustics of the blade with a sensor mounted on it. These simulations should be more precise and include influence of the sensor on the flow and noise generation. It could be possible to observe the noise propagation as well. Experiment would also be required.

Icing is highly affected by local topography and shape of the wind turbine blade. This features can be applied into the WRF model. Still experiment should be performed to validate this method.

7. References

1. E.L. Houghton & P.W. Carpenter: "Aerodynamics for Engineering Students. Fifth Edition", Butterworth-Heinemann, 2003
2. . Milton C. Shaw: "Engineering Problem Solving - A Classical Perspective", William Andrew Publishing/Noyes, 2001
3. H. K. Versteeg & W. Malalasekera: "An introduction to computational fluid dynamics. The finite volume method", Longman Scientific & Technical, 1995
4. M. Van Dyke: "An Album of Fluid Motion", THE PARABOLIC PRESS, 1988
5. Sercan Yagmur, Sercan Dogan, Muharrem H. Aksoy, Eyub Canli, Muammer Ozgoren: "Experimental and Numerical Investigation of Flow Structures around Cylindrical Bluff Bodies", EDP Sciences, 2015
6. S. Dong, G.E. Karniadakis: "Journal of Fluids and Structures 20 (2005) 519–531. DNS of flow past a stationary and oscillating cylinder at $Re = 10\,000$ ", Elsevier, 2005
7. Comsol 5.1 User Guide. CFD Module, Available in the program documentation
8. Patrick Moriarty.: " NAFNoise User Guide" NREL 2005 available from: <https://nwtc.nrel.gov/NAFNoise>
9. SMS-491: "Physical solutions of everyday problems in aquatic sciences. Lecture 5: High Re 's flows" Available on website: http://misclab.umeoce.maine.edu/boss/classes/SMS_491_2003/Week_5.htm
10. Efstathios Konstantinidis and Demetri Bouris: "Bluff Body Aerodynamics and Wake Control, Applied Aerodynamics", InTech, 2012 Available from: <http://www.intechopen.com/books/applied-aerodynamics/bluff-body-aerodynamics-and-wake-control>
11. Zikanov, O.: "Essential Computational Fluid Dynamics", John Wilay & Sons Inc., 2010
12. Guido Buresti: "BLUFF-BODY AERODYNAMICS", Department of Aerospace Engineering University of Pisa, Italy, 2010
13. http://www.pilotfriend.com/training/flight_training/aero/drag.htm
14. <http://www.mh-aerotoools.de/airfoils/bubbles.htm>
15. Erik Rindeskär : " Modelling of icing for wind farms in cold climate" Examensarbete vid Institutionen för Geovetenskaper ISSN 1650-6553 Nr 201
16. Sahan H.Wasala, RupertC.Storey, StuartE.Norris, JohnE.Cater : "Aeroacoustic noise prediction for wind turbines using Large Eddy Simulation" available at: <http://www.sciencedirect.com/science/article/pii/S0167610515001336>

Appendix A

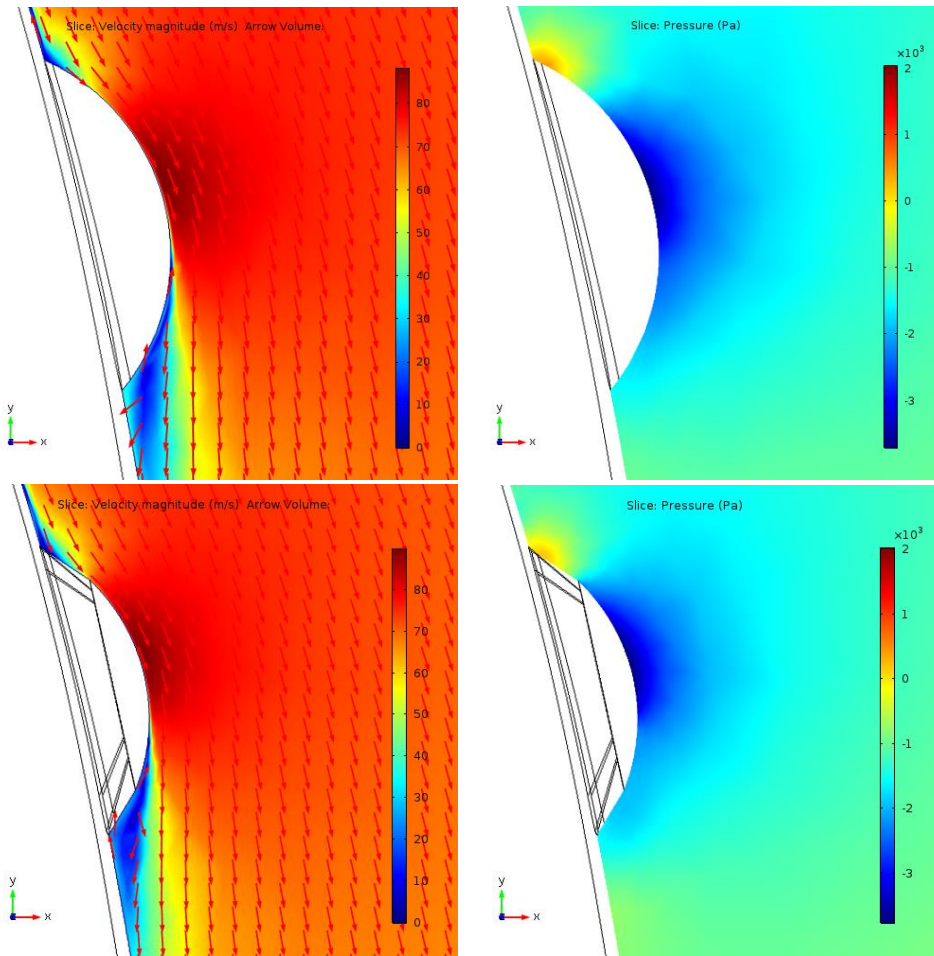
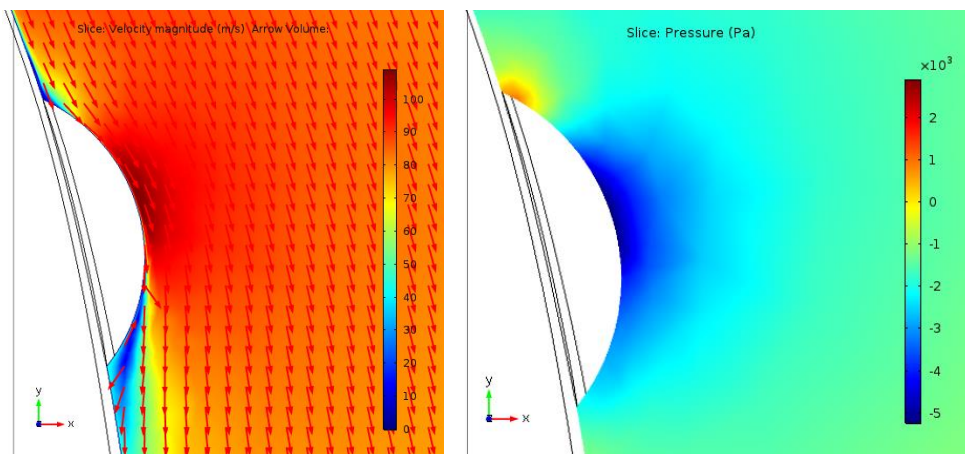


Figure A.1 Velocity with velocity vector indicators and pressure field for sensor model places 27 meters from the blade root for both sensor models with first on the top and second below



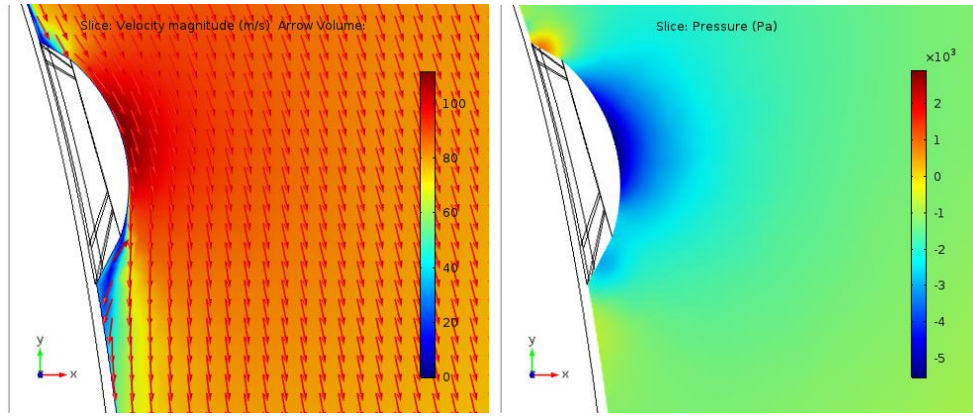


Figure A.2 Velocity with velocity vector indicators and pressure field for sensor model places 34 meters from the blade root for both sensor models with first on the top and second below

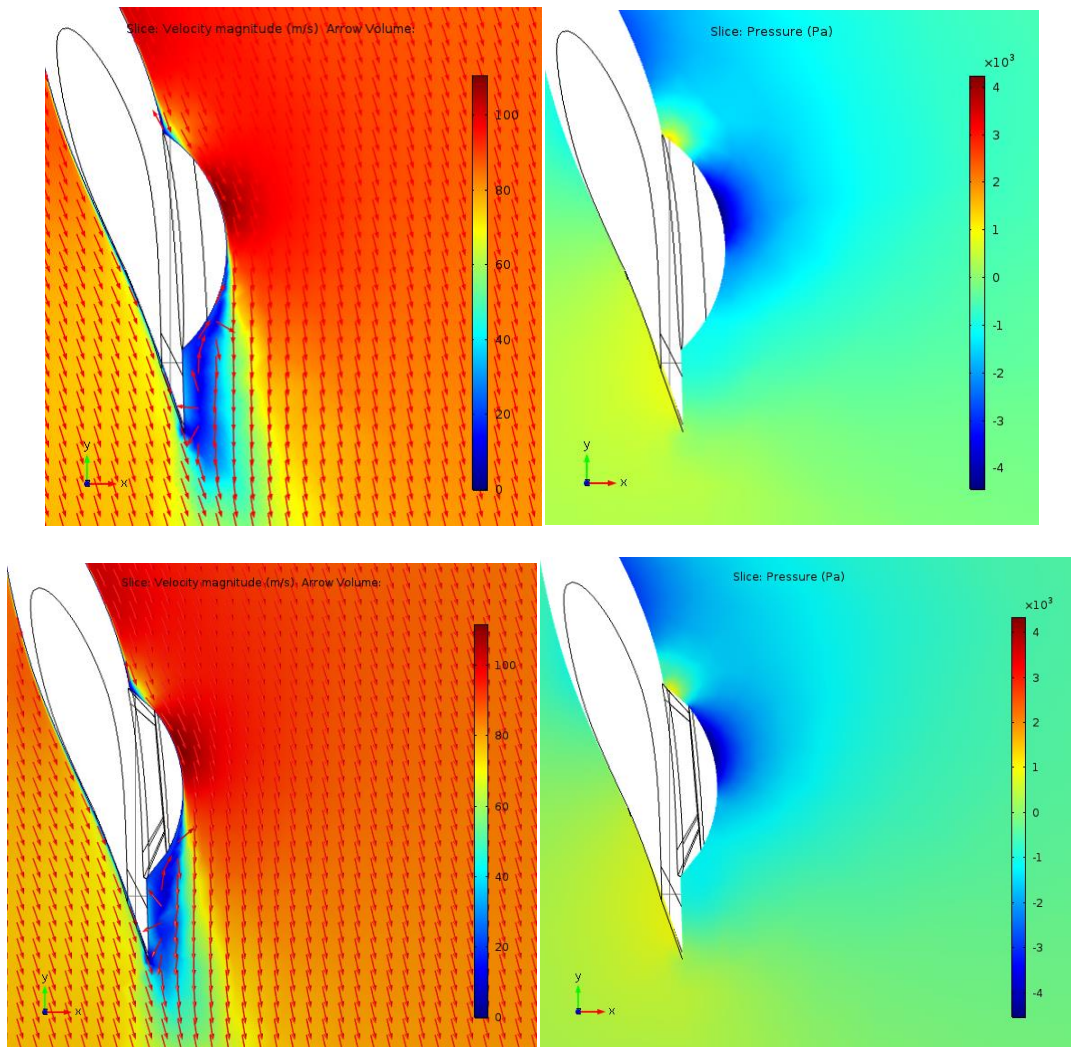


Figure A.3 Velocity with velocity vector indicators and pressure field for sensor model places 42.8 meters from the blade root for both sensor models with first on the top and second below

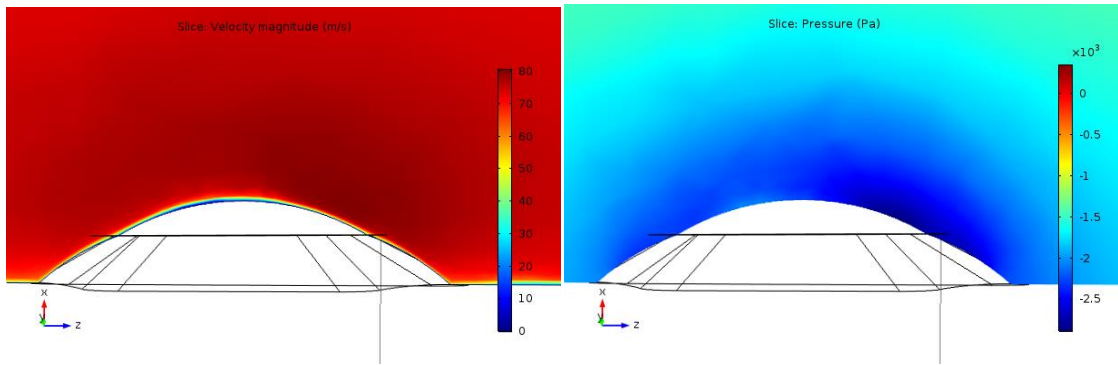


Figure A.4 Velocity and pressure fields alongside the wind turbine blade for second sensor model located, 27 meters from the blade root.

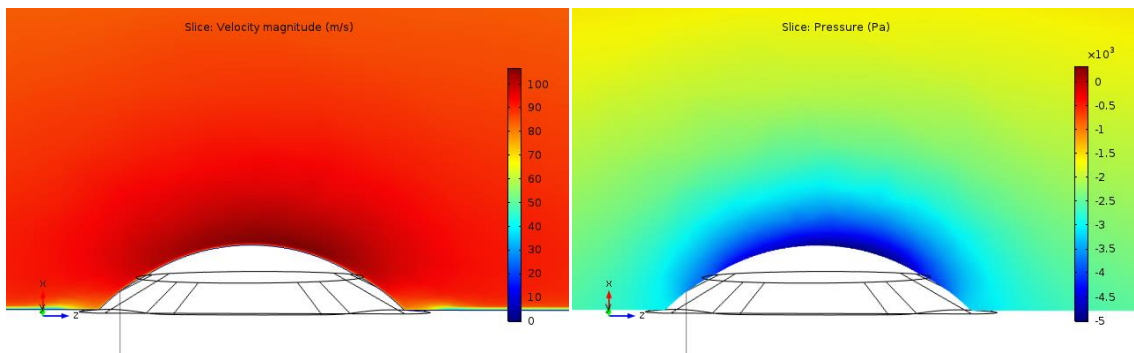


Figure A.5 Velocity and pressure fields alongside the wind turbine blade for second sensor model located, 34 meters from the blade root.

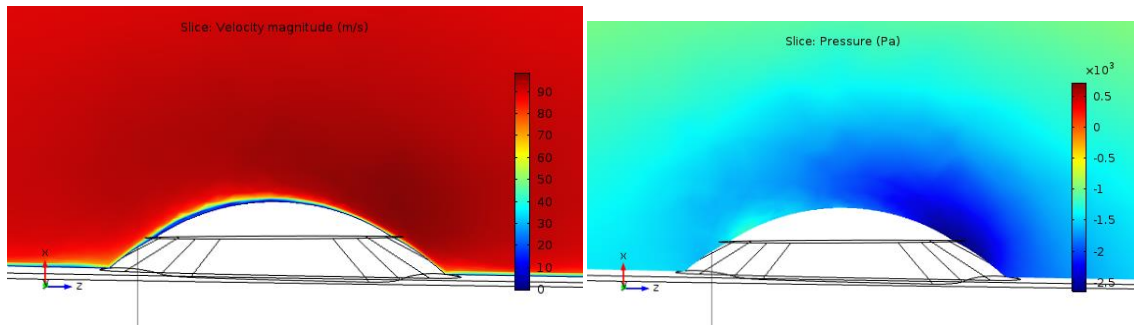


Figure A.6 Velocity and pressure fields alongside the wind turbine blade for second sensor model located, 42.8 meters from the blade root.

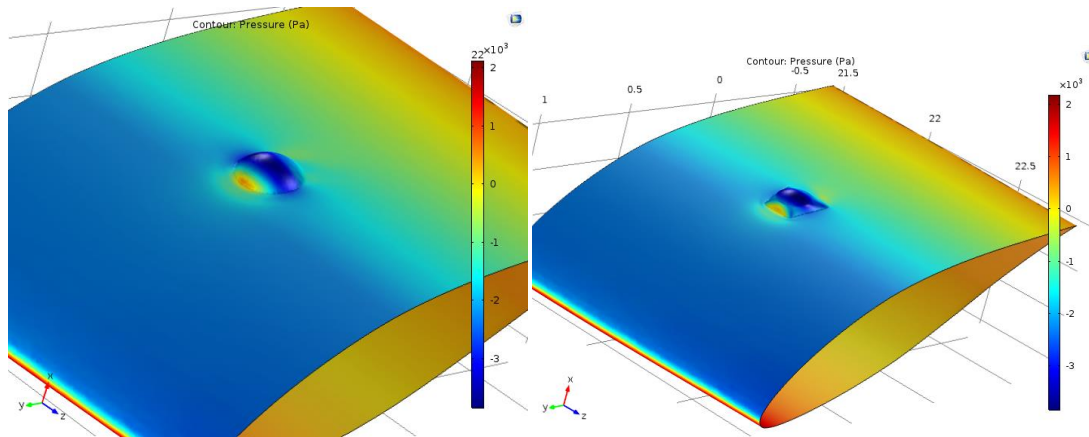


Figure A.7 Pressure distribution on the blade surface around the sensors with the 27 meter distance from the blade root

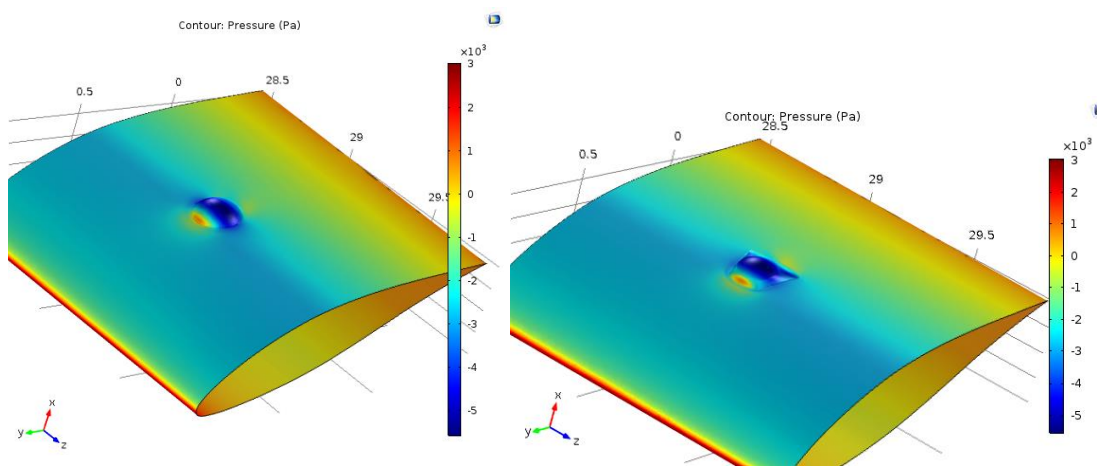


Figure A.8 Pressure distribution on the blade surface around the sensors with the 34 meter distance from the blade root

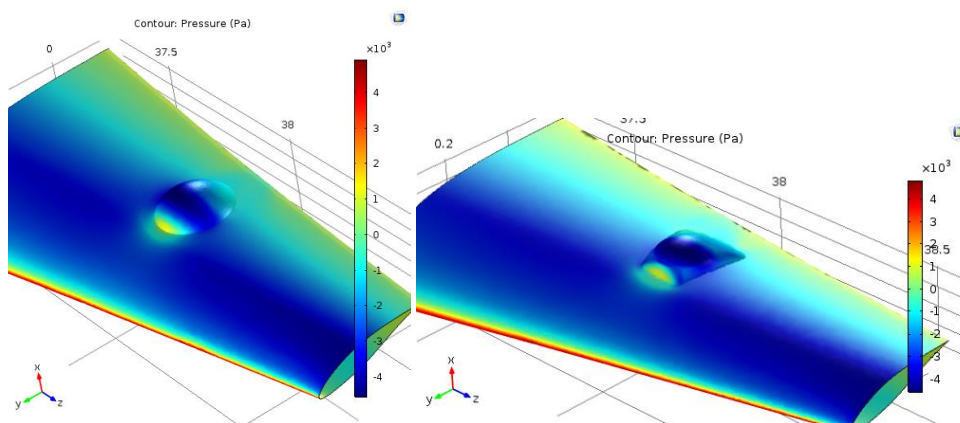


Figure A.9 Pressure distribution on the blade surface around the sensors with the 42.8 meter distance from the blade root